SMR: 1133/7

WINTER COLLEGE ON
SPECTROSCOPY AND APPLICATIONS

(8 - 26 February 1999)

"Environmental Applications of Spectroscopy"

presented by:

Sune SVANBERG
Lund Institute of Technology
Division of Atomic Physics
Lund
Sweden

Air Monitoring by Spectroscopic Techniques

Edited by

MARKUS W. SIGRIST

Infrared Physics Laboratory
Institute of Quantum Electronics
ETH Zurich
Zurich, Switzerland

A WILEY-INTERSCIENCE PUBLICATION

JOHN WILEY & SONS, INC.

New York / Chichester / Brisbane / Toronto / Singapore

DIFFERENTIAL ABSORPTION LIDAR (DIAL)

SUNE SVANBERG

Department of Physics,
Lund Institute of Technology, Lund, Sweden

3.1. INTRODUCTION

Advanced techniques are needed to monitor our threatened environment, i.e., to evaluate pollution levels and developmental trends. While measurements obviously do not improve the environmental conditions per se, they can provide the impetus for implementing appropriate environmental protection programs. Measurement can then confirm positive changes induced by these actions. In this way advanced measurement techniques can play a very constructive role in the process of improving the environment.

Measurements are required on a local, a regional, and also a global scale. Tropospheric pollution has obvious manifestations in terms of health problems, water and soil acidification, and forest damage. Human-induced stratospheric changes in the ozone layer, as evidenced by the occurrence of "ozone holes" at the polar caps, may have much more far-reaching consequences (Farman et al., 1985; Stolarski, 1988). The "greenhouse" effect, due to a global increase in infrared (IR)-absorbing gases such as CO_2, CH_4, and N_2O, is another process of paramount importance (Bach et al., 1979; Revelle, 1982; Mason, 1989). Gaseous pollutants injected into the atmosphere enter very complex atmospheric chemistry chains (Wayne, 1985; Seinfeld, 1986; Trush, 1988).

Optical spectroscopy based on the specific absorption properties of different gases provides sensitive and selective measurements of atmospheric constituents. Its nonintrusive nature and real-time data capability makes it particularly useful. It is well adapted to various remote-sensing approaches yielding data from large atmospheric volumes. Optical spectroscopic remote

sensing can be performed in a *passive* mode, employing natural radiation sources such as the sun or the blue sky, or in an *active* mode, using an artificial source such as a lamp or a laser. These approaches are illustrated in Fig. 3.1. In reflective passive monitoring, frequently performed from satellites, the modification in the infalling spectral distribution due to target absorption is studied. Passive atmospheric absorption—or, in the IR region, emission—can be utilized. Active monitoring in transmission frequently utilizes a CW (continuous wave) optical transmitter to sense the average absorption over an atmospheric path. Lidar (light *detection and ranging*) provides active optical remote sensing in backscattering. A pulsed laser transmitter is used, and light, backscattered from molecules and particles, is collected by an optical telescope and is detected and range-resolved in a radar-like mode. If the wavelength of the laser is varied from an absorption line of a pollutant gas to a close-by position, the detected changes in the backscattered light intensity can be used to evaluate range-resolved concentration profiles. This is the *differential absorption* version of the lidar method, and this is the main subject of the present chapter.

In all optical monitoring of the atmospheric constituents it is important to avoid the spectral regions where major atmospheric species basically block out the transmission. The same limitations pertain to normal, earthbound astronomical observations. Below 200 nm the Schumann–Runge bands of molecular oxygen (Thompson et al., 1963) put a definitive halt to atmospheric
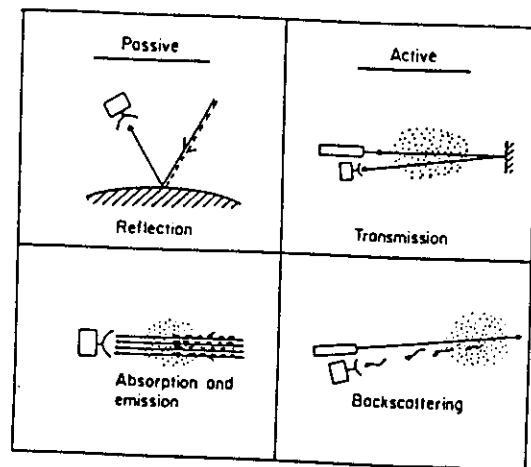

Figure 3.1. Schemes for optical remote sensing of the environment. From Svanberg (1980).

spectroscopy, leaving US vacuum ultraviolet (VUV) spectroscopy as a reliable laboratory discipline. Astronomical observations are effectively halted by stratospheric ozone absorption, which (presently) causes a cutoff at about 300 nm. The zero solar background below 300 nm makes the region down to 200 nm very attractive for atmospheric remote sensing with lidars, although the increasing Rayleigh and Mie scattering for short wavelengths imposes range limitations. In the visible region the atmosphere is obviously transparent, while substantial regions in the IR are completely blocked out by water and carbon dioxide absorption bands. An overview of the atmospheric transmission, pollutant absorption bands, and available laser sources is given in Fig. 3.2 (Grant and Menzies, 1983).

The absorption lines of the major atmospheric species and most important minor species including many pollutants are given in the extensive HITRAN compilation (Rothman et al., 1987). Very recently this material has become available on diskettes for easy personal-computer access (Killinger, 1992). The line widths of the molecular absorption lines are strongly pressure dependent and the relative strengths temperature dependent, which forms the basis for extractions of meteorological information (Korb and Weng, 1983). It also allows the deconvolution of line-of-sight passive observations of molecules present in the troposphere (broadened lines) as well as the stratosphere (sharp lines) (Menzies and Seals, 1977).

The purpose of the present chapter is to describe differential absorption lidar (DIAL) techniques for three-dimensional mapping of atmospheric pollutants. Such techniques allow the remote monitoring of ambient air, industrial emissions, natural emissions due to various geophysical phenomena (volcanoes or other geothermal sources), and monitoring of leaks on natural gas pipelines as well as warning systems for chemical warfare gases. The techniques can also be used for measurements of meteorological parameters such as temperature, humidity, and wind speed. Tropospheric as well as stratospheric studies can be performed. The present review is mainly focused on the description of DIAL monitoring of industrial pollution and geophysical emanations. A pedagogical rather than a comprehensive approach is taken, and no attempt is made to include all important references to the field. For the sake of convenience, examples are largely taken from work performed in the author's lidar groups at the Chalmers University of Technology and the Lund Institute of Technology over a time span of more than 15 years. Comprehensive references can be found in the books and review articles cited below.

The general topic of the present chapter has previously been treated in a few specialized monographs. Hinkley (1976) gives an early comprehensive review of laser monitoring of the atmosphere. In the proceedings of a conference edited by Killinger and Mooradian (1983), non-laser optical techniques such as DOAS (*differential optical absorption spectroscopy*) and FTIR (*Fourier*

Figure 3.1 Atmospheric transmission, pollutant absorption bands, and available laser sources. From Grant and Menzies (1983).

transform infrared spectroscopy) are included. Measures (1984) has written the most throughgoing treatise on laser remote sensing. In a follow-up multi-author volume edited by Measures (1988), the general field of laser remote chemical analysis is treated.

In a series of international laser radar conferences the topic has been extensively illuminated through the years. The number of conferences in the series presently amounts to 17, and the latest ones are cited here (McCormick, 1982a, 1992; Megie, 1984; Carswell, 1986; Stefanutti, 1988; Zuev, 1990).

Several reviews of the field of laser remote sensing of the atmosphere have been published, e.g., by Carswell (1983), Grant and Menzies (1983), Grant (1987), Kobayashi (1987), Fredriksson (1988), and Zanzottera (1990). The present author has also written a few shorter reviews (Svanberg, 1978, 1980, 1985, 1991). Many aspects of practical optical spectroscopy as well as the atomic and molecular physics background are treated in a new monograph (Svanberg, 1992).

We begin our discussion in Section 3.2 with some basic considerations pertaining to optical atmospheric monitoring. The field is introduced by a discussion of long-path absorption measurements, in particular using DOAS. Then different varieties of lidar measurements are introduced and discussed. The use of topographic targets has a clear connection with the long-path absorption technique. Atmospheric backscattering (Mie, Raman, and fluorescence) enables us to perform range-resolved measurements that are particularly characteristic of the lidar technique. Next, Section 3.3 is devoted to a thorough description of the differential absorption lidar (DIAL) method, allowing detailed monitoring of important pollutants. We then discuss in Section 3.4, important laser types used in modern lidar systems and describe in Section 3.5 the basic elements of lidar system design. In Section 3.6, concerning DIAL measurements of tropospheric pollutant gases, some examples of practical monitoring of different important pollutants are given. A special section (3.7) is reserved for a novel DIAL application—that of atomic mercury monitoring, which apart from the pollution aspects contains elements of geophysical studies (mining, geothermal energy, volcanoes, etc). Finally, the outlook for the future of DIAL technology is given in Section 3.8.

3.2 BASIC CONSIDERATIONS

There are two major kinds of optical methods applicable in active remote sensing of the atmosphere:

- Long-path absorption monitoring
- Lidar (*light detection and ranging*), with subdivisions:

Topographic target lidar

Mie scattering lidar

Fluorescence lidar

Raman scattering lidar

Differential absorption lidar (DIAL)

Since there are many elements in common between the two basic techniques, we will first consider long-path absorption measurements as an introduction to the various lidar schemes.

3.2.1. Long-Path Absorption Monitoring

Long-path absorption techniques are based on the same principles as spectrophotometry. However, by using well-collimated normal light beams or laser beams, it is possible to use a path length of several kilometers instead of the 1-cm cuvette typically used in the chemical laboratory. The principle is given in Fig. 3.3. A single-ended arrangement can be achieved by utilizing a corner cube retroreflector at the end of the light path and collecting the back-reflected light with a telescope. Since all detected photons have traveled the same path, no range resolution is obtained and only average concentrations can be determined. The light source can be a high-pressure xenon lamp, as in the case of DOAS. It is difficult to measure weak absorption lines in the presence of strong atmospheric turbulence because of strong scintillation. A fast scanning detection or parallel ccd (charge-coupled devices) spectral detection can then be used to overcome such difficulties. Tunable diode lasers and CW line-tunable CO_2 lasers are useful coherent sources for long-path absorption measurements. We shall come back to the scintillation problem later.

Although the topic of the present chapter is DIAL measurements, the
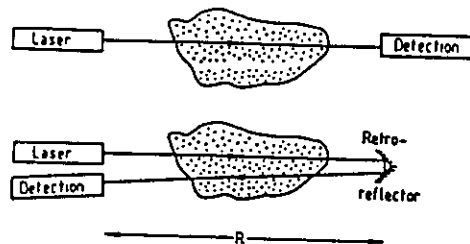
Figure 3.3. Principle of long-path absorption atmospheric spectroscopy.

pertinent principles are best illustrated by starting with a DOAS description. (DOAS is extensively treated by Platt in Chapter 2 of this book.) A DOAS setup is shown in Fig. 3.4 (Edner et al., 1993b). A high-pressure Xe lamp placed in the focus of a telescope is used to launch a well-collimated light beam over a distance of 100 m up to several kilometers. Light is reflected by a mirror and is directed into a Newtonian telescope. Light is focused into the entrance slit of a spectrometer and is detected by a photomultiplier tube (PMT). For fast scanning a number of slits are placed radially on a fast-rotating wheel in front of the PMT. The signals from a large number of scans are added in a computer. The sweep triggering is obtained from a photodiode observing the light from a light-emitting diode through the slotted wheel. In this way a chosen spectral region can repeatedly be swept during a time for which the atmosphere can be considered to be "frozen." An alternative way to reduce the influence of turbulence is to detect all wavelengths in a certain wavelength interval simultaneously by using a diode array detector.

An atmospheric recording of ambient SO_2 over a path length of 2000 m is shown in Fig. 3.5. In Fig. 3.5a the total light from the "white" lamp as seen by the detector is seen for the spectral region 280–320 nm covering the region of SO_2 absorption. Actually, a small absorptive structure can be seen. This can be enhanced by selecting the proper region and magnifying the structure as shown in Fig. 3.5b. A polynomial has been fitted to the general curve. This
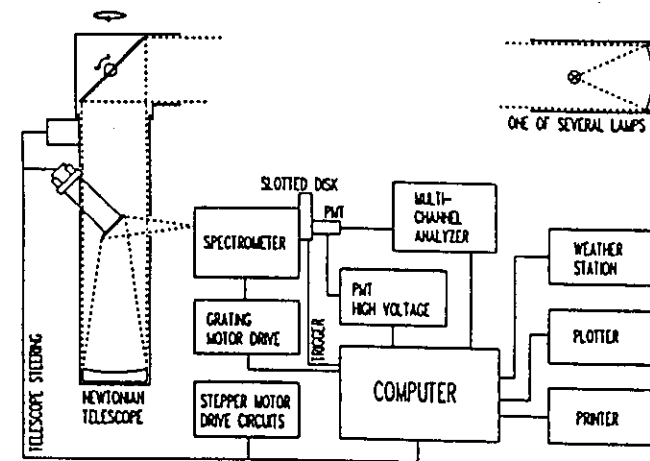

Figure 3.4. Setup for differential optical absorption spectroscopy (DOAS). From Edner et al. (1992a, 1993b).
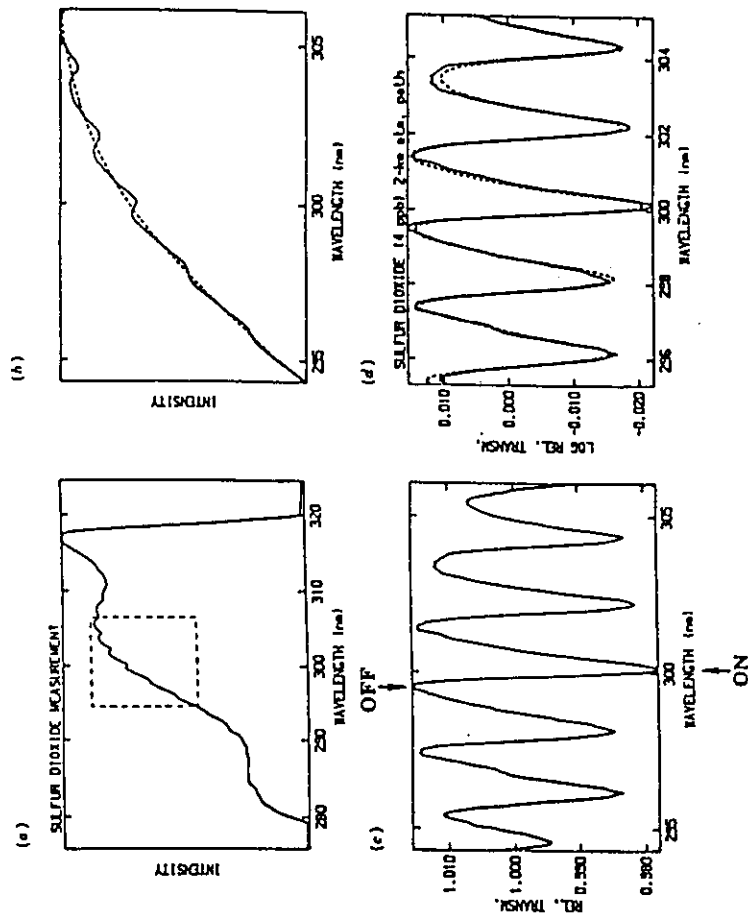
polynomial cannot reproduce the fast intensity variation, but rather provides a smooth curve for normalization. In Fig. 3.5c the intensity recording has been divided with the polynomial. Finally, in Fig. 3.5d the logarithm of the curve is formed for fitting to a weighted laboratory spectrum by employing the Beer–Lambert law. In this way an average concentration value of the pollutant is obtained for the measurement path. As can be seen, SO_2 provides a strongly modulated structure well suited also for DIAL. In the figure the two wavelengths normally used in DIAL are indicated. They have been chosen for maximum differential absorption within the smallest possible wavelength interval. Clearly, the "effective" absorption cross sections will vary with the spectral resolution, which is normally lower than the intrinsic line width owing to pressure (and Doppler) broadening. Thus it is important to determine the effective cross sections with the same resolution (the same apparatus!) in the laboratory as in the practical field measurements. It should also be noted that the Beer–Lambert law is not strictly valid when the instrument limits the resolution. Here laser sources have a great advantage over classical spectroscopic equipment.

Pollutant gas concentrations can be expressed as number densities (molecules/m³), which can be related to volume or mass fractions (ppm—parts per million, 10^6; ppb—parts per billion, 10^9; ppt—parts per trillion, 10^{12}). Nowadays the most common way to state pollution levels is to indicate mass per volume, i.e., $\mu g/m^3$.

Further DOAS spectra—of NO_2 and O_3—are given in Fig. 3.6. For both molecules the *differential* absorption is lower, but there is a substantial *general* absorption for both gases. In particular, ozone does not exhibit much structure, and DIAL measurements require a rather large wavelength separation for achieving a large enough change in the broad and little-structured ozone absorption bond. (See also Fig. 3.23 in Section 3.5.4.) Recently, a renewed spectroscopic study of the ozone molecule suggested use of a particularly strong differential structure close to 283 nm for DOAS measurements, as shown in Fig. 3.6b (Axelsson et al., 1990).

3.2.2. The Lidar Method

In the lidar method, laser pulses are transmitted into the atmosphere and backscattered radiation is collected by an optical telescope and detected as illustrated in Fig. 3.7. The first lidar experiments were performed by Fiocco and Smullin (1963).

A particularly useful characteristic of the lidar method is its capability of remotely monitoring large areas. The size of the covered area is of course closely related to the platform arrangement for the lidar system. These aspects are also illustrated in Fig. 3.7. From a fixed laboratory an industrial area or a
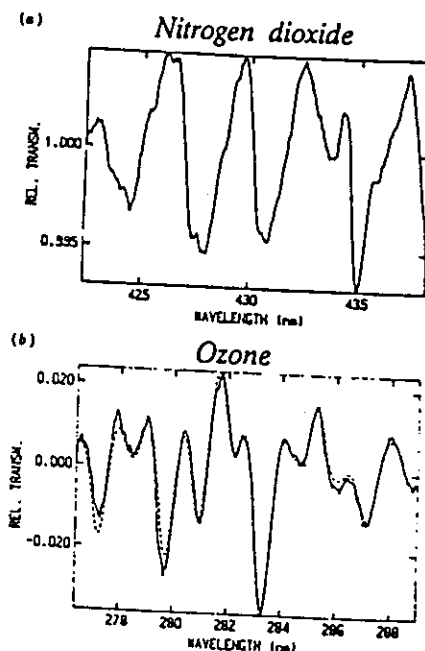

Figure 3.5. SO_2 DOAS measurement: (a) the raw recording of the lamp intensity observed over a 2000-m absorption path; (b) a magnified spectral region with a fitted polynomial(dashed line); (c) the recorded intensity divided by the polynomial; finally, in (d) the logarithm of the curve has been formed and a fit to a laboratory spectrum (dashed line) has been made, yielding a mean SO_2 concentration of 11 $\mu g\ m^3$ (4 ppb). From Edner et al. (1992a, 1993b).

(a)

Nitrogen dioxide

(b)

Ozone

Figure 3.6. DOAS recordings for NO$_2$ and O$_3$ over an optical path of 2000 m. Measured intensities have been divided by fitted polynomials to enhance the structure. The NO$_2$ recording (a) yields a mean gas concentration of 29 μg/m^3 (12 ppb), whereas the O$_3$ recording (b) yields 161 μg/m^3. From Edner et al. (1992a, 1993b) and Axelsson et al. (1990), respectively.

section of a city can be covered by scanning. A mobile system, particularly if supplied with its own electric power generator, can conveniently be deployed for various measurement campaigns in urban or industrial areas. Airborne systems have also been constructed and used very successfully for regional measurements. Finally, satellites can provide platforms for future global coverage by lidar space systems now being planned.

3.2.2.1. Topographic Target Lidar

In the lidar approach, a laser pulse is transmitted into the atmosphere and backscattered radiation is detected as a function of time by an optical receiver in a radar-like fashion. If the laser beam is directed against a distant,
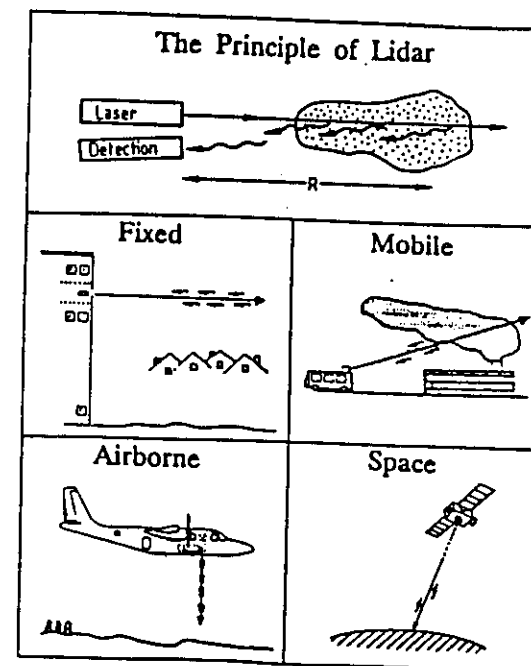
Figure 3.7. The lidar principle and different platform arrangements for lidar systems: Fixed laboratory, mobile system, airborne system, and spacecraft installation.

back-reflecting mirror (retroreflecting corner cube) at a distance R, a strong optical echo signal is received after a time

$$t = 2R/c \qquad (3.1)$$

where c is the velocity of light. This is a principle of, e.g., lunar ranging against retroreflectors placed by Apollo astronauts (range precision: a few centimeters) or satellite tracking for geodetical applications. Even if a natural (topographic) target such as a brick wall, vegetation, or a mountainside is chosen, there will be a distinct but fainter echo signal. This is the principle of military range finders. Ranging is illustrated in Fig. 3.8, where a nitrogen-laser-pumped dye laser operating in the blue spectral region is fired against a mountainside at a distance of 5.5 km (Fredriksson et al., 1979). The backscattered light is received
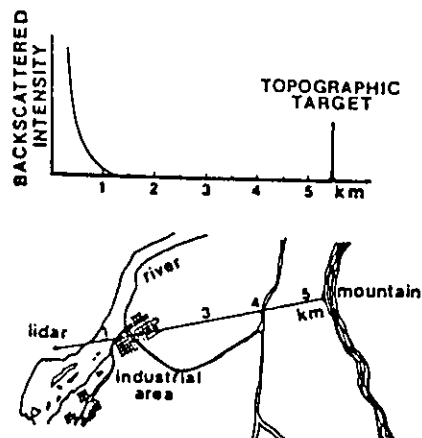
Figure 3.8. Illustration of NO_2 measurements against a topographic target. From Fredriksson et al. (1979).

by an optical telescope of diameter 30 cm and the optical echo is transformed into an electronic signal in a fast PMT. With light traveling at 300 m/μs the echo will be detected about 37 μs after the laser pulse. For a pulse length of δt, the minimum width of the echo signal expressed as a range δR will be

$$\delta R = \delta t/2c \tag{3.2}$$

Owing to the finite response time of the detection system, the width can frequently be larger. The intensity $P(\lambda)$ of the echo depends on many factors including laser pulse energy, range, telescope area, and the diffuse reflectance (albedo) of the target. It also depends on the wavelength-dependent absorption cross section $\sigma(\lambda)$ of the atmosphere. If only the absorption cross section for the pollutant gas varies when the wavelength of the laser is changed from λ_{on} (on the absorption line) to the nearby wavelength λ_{off} (off the absorption line) and no other gas constituents interfere (or absorb equally for the two wavelengths), the Beer–Lambert law yields

$$P(\lambda_{on})/P(\lambda_{off}) = \exp\left[-2RN(\sigma_{on} - \sigma_{off})\right] \tag{3.3}$$

where $[\sigma_{on} - \sigma_{off}]$ is called the differential absorption cross section, and N is the average concentration of the gas studied.

Equation (3.3) assumes that the diffuse reflectance of the target does not change for the small wavelength change $\Delta\lambda = \lambda_{on} - \lambda_{off}$. This is normally the case for solid materials interrogated in the UV or visible region. However, in the IR region, e.g., around 10 μm, where the CO_2 laser operates, a differential albedo can exist for the target material (Shumate et al., 1982; Grant, 1982; Englisch et al., 1983). This is due to the sharpness of the molecular vibration spectra even in solids or liquids. This phenomenon can then be used for remote characterization of the target, e.g., in airborne geophysical applications. In such measurements it is instead important to choose the wavelengths in such a way that a zero atmospheric differential absorption value is obtained.

If a gaseous pollutant with a nonzero differential absorption for the small wavelength change chosen is present in the air, the relative topographic echo heights will change as described by Eq. (3.3). The echo serves the role of a power meter placed at the end of the (doubled) path, with the considerable convenience that nobody needs to place the power meter at the remote location. For the case shown in Fig. 3.8, the laser wavelength was changed from 448.1 to 446.5 nm. A 4% change in echo height was observed. Based on the relevant differential absorption cross section for the wavelength pair used, it was concluded that the average concentration on NO_2 over the 5.5 km path from the lidar system to the mountain was about 2 ppb. In airborne lidar measurements the surface of the earth is available as a topographic target for mean concentration determinations.

3.2.2.2. Mie Scattering Lidar

Mie scattering from particles and Rayleigh scattering from molecules provide strong signals observed in backscattering in lidar sounding of the free atmosphere. These scattering processes are elastic, i.e., the scattered photons have the same frequency as the incoming light (apart from possible small Doppler shifts). This signal can clearly be seen in Fig. 3.8 for ranges up to 1300 m and can be considered to be due to a "distributed" topographic target, present at all distances. Rayleigh scattering has a strong $1/\lambda^4$ dependence on the wavelength and can yield a dominating signal at short UV wavelengths. Mie scattering has a slower wavelength dependence ($\approx 1/\lambda^2$) and increases in relative importance to be dominant in particle-rich air probed at visible and near-IR wavelengths. The Mie backscattering from particles thus allows a mapping of the relative distribution of particles over large areas if the lidar system is scanned (see, e.g., Shimizu et al., 1985). However, since Mie scattering theory (van de Hulst, 1957; Kerker, 1969) involves many normally inaccessible particle parameters, quantitative results are difficult to obtain. Mie scattering is extremely useful in providing the "distributed mirror" needed in DIAL, the main topic of this chapter. As discussed below, measurements are then made at two close-lying

wavelengths exhibiting a nonzero differential absorption cross section for the gas of interest, and the two signals are divided to eliminate all unknown Mie scattering parameters.

From Fig. 3.8 it is obvious that the atmospheric backscattering exhibits a strong range dependence, basically reflecting the $1/R^2$ illumination law. We would now like to discuss the lidar signals more closely and introduce the general lidar equation, yielding the received laser radar intensity $P(\lambda, R)$ from a range R:

$$P(\lambda, R) = CWn_b(R)\sigma_b \frac{\Delta R}{R^2} \exp\left(-2 \int_0^R [\sigma(\lambda)N(r) + K_{ext}(r)] dr\right) \quad (3.4)$$

Here C is a system constant; W is the transmitted pulse energy; and $n_b(R)$ is the number density of scattering objects with backscattering coefficient σ_b. The exponential factor describes the attenuation of the laser beam and the backscattered radiation due to the presence of absorbing molecules of concentration $N(r)$ and absorption cross section $\sigma(\lambda)$ and due to scattering particles with wavelength-independent extinction $K_{ext}(r)$.

There exists a complicated relation between σ_b and K_{ext} for particle scattering. Certain simplifying assumptions are frequently made to allow an evaluation of the particle distribution $n_b(R)$. Much work has been invested into inverting the lidar equation. One of the most commonly used technique is the Klett inversion (Klett, 1981, 1986). If the absorption due to the particles is very small (thin clouds), the extraction of relative values of $n_b(R)$ is very simple, with a constant σ_b value assumed. A close-range recording of industrial particulate pollution is shown in Fig. 3.9. Superimposed on a general $1/R^2$ signal due to a uniform background particle distribution, localized signals of increased backscattering are seen owing to the industrial plumes. The stepwise attenuation of the uniform backscattering when the main plume is being passed can also clearly be seen.

Pure Mie scattering is extensively used for studying stratospheric dust from volcanic eruptions (McCormick, 1982b; McCormick et al., 1984; Osborn et al., 1992; Stefanutti et al., 1992b). Such studies are important for assessing perturbations in the earth's radiation budget. The year 1816 became known as "the year without a summer" because of an extensive volcanic eruption. Recent major eruptions that have been much studied by vertically sounding Mie lidars were due to El Fuego, Guatemala (1974), El Chichon, Mexico (1982), and Mt. Pinatubo, the Philippines (1991). Lidar recordings of the development of the stratospheric dust layer from Mt. Pinatubo are shown in Fig. 3.10 (Osborn et al., 1992). The Mie-to-Rayleigh scattering ratio has been plotted, eliminating (e.g., the $1/R^2$ distance dependence.
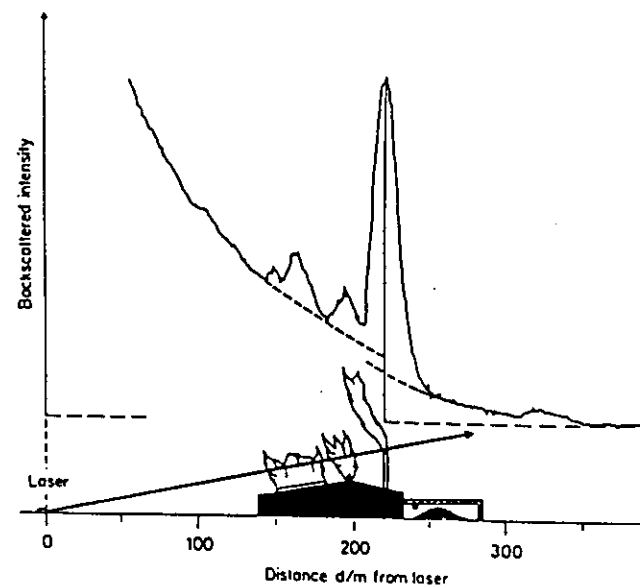
Figure 3.9. Mie scattering lidar particle monitoring at an iron-alloy plant. From Fredriksson et al. (1976).

3.2.2.3. Raman Lidar

Raman scattering is a much more well-defined scattering process, that can be used for quantitative measurements of gaseous constituents of the atmosphere. For the case of Raman lidar the constants in the lidar equation (3.4) have a new meaning, so that $n_b(R)$ is the number density of the Raman scattering molecules and σ_b is the Raman cross section. In contrast to the Mie and Rayleigh processes, Raman scattering is inelastic. In vibrational Raman scattering, a molecular vibrational quantum is picked up from the incoming photon, leaving the scattered quantum characteristically red-shifted (Stokes-shifted) with respect to the Rayleigh scattering by an amount corresponding to the molecular vibrational energy. Raman scattering from the major atmospheric constituents, O_2, N_2, and H_2O, is seen in the insert of Fig. 3.11, exhibiting the characteristic Raman shifts (1556, 2331, and 3652 cm^{-1}) for these molecules (Fredriksson et al., 1976). The main difficulty in using Raman scattering is its inherent weakness, typically 10^3 times weaker than the
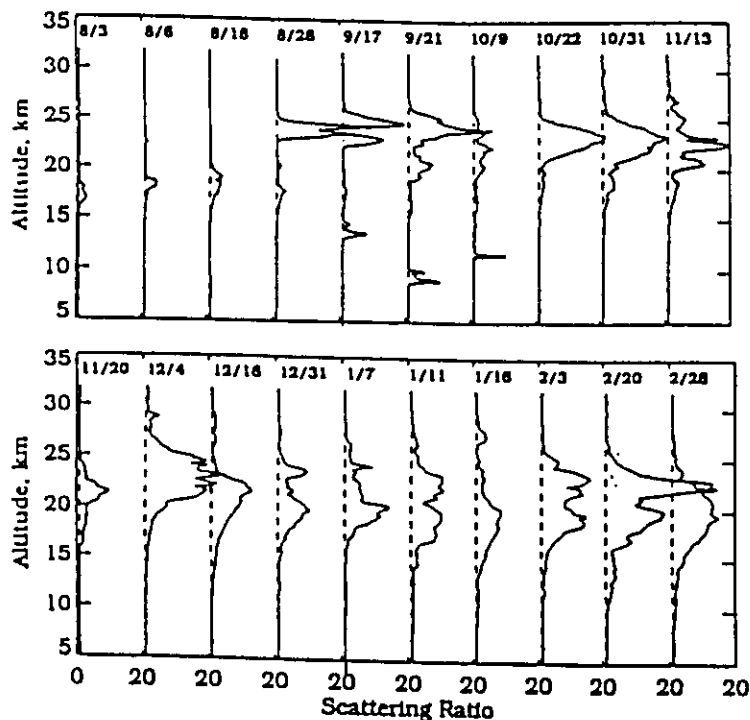
Figure 3.10. Lidar recordings of stratospheric dust due to the Mt. Pinatubo volcanic eruption. The Mie scattered intensity divided by the expected Rayleigh scattering intensity from a particle-free atmosphere has been plotted. Recordings taken at Hampton, Virginia, covering the period, Aug. 3, 1991, to Feb. 28, 1992. From Osborn et al. (1992).
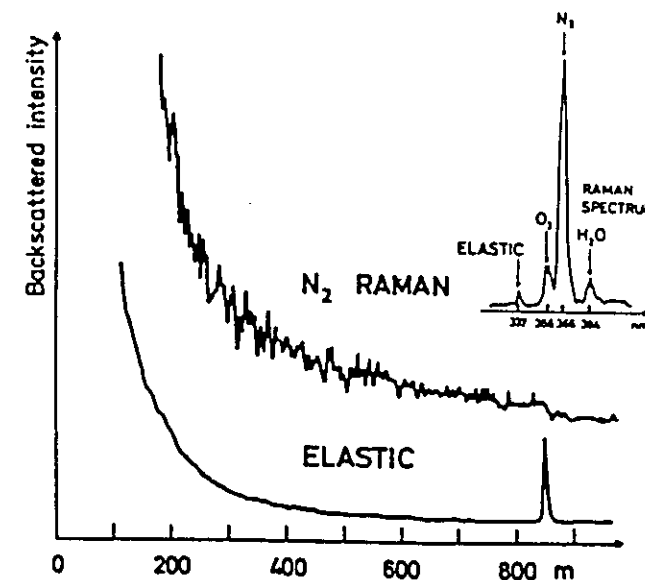

Figure 3.11. Elastic backscattering and N_2 Raman scattering recordings against a solid target at an 850-m distance. The measurements were performed with a nitrogen laser operating at 337 nm. Inset: a spectrally resolved recording of atmospheric backscattering is shown, featuring peaks due to oxygen, nitrogen, and water vapor. From Fredriksson et al. (1977).

Rayleigh scattering from the same molecule. This must be compensated by very high concentrations and short measuring ranges even when large lidar systems are used (Hirschfeld et al., 1973). Thus, the Raman technique is useful mainly for the major atmospheric constituents. First Raman lidar recordings were actually performed for N_2 and O_2 (Leonard, 1967).

A Raman lidar recording is obtained by suppressing the strong elastically backscattered light and instead centering the detection band (selected by a sharp interference filter with high out-of-band rejection) on the appropriate Raman-shifted wavelength. A nitrogen Raman lidar recording is shown in Fig. 3.11 together with a corresponding elastic recording (Fredriksson et al.,

1977). In this case the beam from a nitrogen laser ($\lambda = 337$ nm) was terminated against the bricks of a smoke stack, clearly seen as an echo at 850 m in the elastic signal. In contrast, the nitrogen Raman recording shows the uniformly decreasing $1/R^2$ falloff for the ambient nitrogen and a sudden disappearance of the signal at the encounter of the solid target.

Nitrogen Raman signals can be used for measuring atmospheric attenuation (nontrivial deviations from $1/R^2$ dependence), since the signal is not strongly influenced by the particle backscattering. Another major application is vertical sounding of water vapor profiles, which are of great meteorological importance and are useful in radiation budget assessments. Examples of water vapor mixing ratio recordings taken with a high-energy XeCl excimer laser ($\lambda = 308$ nm) are shown in Fig. 3.12 (Ansmann et al., 1992). Here the water Raman signal has been divided by the nitrogen Raman signal. Water vapor can also be measured by DIAL (Browell et al., 1978; 1981).
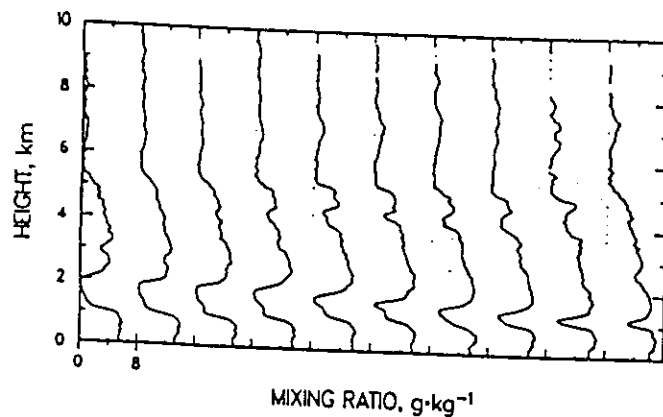
Figure 3.12. Water vapor Raman lidar curves, plotted as mixing ratios (water vapor to dry air). From Ansmann et al. (1992).

Rotational Raman scattering utilizes the extremely small wavelength shifts due to the absorption or emission of a quantum corresponding to a rotational transition. Since the population distribution on the different rotational levels is very temperature dependent, rotational Raman scattering can be employed for vertical temperature measurements using lidar signals from N_2 or O_2 (Hauchecorne et al., 1992).

3.2.2.4. Fluorescence Lidar

In fluorescence lidar a laser tuned to the absorption line of an atmospheric species is used and fluorescence light is detected in the subsequent decay. For this case $n_b(R)$ in Eq. (3.4) is the number density of fluorescing atoms and σ_b is the fluorescence cross section. Fluorescence lidar is a powerful technique for measurements at mesospheric heights, where the pressure is low and the fluorescence is not quenched by collisions. The collisions induce radiationless decays to the ground state, eliminating many atoms from contributing to the fluorescence light emission. At normal atmospheric pressures the quenching dominates by a factor of about 10^3 over fluorescence, effectively eliminating the light. After first demonstrations by Bowman et al. (1969), the technique has been used extensively to monitor layers of various alkali and alkaline earth atoms (Li, Na, K, Ca, Ca$^+$, and Fe) at a height of about 100 km (Chanin, 1983; Fricke and von Zahn, 1985; Hansen and von Zahn, 1990; Collins et al., 1992; Kane et al., 1992). The mesospheric atoms are formed from vaporization of

micrometeorites. By monitoring the movements of the layers the atmospheric dynamics can be studied, including the formation of gravitational waves.

An example of a recording of the mesospheric sodium layer is shown in Fig. 3.13 (Collins et al., 1992). A narrow-band laser was tuned to the sodium resonance line. In the same recording, taken at the South Pole, the Mie scattering return from polar stratospheric clouds (PSCs) is shown. Such clouds are very important in the polar ozone destruction process.

A novel application of fluorescence lidar is the creation of "guide stars" of fluorescing sodium atoms in the mesosphere for rectifying images of large-scale astronomical telescopes. The technique of adaptive imaging strongly enhances the performance of ground-based telescopes and is now being implemented widely (Thompson and Gardner, 1987; Collins, 1992). Recently, it was realized that the sodium wavelength can conveniently be generated by mixing the two Nd:YAG laser wavelengths 1.064 mm and 1.319 μm (Jeys et al., 1989).

3.2.2.5. Solid Target Fluorescence Lidar

In Fig. 3.8 the typographic target echo was recorded by using the elestically backscattered light. However, fluorescence is induced in the target by the laser pulse, and if the signal is strong enough the wavelength contents of the echo can be analyzed at the site of the receiver system. An optical multichannel analyzer with an image-intensified array detector is well suited for such measurements. Then the full fluorescence spectrum can be captured for every laser shot. The image intensifier can also be gated down to 5 ns to accept light
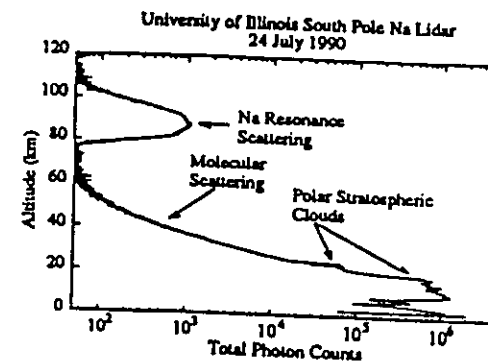

Figure 3.13. Recording at the South Pole of the mesospheric sodium layer (seen in resonance fluorescence) and polar stratospheric clouds (seen in Mie backscatter). From Collins et al. (1992).

arriving only at the right delay. In this way ambient light can be suppressed.

Fluorescence spectroscopy has long been used for analytical and diagnostic purposes (Udenfriend, 1962, 1969; Wehry, 1976; Hercules, 1966; Lakowicz, 1983). Laser-induced fluorescence (LIF) has an interesting potential for remote sensing of environmental parameters. For quite some time, hydrospheric pollution monitoring has been performed with airbone laser-based fluorosensors. Different kinds of oil can be identified by their fluorescence properties. Other pollutants and algal bloom patches can similarly be studied (O'Neill et al., 1980; Capelle et al., 1983; Hoge et al., 1986; Reuter, 1991). By use of the blue-green transmission window of water, bathymetric measurements of sea depths can be performed as well (Kim, 1977; Hoge et al., 1980). The field of laser-based hydrospheric monitoring is covered by Measures (1984). LIF has also been used by American (Hoge et al., 1983; Hoge, 1988; Chappelle et al., 1985), Italian (Cecchi and Pantani, 1991) and Swedish groups (Svanberg, 1990; Edner et al., 1992d) for studies of land vegetation.

Examples of laboratory spectra for various oil products that might appear in the aquatic environment are shown in Fig. 3.14 (Celander et al., 1978). As a rule, light petroleum fractions exhibit blue-shifted, intense fluorescence whereas heavier fractions also have longer wavelength components and fluoresce more weakly. At shot UV wavelengths the penetration of the exciting light into the oil is limited to micrometers. For longer wavelengths the penetration depth is larger. Thus, in order to assess the thickness of an oil film the choice of excitation wavelength is important. In the assessment of marine oil spills, the fluorescence characteristics of different oil products play an important role in airborne measurements and in the decision regarding the correct oil-fighting countermeasures to be implemented.

Algae fluorescence monitoring can be important for measuring the total marine productivity, which originates in the conversion of solar energy, CO_2, and nutrients into organic matter by microscopic phytoplankton. Recently, huge algal blooms, for instance, of *Chrysochromulina polylepis*, leading to devastating consequences for most other marine life forms, have occurred owing to eutrophication of coastal waters. Some classes of algae exhibit LIF spectra with certain characteristic features (Celander et al., 1978) in addition to the dominating peak at 685 nm due to chlorophyll *a*. A blue-green fluorescence is normally observed for water even in the absence of oil spills. This fluorescence is due to organic material (*Gelbstoff*). Measurement scenarios for fluorescence lidar monitoring of water and land vegetation are shown in Fig. 3.15 with examples of remotely recorded spectra.

In aquatic monitoring a strong Raman signal due to the water molecules is observed at a Raman shift of about 3400 cm^{-1} (O—H stretch vibration), as shown in Fig. 15a. This signal is very useful, since it is possible to utilize it as a reference to normalize algal and *Gelbstoff* signals to the same effective water
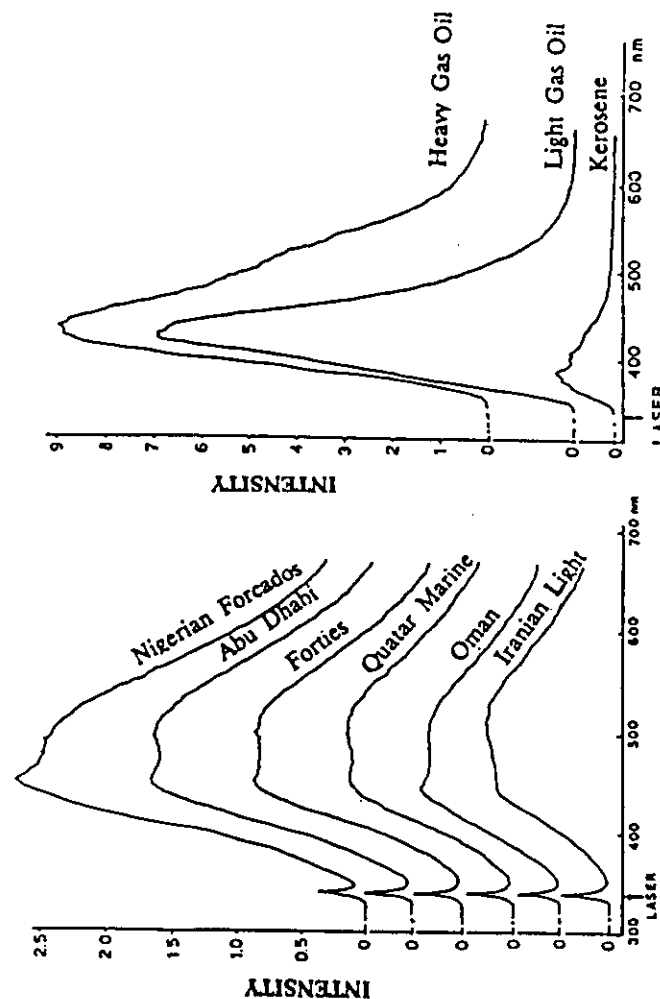

Figure 3.14 Laboratory recordings of laser-induced fluorescence from different crude oils and refined products. The excitation source was a nitrogen laser operating at 337 nm. The recordings are not corrected for varying spectral response of the detector. In corrected curves the intensities for red colors increase. From Celander et al. (1978).
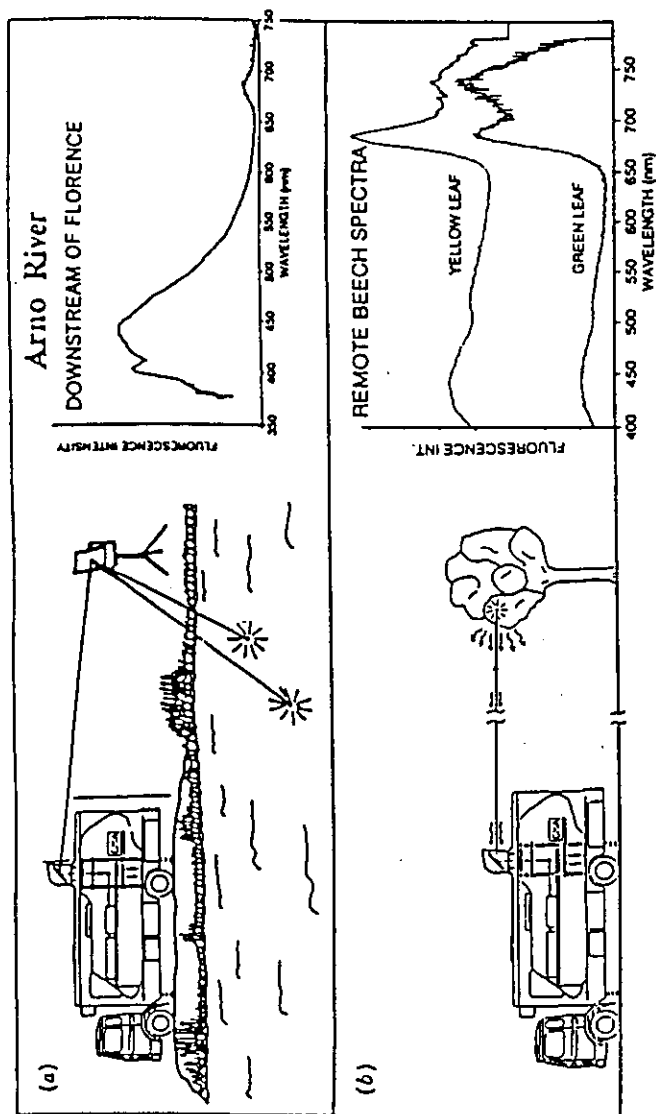
Figure 3.15. Fluorescence lidar measurements of (a) water and (b) terrestrial vegetation. A frequency-tripled Nd:YAG laser operating at 355 nm was used. Remote laser-induced fluorescence spectra are shown for a measurement distance of about 50 m. Adapted from Edner et al. (1992d,e).

measuring volume. A careful analysis of the shape of the water Raman signal provides information on the water temperature. Water molecules form aggregates of different sizes with slightly different Raman shifts. The relative occurrence of mono-, di-, and poly-water molecules is temperature dependent (Leonard et al., 1979; Breschi et al., 1992).

Land vegetation monitoring by fluorescence lidar is shown in Fig. 3.15b, illustrating different signatures for green and lightly yellow maple leaves. The ratio of the two chlorophyll peaks at 690 and 735 nm relates to different plant physiological conditions, as discussed by Lichtenthaler and Rinderle (1988). Land vegetation can be efficiently characterized by multispectral reflectance measurements using spaceborne sensors in satellites such as LANDSAT, SPOT, and ERS-1 (Chen, 1885). An *active* remote sensing technique such as LIF might, in certain circumstances, complement *passive* reflectance monitoring.

3.3. PRINCIPLES OF DIFFERENTIAL ABSORPTION LIDAR (DIAL)

The principles of DIAL are schematically represented in Fig. 3.16, where a measurement scenario in an industrial area is illustrated. Laser pulses are transmitted into the atmosphere, which for the time being is (unrealistically) assumed to contain a uniform distribution of Mie scattering particles. A gaseous pollutant is emitted from the industry as indicated and penetrates in between the uniformly distributed particles, which provide "topographic targets" located everywhere. The industrial effluent is assumed to be free of additional particles. Laser light is alternatingly transmitted at a wavelength (λ_{on}), where the species under investigation absorbs, and at a neighboring, off-resonant wavelength (λ_{off}). In the presence of an absorbing gas cloud the on-resonance signal is attenuated through the cloud and the off-resonant one is not. If the particle concentration is low, the off-resonant signal will exhibit a pure $1/R^2$ dependence as shown in Fig. 3.16, whereas additional intensity losses occur when the gas is encountered. The differences between the two curves is best visualized by dividing them for each range interval. For identical curves a ratio value of unity is obtained for all ranges. This is true only if the Mie scattering from the particles does not change when the wavelength is changed from the on to the off value. For spherical particles of uniform size (monodisperse particles) the Mie scattering cross section exhibits a strong oscillatory behavior as a function of wavelength. However, for natural atmospheres the size and shape of the particles vary continuously and the oscillations are smeared out. Thus, for practical cases the on- and off-wavelength curve division is unaffected if the wavelength separation is small. The resulting curve is called the DIAL curve.
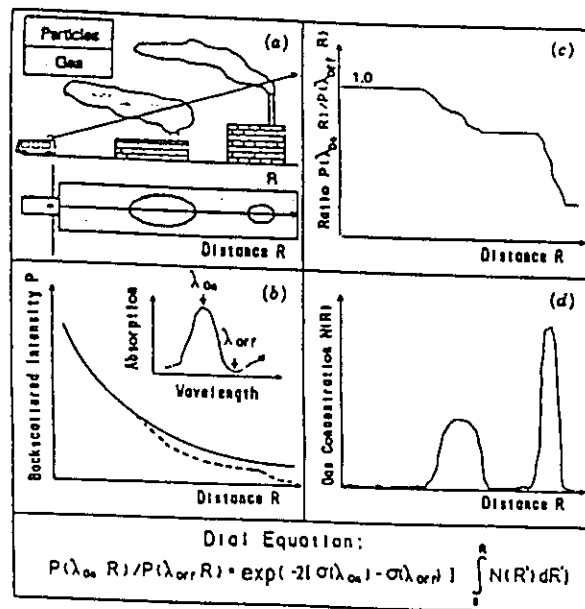
Figure 3.16. The principle of differential absorption lidar (DIAL). From Edner et al. (1987b).

When a gas cloud is encountered there is a downward slope on this ratio curve, which after the cloud passes resumes its horizontal direction but at a lower level. From the DIAL curve it is clear that the gas concentration as a function of range can be calculated basically by employing the Beer–Lambert law and using the differential absorption cross section for the gas. Such a calculated concentration curve is also included in Fig. 3.16.

At this point we note that we really do not need our initial pedagogical (and unrealistic) assumption that there is a uniform particle distribution. Even if there would have been a localized cloud of additional particles increasing the backscattering strongly for this particular range, the resulting upward bump would be equally present in the on- and off-resonance curves and would thus not show up in the ratio (DIAL) curve. Even most other troublesome and unknown parameters are eliminated in the division, and the gas concentration as a function of the range along the beam can be evaluated with knowledge of the differential absorption cross section only.

What we have found here using hand-waving (informal, off-the-cuff) arguments can of course be put on a rigorous mathematical foundation. The DIAL

curve is obtained by forming the lidar equation (3.4) first for the *on* wavelength and then for the *off* wavelength. Then the two equations are divided by each other, yielding

$$\frac{P(\lambda_{on}, R)}{P(\lambda_{off}, R)_0} = \exp\left[-2(\sigma_{on} - \sigma_{off})\int^R N(r)dr\right] \tag{3.5}$$

The assumptions we have made are that σ_b and $K_{ext}(r)$ are wavelength independent for a sufficiently small wavelength change. If we want to calculate the average concentration value $N_{av}(R, R + \Delta R)$ for a certain range interval ΔR, this can easily be made using Eq. (3.5). We obtain

$$N_{av}(R, R + \Delta R) = \frac{1}{2(\Delta R)[\sigma_{on} - \sigma_{off}]} \cdot \ln \frac{P(\lambda_{off}, R + \Delta R)P(\lambda_{on}, R)}{P(\lambda_{on}, R + \Delta R)P(\lambda_{off}, R)} \tag{3.6}$$

From the hand-waving description as well as from Eq. (3.6) it is obvious that a sufficiently large range interval ΔR must be chosen to allow a significant average concentration value N_{av} for the corresponding interval to be evaluated. The larger the concentration values are, the easier the expression following the "in" in the equation obtains a significant value for a given value of ΔR. This is easily understood by observing that this expression is the DIAL curve value at R divided by the DIAL curve value at $R + \Delta R$. A large slope on a noise-free DIAL curve yields high-quality data for the range-resolved concentration curve. For high concentrations a high spatial resolution can be used while still producing accurate data. To enable the numerical evaluation to be performed in the presence of the noise in the experimental data, the DIAL curve is normally "smoothed" before the concentration calculation by forming a sliding average over a number of digital range channels in the electronic detection system.

The DIAL technique was pioneered by Shotland (1966), who studied water vapor. First DIAL measurements on an atmospheric pollutant were reported by Rothe et al. (1974a, b) and Grant et al. (1974) for the case of NO_2.

In this section we shall present two simple applications of the DIAL technique: the case of a strong pollutant plume in an otherwise clean atmosphere, and the case of a uniform gas distribution in the atmosphere. Later, many examples of the more common situation of nonuniform distributions will be given.

In Fig. 3.17 we demonstrate a remote measurement of the NO_2 contents in an industrial plume. The laser beam was directed just above the top of the smokestack. To the left in the figure as shown the on- and off-resonance lidar recordings for NO_2. A logarithmic representation is used to decrease the large signal differences at close and far-off ranges. In the elastic backscatter curves a
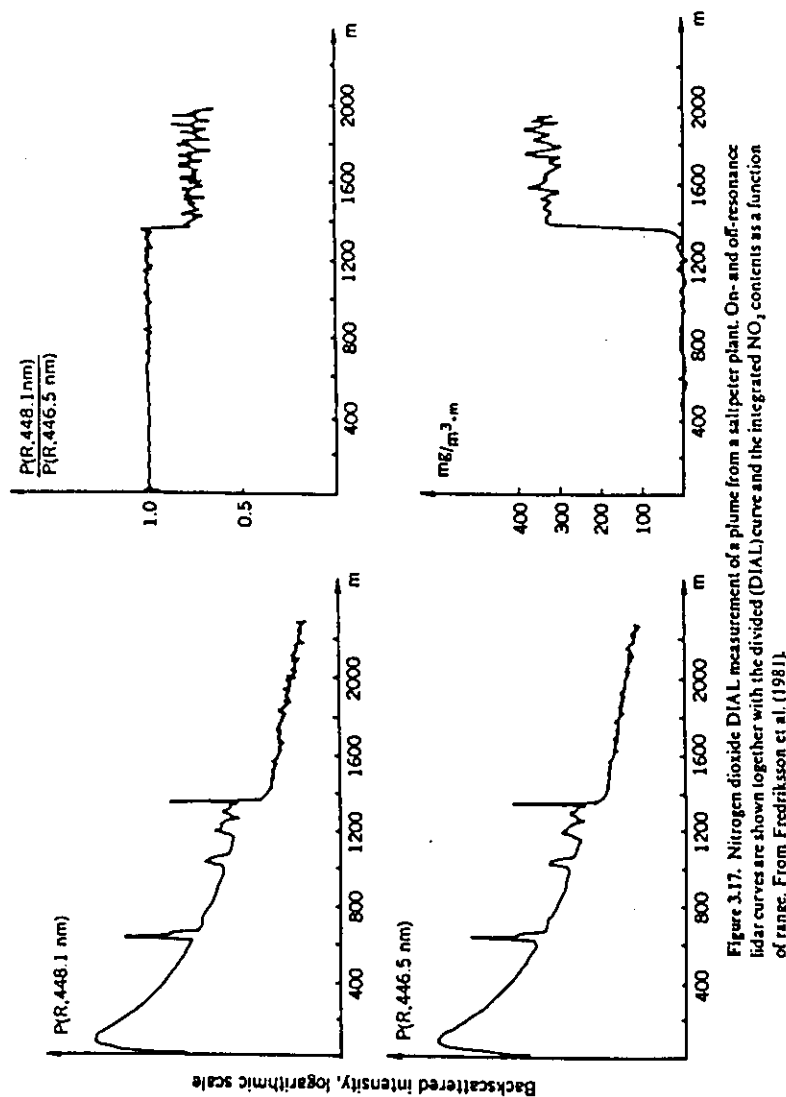
Figure 3.17. Nitrogen dioxide DIAL measurement of a plume from a saltpeter plant. On- and off-resonance lidar curves are shown together with the divided (DIAL) curve and the integrated NO₂ contents as a function of range. From Fredriksson et al. (1981).

number of particle-containing plumes accidentally drifting into the laser beam are clearly seen in addition to the one that is actively aimed at (at a 1350-m distance). The backscattered radiation is attenuated only by this plume, as can be clearly seen in the curves. It can also be seen that the attenuation is larger in the 448.1 nm curve because of the strong NO_2 absorption at this on-resonance wavelength. In the upper-right part of the figure the divided (DIAL) curve is shown. It can then clearly be seen that the effect of the particle plumes is eliminated. The only effect "surviving" the ratio formation is the step at 1350 m. Using Eq. (3.6) and the differential cross section for the NO_2 absorption, we can calculate the integrated NO_2 concentration as shown in the lower right corner. Knowing the gas flow rate from the stack it is possible to conclude that the emission amounted to about 40 kg/h.

The case of a uniform gas distribution is normally not a realistic one. However, the permanent gases such as N_2 and O_2 of course show this behavior, and in Fig. 3.18 we show the case of atmospheric oxygen in order to illustrate the application of the DIAL equation. This measurement was performed in the very weak oxygen absorption band surrounding the atomic mercury line at 254 nm. In the top part of the figure individual lidar curves for on- and off-resonance laser tuning are shown. At about a 1200-m distance the laser beam hits a hill, resulting in sharp echoes in both curves. The close-range intensity has been reduced by ramping up the amplification of the system to reach its full constant value only at a range of 600 m. In the lower part of the figure the DIAL curve is shown. For the case of a uniform distribution, Eq. (3.5) takes the very simple form of a pure exponential:

$$\frac{P(\lambda_{on},R)}{P(\lambda_{off},R)} = \exp[-2NR(\sigma_{on} - \sigma_{off})] \qquad (3.7)$$

which is clearly shown in Fig. 3.18. Equations (3.7) and (3.3) are identical, as expected.

3.4. LASERS FOR DIAL

Since the introduction of the laser in 1960 a large number of laser types have been developed. Some of these are more practical and useful than others, and a few systems have emerged as the DIAL lasers of choice. Important requirements for DIAL use are tunability, high pulse energy, and sufficiently short pulse length. Since the lasers need to be used in operational field equipment they must be sufficiently rugged and practical. The most useful DIAL lasers are shown in Fig. 3.19. Two of the laser systems shown, the Nd:YAG laser and
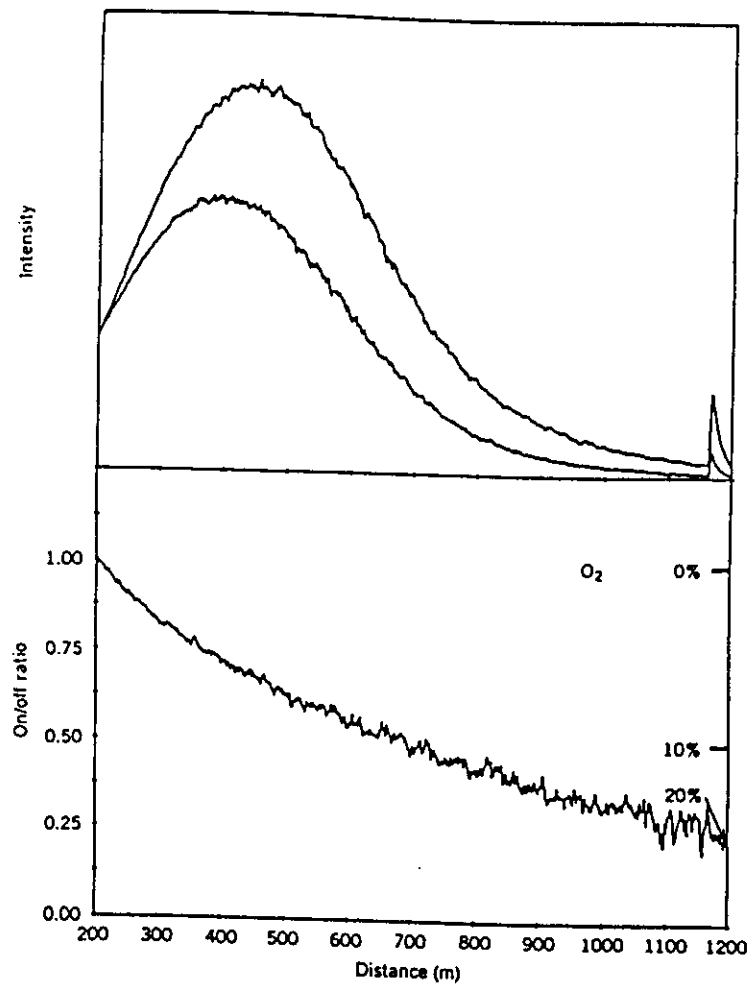
Figure 3.18. DIAL monitoring of molecular oxygen in ambient air. The laser beam is terminated against a hillside at about 1200-m distance. In the upper part of the figure on- and off-resonance curves are shown for O_2. The photomultiplier voltage has been ramped. In the lower part of the figure the DIAL curve is shown, following an exponential as expected for a uniform gas distribution. From Edner et al. (1991c).
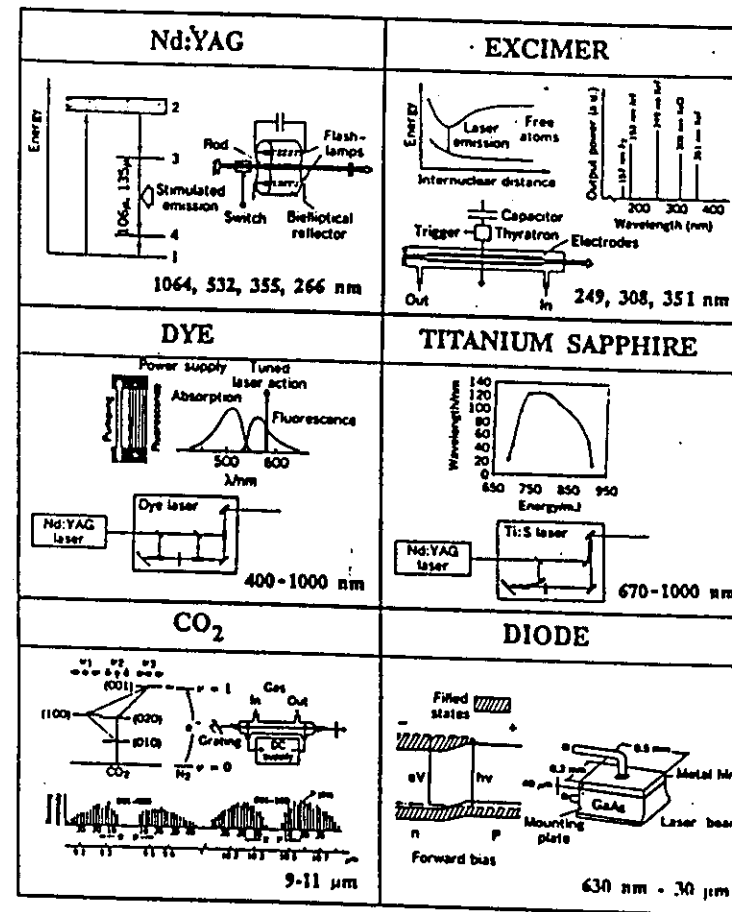

Figure 3.19. Construction and characteristics of six laser types of interest for DIAL measurements.

the excimer laser, are fixed-frequency lasers normally used as pumping sources for dye or titanium–sapphire lasers, which are widely tunable.

Laser sources are described in a number of textbooks (see, e.g., Siegman, 1986; Svelto, 1989; Svanberg, 1992).

3.4.1. The Nd:YAG Laser

The neodymium:YAG (yttrium aluminum garnet) laser is a highly efficient solid state laser using Nd^{3+} ions in a crystalline matrix. The Nd:YAG laser is a four-level laser with a broad absorption band that permits broad-band flashlamps to be used for pumping. The upper laser transition level has a long lifetime and permits storage of excess population. If a shutter is placed in the cavity, lasing can be prevented although population inversion has been reached. By opening the shutter when most of the pumping capacity of the lamp has been utilized, a giant pulse at $1.064 \mu m$ can be generated with megawatt power and about 10-ns pulse duration (Q-switching technique). In that way pulses with an energy of tens of millijoules can be formed. In order to achieve higher pulse energies the beam is passed through flashlamp-pumped amplifiers with laser rods of increasing diameter. In commercial Nd:YAG lasers used for lidar systems, one or two amplifiers are used to achieve pump energies well above 1 J. Repetition rates are 10–30 Hz.

By using phase-matched KDP (potassium dihydrogen phosphate) crystals, efficient frequency doubling, tripling, or quadrupling to 532, 355, or 266 nm, respectively, can be obtained. The doubled and tripled outputs are frequently used for pumping rhodamine and coumarin dyes in a dye laser for DIAL applications. The quadrupled output can be useful for ozone lidar systems, frequently in conjunction with stimulated Raman scattering in deuterium or hydrogen, producing outputs at 289 or 299 nm, respectively.

During the last few years high-power Nd:YAG lasers have become much more compact than they used to be, making them even more attractive for lidar use. Flashlamp quality has also greatly improved, allowing typically 20 million shots before replacement. Diode laser pumping of Nd:YAG lasers is quickly developing. Here pulsed diode lasers at 808 nm are used, matching a strong absorption line of the active medium. Small, very reliable units employing this all-solid-state technology are available. As the price of diode lasers continues to decline rapidly, high-energy lidar transmitters with strongly reduced power and cooling requirements will undoubtedly soon be available.

3.4.2 The Excimer Laser

Excimer lasers use noble-gas halogenides as the lasing medium. Such molecules can be formed in excited states in a fast discharge (thyratron switching)

in a mixture of Ar, Kr, or Xe with HCl or HF. Since the ground state is immediately dissociating, excimer molecules are ideal as laser media. In lidar contexts the XeCl excimer laser at 308 nm is important for pumping dye lasers for DIAL. The KrF laser at 249 nm is common for tropospheric ozone lidar systems, and is then frequently used in connection with stimulated Raman scattering in deuterium or hydrogen to produce 268-, 277-, 292-, or 313-nm output. For stratospheric ozone monitoring, less absorbed, longer wavelengths must be used, e.g., 308 nm from XeCl or 351 nm from XeF. In direct use of excimer lasers as lidar transmitters, a specially designed laser resonator (unstable resonator) is utilized to yield a much better beam quality than is available from excimer lasers for dye-laser pumping.

Excimer lasers yield pulse energies of hundreds of millijoules. An especially attractive feature is their high repetition rates (up to several hundred hertz). On the other hand, special installations and precautions are needed in the handling of very corrosive and toxic gases.

3.4.3. The Dye Laser

Dye lasers have long been the standard source in DIAL systems. The active medium consists of strongly fluorescing dye molecules, normally dissolved in methanol or ethanol. Flashlamp pumping in the broad absorption band of the dye can be used, but more frequently the harmonics of a Nd:YAG laser or a XeCl excimer laser is employed. The fire hazard in using direct flashlamp pumping of the flammable dye liquid as well as the comparatively long pulses are reasons for infrequent use of the direct pumping modality. In the dye laser oscillator normally a grating preceded by a prism beam expander is used for narrowing down the bandwidth and for tuning. For DIAL it is important to be able to change the wavelength between adjacent shots. It is not practical to turn the grating by using the normal sine-drive mechanics of the laser. Instead, a dual-wavelength option is frequently used in the laser. One possibility is to use a beamsplitter and direct half the laser mode toward one grating and the other half toward the second grating. The two arms are then alternatingly blocked for adjacent shots. Another, more convenient option is to have two gratings covering half of the expanded beam each. By alternatingly blocking the beam path in front of the gratings, every second shot can be fired at the preselected *on* and *off* wavelengths.

In order to achieve a sufficient pulse energy for long-range monitoring, one or two dye amplifier cells are normally used after the oscillator, as shown in Fig. 3.19. The dye amplifiers are pumped by the same pump laser, the output of which is split up in beams of suitable pulse energies. Rhodamine dyes are used to reach SO_2 and O_3 wavelengths around 300 nm after frequency doubling. Output powers of up to 200 mJ can be achieved at the dye's fundamental

wavelengths when green Nd:YAG laser pumping is employed. Blue and green dyes can be pumped by 355 nm output from a tripled Nd:YAG laser or conveniently directly and efficiently by a XeCl diode laser. In this way 450 nm for NO_2 or 226 and 254 nm after frequency doubling for NO and Hg, respectively, can be generated.

3.4.4. The Titanium–Sapphire Laser

Titanium–sapphire is a new tunable solid state laser material covering the wavelength region from 670 nm to about 1 μm. Since the upper state lifetime is only 3 μs, flashlamp pumping, although possible, is not very efficient. Frequently, frequency-doubled Nd:YAG laser is preferred for pumping. In order to get a high pulse energy, an end-pumped amplifier stage is frequently used. Commercial lasers of this kind have just become available and give considerable promise. NO_2 wavelengths are achieved by frequency doubling; SO_2, O_3, and Hg wavelengths, by frequency tripling; and NO wavelengths, by frequency quadrupling. Output pulse energies in oscillator/amplifier units can be similar to those achievable with dye lasers.

3.4.5. The CO_2 Laser

The carbon dioxide laser is a gas laser, emitting on a variety of vibrational-rotational lines of the CO_2 molecule in the 9–12 μm region. In the gas discharge tube nitrogen is added and pumping is provided by collisional exchange between ground-state CO_2 molecules and vibrational excited N_2 molecules. At the normal gas pressure of few torr the Doppler-broadened lines allow a very limited tuning of only 50 MHz and one has to rely on the accidental coinciding of pollution molecular absorption lines and the grating-selected laser lines. Many pollutants are accessible because of the richness of lines in the IR region. Frequently a CW seeder laser is employed when heterodyne detection is used in IR lidar systems.

The HF (hydrogen-fluoride) and DF (deuterium-fluoride) lasers are other pulsed gas lasers operating in the IR region. These lasers cover the 2.7–3.0 μm and 3.7–4.0 μm regions, respectively.

3.4.6. The Diode Laser

The diode laser is a highly efficient tunable solid state laser with very small dimensions. It consists of a highly doped p–n junction that is operated biased in the forward direction. The lasing occurs over the bandgap, the size of which varies for different materials. Normally, a resonator is provided by polishing the semiconductor chip surfaces. Better laser control is achieved by using an external resonator and coating the diode itself with an antireflection layer. We have discussed earlier the use of powerful 808-nm diode lasers for solid state laser pumping. Pulsed diode lasers are used in certain cloud height meters and range finders. CW units are used for seeding pulsed IR lasers and as local oscillators in heterodyne detection systems.

3.5. LIDAR SYSTEM DESIGN

A good DIAL system should be designed to be able to detect low gas concentrations at large ranges. Thus, signal intensity and signal noise are major concerns. Obviously, the detected backscattered intensity will increase with laser pulse energy, telescope area, and detector efficiency as indicated by the lidar equation. However, a lidar system can additionally strongly improve in sensitivity (particularly in the IR region) by introduction of heterodyne detection schemes instead of direct photon detection. A further aspect of major concern is the influence of the atmospheric turbulence (scintillation) in the lidar signals. Another technical consideration in laser radar system design is the need to be able to handle the large dynamic range typical for lidar signals. Before describing some DIAL systems in more detail we shall next address these general points.

3.5.1. Dynamic Range Reduction

A special signal-handling problem in lidar systems is that the backscattered intensity has a basic $1/R^2$ dependence. Thus, the detection system must be able to handle strong close-range signals at almost the same time as weak signals from afar. This calls for a very large dynamic-range capability that is hard to provide. Thus various methods to reduce the dynamic-range requirements have been developed.

By separating the axis of transmission from the detection telescope axis, the close-range signal is reduced since the transmission and detection lobes do not spatially overlap until a certain range. Even in a coaxial system a strong "geometrical compression" can be achieved (Harms et al., 1978; Harms, 1979) by introducing an aperture defining the telescope field of view in the far-field image plane of the telescope. The closer-range scattering volume will be imaged at larger distance from the telescope mirror and will thus be out of focus in the aperture plane. Only a fraction of the totally backscattered light can thus pass the aperture, reducing the close-range signal.

There are also electronic means to reduce the dynamic-range requirements for the detection system. One possibility is to use a logarithmic amplifier. A logarithmic representation was used above in Fig. 3.17. A further possibility

is to ramp the high voltage supplied to the photomultiplier dynode chain, triggering the ramp at the time of the pulse release. This was illustrated in Fig. 3.18. Maximum and constant amplification is provided after a time delay when the signal has decreased to a level that can be handled by the transient digitizer, i.e., one having a limited number of bits for the digitizing of the signal.

Geometrical compression, logarithmic amplification, and dynode-chain ramping all modify the recorded signal with regard to the lidar equation (3.4). However, since all curves are influenced in the same way, this problem is divided away when one is forming the DIAL ratio between the signals.

3.5.2. Heterodyne Detection

Heterodyne, or *coherent*, detection is a valuable scheme particularly in the IR region, where PMTs do not exist to provide strong and noise-free amplification (Menzies, 1976). Infrared detectors have a high efficiency but yield very low signal levels, calling for electronic amplification. This can easily induce additional noise. This can be circumvented in the heterodyne scheme, where the incoming signal amplitude A_S is mixed with the radiation of a narrow-band local oscillator with amplitude A_L on the detector, as shown Fig. 3.20. The detected signal S from the detector is the square of the resulting amplitude:

$$S = (A_S \cos \omega_S + A_L \cos \omega_L)^2$$

$$= A_S A_L \cos(\omega_S - \omega_L) + \text{(high-frequency terms)} \qquad (3.8)$$

Most terms in Eq. (3.8) oscillate at high optical frequencies (10^{13}–10^{14}). If the signal is passed through an electronic filter centered at the difference (intermediate) frequency $\omega_{IF} = \omega_S - \omega_L$, only the slowly oscillating component can pass. We note that this signal is proportional to the original signal amplitude A_S as well as to the local oscillator amplitude A_L, which can be increased arbitrarily for low-noise amplification. Since the signal is proportional to the square root of the normal lidar signal (A_S^2), heterodyne detection also handles
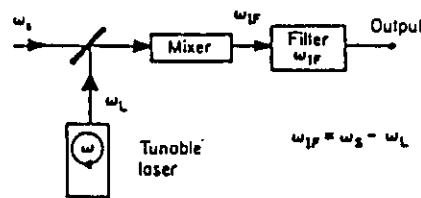

Figure 3.20. The principle of heterodyne detection.

the problems with dynamic range in an efficient way. Because coherence phenomena constitute an integrated part of heterodyne detection, it is important to adequately handle speckle noise through appropriate coherent lidar design.

By varying the local oscillator frequency or by analyzing the intermediate frequency spectrum, it is possible to detect Doppler shifts induced by movements of the backscattering particles. In this way it is possible to measure wind velocity with such a Doppler lidar system (Huffaker et al., 1984; Menzies, 1991). A wind speed of 1 m/s along the line of sight of the laser beam roughly corresponds to a frequency shift of 200 kHz at 10 μm wavelength.

An alternative way of measuring stratospheric wind speeds is to directly observe the Doppler shift in Rayleigh scattered narrow-band laser light. For this purpose Fabry–Pérot interferometers (Garnier and Chanin, 1992) or sharp atomic edge filters (Korb et al., 1992) are used on the detection side.

3.5.3. Atmospheric Turbulence

The useful range and the accuracy of a DIAL system will be limited by the number of backscattered photons detected by the system (the shot noise). However, even if a strong signal is obtained, the result is not necessarily accurate. This is related to the fact that lidar recordings have to be performed at both the *on* and *off* wavelengths (at least one and in general many lidar returns at each wavelength) in order to calculate the concentration from the DIAL curve. It is then very important that the atmospheric conditions remain the same to provide identical backscattering from particles and molecules. Because of atmospheric turbulence, as well as more macroscopic changes induced by winds (cloud and particle plume movements), such changes occur if the recordings for *on* and *off* wavelengths are not performed simultaneously. Then the curves are different for other reasons than for the presence of the gas to be studied, and erratic concentration values (even negative!) can be obtained. Simultaneous recording can in principle be performed by using two individually tuned lasers with overlapping beams. However, since the wavelength difference is normally chosen very small to avoid differential Mie scattering, it can be difficult to optically filter the two return signals in separate detection channels. By delaying one laser about 100 μs with respect to the other, the same detector and electronic transient digitizer can be used to detect the two laser returns. Experiments have shown (Killinger and Menyuk, 1981) that the time structure of turbulence is such that the atmosphere is practically "frozen" if the recordings are made within 1 ms. Since in many DIAL systems, many on- and off-resonance shots are averaged in separate memories, atmospheric movements are averaged out and no systematic error is made. Still the noise level increases owing to the turbulence. However, since the lidar curves

are frequently evaluated out to maximum range, the signal becomes photon limited and the turbulence is in practice found to be no serious limitation even if a single laser is used at a repetition rate of 10–100 Hz, firing on, on- and off-resonance wavelengths every second shot. For such systems, changes in the DIAL curve larger than 1% can be considered significant. Thus, this number for differential absorption can form a basis for a calculation of the DIAL detectivity for different pollutants, as further discussed below (see Table 3.1 in Section 3.6.6). In order to test the proper performance of a DIAL system, a DIAL measurement and data evaluation can be performed without actually changing the wavelength of the laser between the shots. Clearly, a zero concentration value should be obtained for all range intervals. The size of nonzero concentration readings (positive or negative!) indicates the uncertainty in the particular measurement situation.

The problem of spectrally separating the on- and off-resonance signals can be solved in the gas correlation lidar technique (Edner et al., 1984). Gas correlation techniques for passive atmospheric monitoring have been described by Ward and Zwick (1975) and Lee and Zwick (1985). The principle of gas correlation lidar is shown in Fig. 3.21. A rather crude laser system with a comparatively broad line width is utilized. Since the laser wavelength is not sharp, it covers both on- and off-resonance wavelengths at the same time. However, the information for on- and off-resonance wavelengths can be separated on the detection side by splitting the received radiation into two parts. One part is detected directly, whereas the other part is first passed through a cell filled with an optically thick sample of the gas to be studied. In this way all the on-resonance radiation is filtered away, leaving only the off-resonance radiation to be detected. In the direct channel the sum of the on- and off-resonance radiation is detected. Unknown factors are eliminated by dividing the signals. The simultaneous detection of the two signals eliminates influences due to atmospheric turbulence and fluctuations due to changing reflectivity in airborne measurements using the ground as a topographic target.

3.5.4. Fixed DIAL System Design

Differential absorption lidar systems can be arranged with different degrees of versatility and complexity. Fixed systems frequently can have a simpler design than mobile systems. In particular, electricity and cooling demands can be met using the normal utilities available in laboratories. We will start with a description of a vertically looking ozone lidar system with a layout as shown in Fig. 3.22 (Edner et al., 1991a). Since the ozone molecule does not exhibit a strongly structured spectrum but rather only a gradually increasing absorption from 320 to 260 nm, it is necessary to place the on- and off-resonance
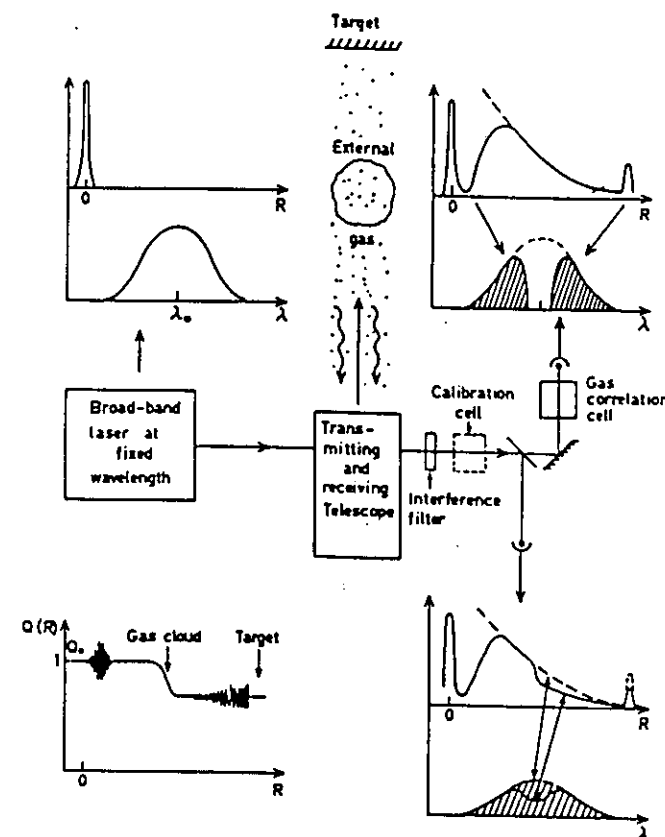

Figure 3.21. Gas correlation lidar. From Edner et al. (1984).

wavelengths much further apart than would normally be the case for DIAL. The absorption spectrum of ozone is shown in Fig. 3.23. Since there are no sharp structures, a continuously tunable laser is not needed but rather a step-tunable system. This can be achieved by an excimer laser or a frequency-quadrupled Nd:YAG laser in combination with stimulated Raman shifting. When a KrF laser is used the primary emission occurs at 249 nm whereas the quadrupled YAG emission occurs at 266 nm. The positions of the Stokes-
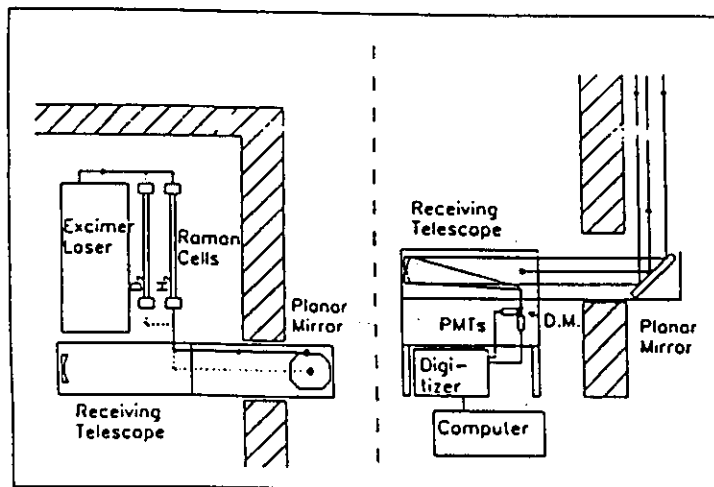
Figure 3.22. A fixed ozone lidar system based on an excimer laser. From Edner et al. (1991a).
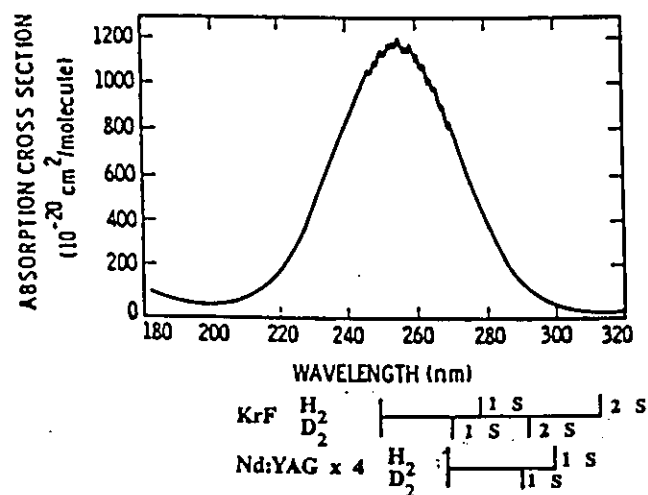

Figure 3.23. The ozone absorption cross section in the short-wavelength region, with fixed-frequency laser lines indicated. From Molina and Molina (1986).

shifted component obtained with hydrogen or deuterium in the Raman converting cell are indicated in Fig. 3.23.

The system shown in Fig. 3.22 uses a KrF laser (pulse energy, 300 mJ; repetition rate, 100 Hz) and incorporates two Raman cells, one filled with hydrogen and one filled with deuterium (Raman shifts 4155 and 2987 cm^{-1} for H_2 and D_2, respectively. In the system the first and second Stokes components from H_2 at 277 and 313 nm are normally utilized and are transmitted together with the primary excimer radiation via a first surface aluminized mirror vertically into the atmosphere. Backscattered radiation is reflected via the same mirror into a horizontally looking telescope using a 30-cm-diameter off-axis parabolic aluminized mirror. A dichroic mirror is used to direct the two Stokes components into separate photomultiplier tubes, mounted behind narrow-band interference filters. In this system the on- and off-resonance wavelengths can be transmitted and recorded separately because of the large wavelength separation. Each photomultiplier is connected to an input channel of a digital oscilloscope where the transients are averaged for many laser pulses. The data are transferred into a personal computer, where the DIAL curve is formed. A practical range of about 2 km is obtained.

As a further example of a fixed lidar system a CO_2-laser-based system operated by ENEA (Comitato Nazionale per la Ricerca e per lo Sviluppo dell' Energia Nucleare e delle Energie Alternative) at Frascati, Italy; is chosen (Barbini et al., 1991). A schematic diagram of the system is shown in Fig. 3.24. Two line-tuned pulsed CO_2 lasers generating 80-ns-long pulses with energy up to 4 J are used, tuned to the on- and off-resonance wavelengths, respectively. The lasers are fired close in time for freezing the atmospheric conditions as discussed above. The two laser beams are sent along the rotation axes of the telescope, which is mounted in a dome at the top of a 5-m-high tower. By this arrangement it is possible to keep the overlap between the transmission and detection lobes. The radiation is detected by a HgCdTe detector cooled to 77 K. This system is used for mapping of H_2O and O_3 and has a range of about 5 km for spatially resolved measurements.

3.5.5. Mobile DIAL System Design

Mobile DIAL systems are very versatile for research and operational measurements. A number of efficient systems have been constructed (see e.g., Hawley et al., 1983; Jolliffe et al., 1987; Staer et al., 1984; Fredriksson et al., 1981; Edner et al., 1987b; Wolf et al., 1990; Zanzottera, 1990). In Fig. 3.25 two Swedish systems of similar layout are shown, one constructed at the Chalmers Institute of Technology (Fredriksson et al., 1981) and the other one at the Lund Institute of Technology (Edner et al., 1987b). A photograph of the newer and larger system during measurements in an industrial area is shown in Fig. 3.26.
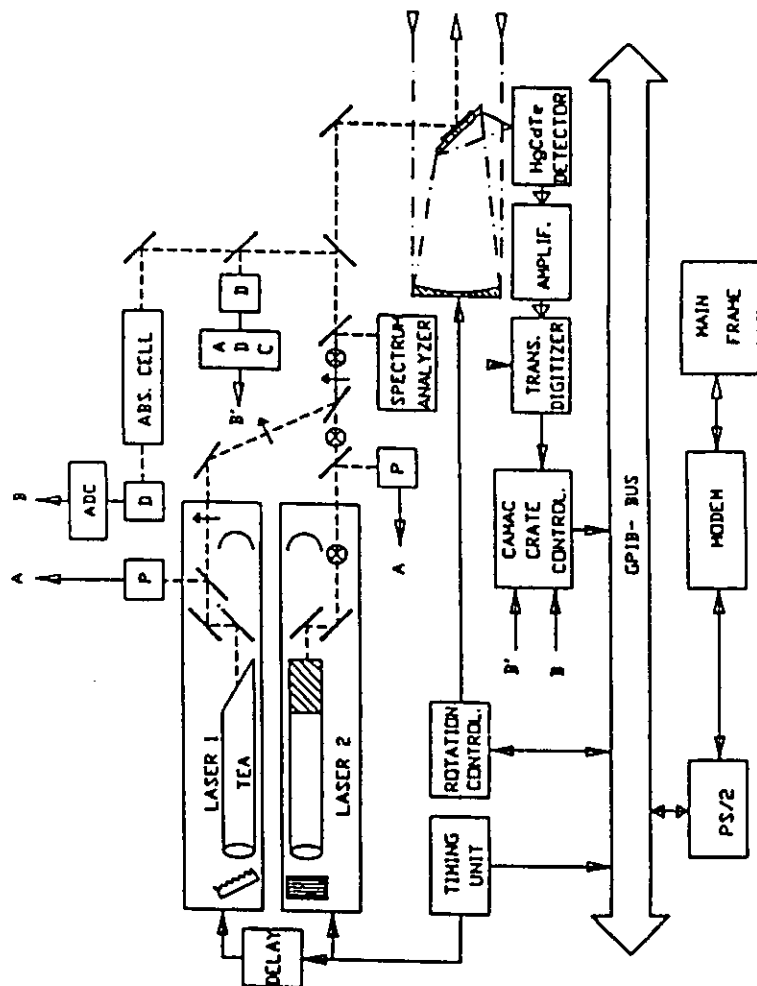
Figure 3.24. Layout of a CO_2 DIAL system. Key: ADC, analog-to-digital converter; D, detector; P, power meter; Ps/2 computer. From Barbini et al. (1991).
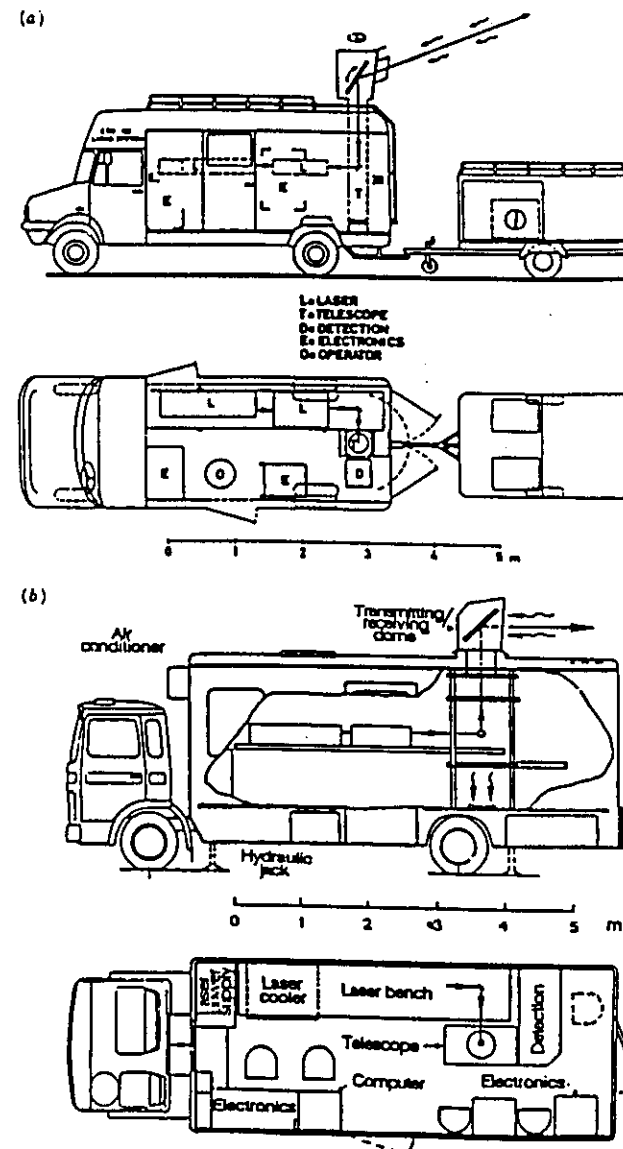
L = LASER
T = TELESCOPE
D = DETECTION
E = ELECTRONICS
O = OPERATOR

Air conditioner

Transmitting/ receiving dome

Hydraulic jack

Laser cooler

Laser bench

Telescope

Detection

Electronics

Computer

Electronics

Figure 3.25. Two Swedish mobile DIAL systems (a,b) From Fredriksson et al. (1981) and Edner et al. (1987b), respectively.

Figure 3.26. Photograph of the newer Swedish mobile lidar system.

A schematic of the optical arrangements in the older system is shown in Fig. 3.27. The new system is similar but uses updated optics and electronics.

Nd:YAG lasers are used as transmitters in the Swedish DIAL systems. The pulse energy at 10 Hz at the fundamental wavelength was 250 mJ in the original system of 1981. By using frequency conversion in nonlinear crystals, 100-mJ pulses at 532 nm (the second harmonic) and 50-mJ pulses at 355 nm (the third harmonic) could then be generated. Since that time, laser technology has been greatly improved. In the new system operating at 20 Hz the fundamental pulse energy is presently 1.200 J, with 500 mJ at 532 nm and 200 mJ at 355 nm. The frequency-doubled output is used to pump yellow and red rhodamine dyes in a dye laser in order to reach UV wavelengths around 300 nm for DIAL measurements of SO_2 and O_3. The frequency-tripled radiation is used to pump blue stilbene and coumarin dyes for reaching NO_2 wavelengths, and after frequency doubling NO and Hg wavelengths. Arrangements are made to provide fast wavelength switching from on- to off-resonance wavelengths every second laser shot. In the older system this is made by rocking the laser oscillator grating by employing a stepper-motor-driven eccentric wheel acting on a cam on the grating mount. In the newer system two independently set gratings are used in the oscillator and a rotating quartz block in used to engage one or the other grating for alternate laser shots.

For high pulse energies the laser beam is expanded in a Galilean telescope with one negative and one positive lens to reduce the beam power density before hitting the system steering mirror. (A Newtonian telescope cannot be used since air breakdown is obtained in the focus between the two positive lenses.) The laser beam is sent vertically and coaxially with the receiving telescope toward a large first surface aluminum folding mirror used to direct
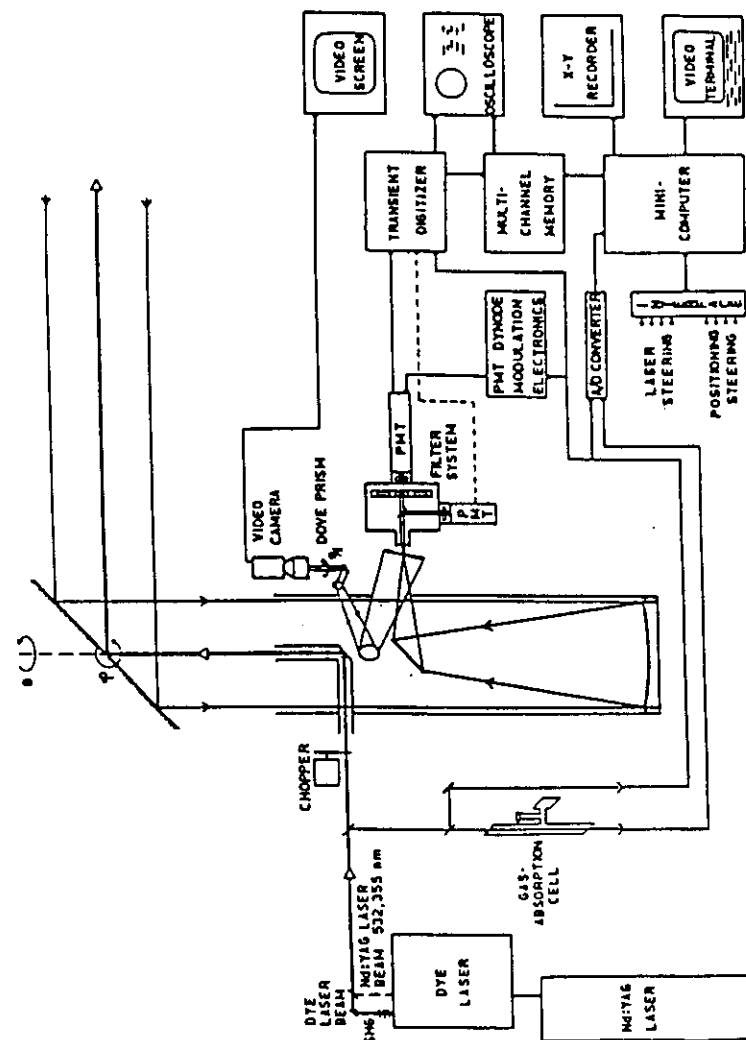

Figure 3.27. DIAL system optical and electronic layout. From Fredriksson et al. (1981).
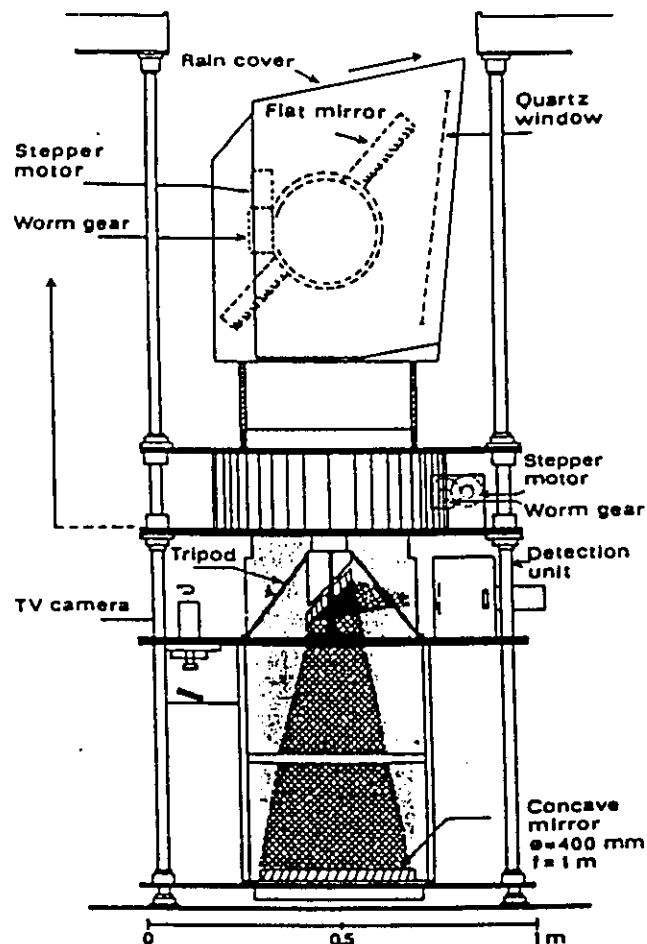
Figure 3.28. Arrangement with receiver telescope and retractable mirror dome in mobile DIAL system. The dome is shown in its retracted position. From Edner et al. (1987b).

the laser beam into the measurement direction. The mirror is placed in a dome equipped with a large quartz window, sealing off the lidar system toward the outdoor weather conditions. The dome rotation and the mirror vertical positioning are computer controlled via powerful stepper motors. In Fig. 3.28 the layout of the telescope/dome arrangement of the newer system is shown. In order to reduce the overall height of the mobile system during transport, the dome can be retracted into the laboratory as shown in the figure. This also improves the serviceability of the dome construction. A motorized cover can be moved forward for rain protection of the quartz window once the dome has been hoisted out of the roof orifice into operating position.

Light backscattered from the atmosphere or from topographic targets passes into the system via the quartz window and is directed via the folding mirror down into a vertical Newtonian telescope that has a diameter of 30 cm in the older system and 40 cm in the newer system. The telescope mirrors are spherical (for cost reasons) rather than parabolic. Via a secondary mirror the light is focused toward an image plane, where an aperture is placed defining the telescope field of view. With a telescope focal length of 1 m an aperture diameter of 2 mm corresponds to a telescope field of view of 2 mrad, matching a typical laser beam divergence. A small beam divergence and a correspondingly small telescope field of view is desirable in order to achieve rejection of ambient light, competing with the laser-induced signal during daytime operation. This is not an important consideration below 300 nm, where the stratospheric ozone layer provides an efficient cutoff of background radiation. The vertical telescope arrangement with a rooftop steering mirror has the following important advantages over most other constructions:

- 360° horizontal scanning capability
- Eye-safe near-field operation, with the laser beam leaving system high above the ground
- Easy optical alignment
- Space-saving arrangement in the mobile laboratory
- Easy weather protection

On the other hand, high elevation angles cannot be used. For vertical sounding the whole dome can be dismantled or, more conveniently, a fixed 45° mirror be used in front of the quartz window.

The aperture is arranged as a hole in a polished metal mirror that directs all light, except the signal photons passing the aperture, toward a ccd camera that displays sharply the target area except a black spot at the position of the laser beam. Such an arrangement is very useful for swift and accurate positioning of the measuring beam. When the dome is rotated, the TV image will also rotate

unless counter measures are taken. In the older system the TV camera is preceded by a Dove prism that is rotated with half the angular speed relative to the dome rotation. In the newer system the whole TV camera is rotated synchronously with the dome rotation.

When the stepper motors are activated, 10-turn precision potentiometers are also turned to generate analog voltages that are compared with set voltages defining the limits of allowed firing directions. If these limits are accidently passed, e.g., owing to computer or operator failure, the laser firing is inhibited. Such a system is an additional security measure when non-eye-safe wavelengths are used (see also Section 3.5.7).

The light that passes the aperture is collimated by means of a lens. A narrow-band high-transmission interference filter centered at the laser wavelength is used to reject daylight. A number of interference filters corresponding to different pollutants (wavelengths) are mounted on a filter wheel. The optical transient is converted into an electrical transient in a PMT. In order to reduce the dynamic range requirements the PMT voltage is ramped as discussed in Section 3.5.1. In this way the close-range intensity is reduced. Beyond about 600 m the true signal shape is obtained.

The transients from the PMT are fed to a transient digitizer, which is a critical component in a DIAL system. The transient digitizer normally has an 8-bit resolution (256 intensity levels), a very limited value, which is the origin of the dynamic range reduction needs. For tropospheric air pollution monitoring the separation between the temporal channels in the transient digitizer is 10 ns, which corresponds to a range interval of 1.5 m, matching a commonly used laser pulse length of 10 ns. The data string of numbers from the transient digitizer is fed to a personal computer. The on- and off-resonance transients are added in separate memories. In the older system a separate hardware signal averager was used since the computers were not fast enough to directly handle the data stream. Before one forms the DIAL curve by division of the on- and off-resonance curves, it is important to subtract the background intensity due to the ambient light and the PMT dark current. This is done by automatically blocking the laser beam every ninth shot and subtracting this signal multiplied by 8 from the intensity collected during the eight previous shots. This is done for the on- as well as the off-resonance wavelengths.

For a given measurement direction normally 50 data collection cycles as described above are used, corresponding to 400 transients for each wavelength. Then the DIAL curve as the ratio of the on- and off-resonance curves is formed. From the DIAL curve the range-resolved concentration curve is then calculated for the given measurement direction using Eq. (3.6). Examples of this process were already given in Figs. 3.17 and 3.18. A new measurement direction can then be chosen, and the procedure is repeated. After the final measurement direction is finished, the procedure can be

repeated if it is desired to form more representative averages. Finally, a concentration map can be calculated from all the collected data. We shall return to this process in Section 3.6.

To make the mobile system fully self-contained and operational, a motor generator on a trailer is brought along. The new system is equipped with a 20-kV·A diesel-powered unit, amply covering the demands of the system. Apart from the laser, particularly energy-consuming units are a closed-loop cooler for the laser and the laboratory air-conditioning system. The new system is also equipped with four hydraulically operated supporting legs that, when in use, fully stabilize the mobile laboratory for accurate beam pointing.

3.5.6. Airborne DIAL System Design

Airborne DIAL systems provide monitoring of gas constituents over wide areas. Such systems are normally looking downward or upward in a fixed position, but scanning systems utilizing a laterally moving mirror can also be used. Because of the swift movement, special requirements as to high repetition rates pertain. Furthermore, it is necessary that the on- and off-resonance pulses be fired simultaneously or with very small temporal spacing, since the atmospheric backscattering conditions otherwise certainly would be changed. For airborne operation, weight and power consumption are normally also critical factors.

The layout of an airborne DIAL system operated by NASA is shown in Fig. 3.29 (Browell et al., 1983; Browell, 1991). The system utilizes two individually Nd:YAG pumped dye lasers, firing with a temporal separation of 100 μs. The laser beams are split into two equal parts, one transmitted toward the nadir and one transmitted toward the zenith. Correspondingly, two receiving telescopes are operated back to back. The system is capable of large area mapping of particles, ozone, and water vapor.

3.5.7. Eye Safety

DIAL systems are operated in the open environment, and it is necessary that the measurements be performed in such a way that eye damage will not occur to persons in the operating zone of the system. The safe use of lasers is regulated by American standards, which have also been adopted in most other countries (ANSI, 1986; Sliney and Wolbarsht, 1980). Of special concern is the spectral region from 400 to 1400 nm, where the cornea is transparent and the radiation is focused onto a small spot on the retina. Outside this region the radiation is absorbed before reaching the retina and the irradiation threshold values are relaxed by a factor of 1000. With a normal laser beam divergence of a few milliradians the UV laser beam for NO, Hg, O_3, or SO_2 measurements is

eye-safe for distances beyond 100 m or shorter. Combined with rooftop transmission from mobile systems, UV DIAL measurements give little safety concern. For NO_2 monitoring in the blue region the eye safety distance is several kilometers and special precautions must be taken with continuous beam-path monitoring during measurements. Special consideration must be given to the possible use of binoculars by ground observers of a lidar airborne system.

3.6. DIAL MONITORING OF TROPOSPHERIC GASES

In this section we shall give several examples of DIAL monitoring of atmospheric gases. Most of the examples concern measurements of industrial pollution. The measurements are performed with DIAL systems as described in the previous section.

3.6.1. SO_2 Monitoring

Sulfur dioxide is one of the most important pollutants produced in the burning of fossil fuels. The amount of SO_2 produced is directly related to the sulfur contents in the fuel. In the atmosphere the gas is converted into sulfuric acid and sulfate particles largely responsible for acidification of certain areas. The absorption spectrum of SO_2 is prominent in the region around 300 nm, as shown in Fig. 3.5. There also the most common wavelength pair utilized in DIAL measurements is indicated.

The DIAL technique is very powerful for determining the total flux of a pollutant from an industrial plant. This can be done by making a vertical scan with the lidar system beam through the atmosphere downwind from the plant. In this way not only the stack emissions are captured but also the diffuse emissions from ventilators and leaking valves. Such a downwind recording at a Swedish pulp mill is shown in Fig. 3.30. The DIAL curves recorded in different directions are automatically evaluated on the system computer, and the concentrations are represented on a type of gray scale. Data were collected for a total time of 20 min. The area integrated concentration value N_A can be calculated from the data in the figure. By multiplying this value with the wind velocity component perpendicular to the measurement plane, the total flux F_{tot} from the industry can be determined:

$$F_{tot} \, [\text{kg/s}] = N_A \, [(\text{kg/m}^3) \cdot m^2] \cdot v_{\perp} \, [\text{m/s}] = \int_A N \, da \cdot v \cos \phi \, [\text{kg/s}] \quad (3.9)$$

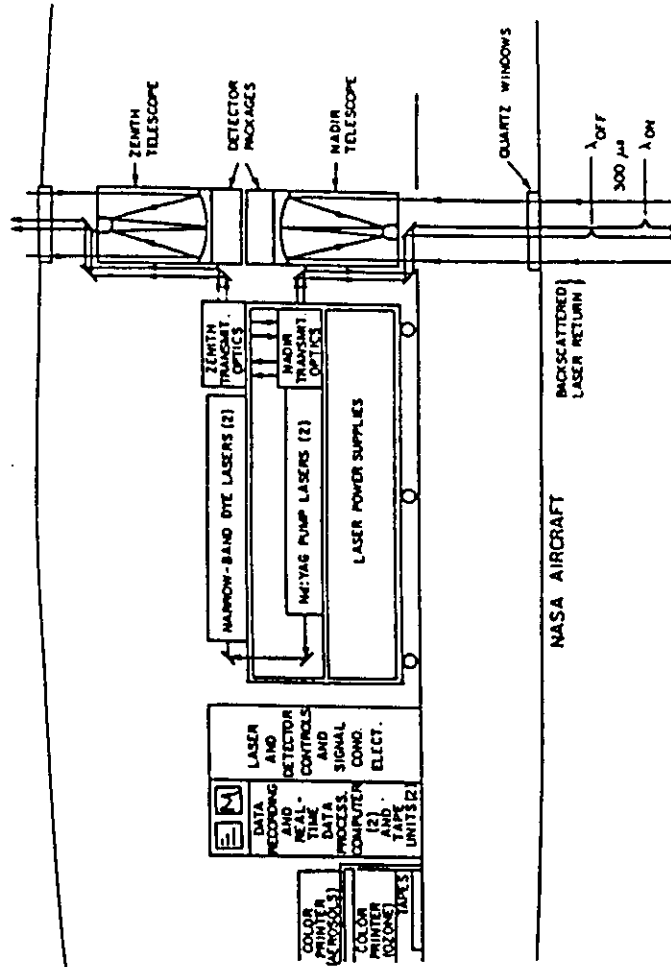where ϕ is the angle between the measurement direction and the direction

Figure 3.29. The NASA [National Aeronautical and Space Administration (U.S.)] airborne DIAL system. From Browell (1991).
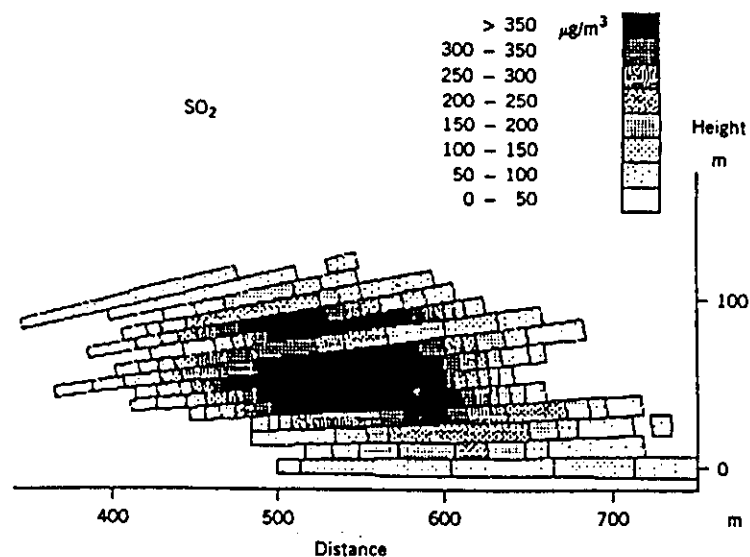
Figure 3.30. SO₂ plume scan at a Swedish pulp mill. From Edner et al. (1987b).

perpendicular to the plume. For accurate flux determinations it is obviously as important to make a correct wind velocity measurement as to perform the DIAL measurements correctly. For the measurement situation shown in Fig. 3.30 an hourly flux of 230 kg is estimated.

Since wavelengths for DIAL SO₂ monitoring are obtained by frequency doubling of very efficient rhodamine dyes, high-energy laser pulses can be obtained and thus a substantial range is available. This is illustrated in Fig. 3.31, where on- and off-resonance curves and the corresponding DIAL curves are shown for a horizontal range out to 4 km. At a distance of about 3 km thin clouds were encountered, but the signal was retrieved also after the clouds were passed. The recording was performed as part of a study of a possible conversion of H₂S into SO₂ downwind from an Icelandic geothermal field. The SO₂ concentration was found to be very low and did not increase for larger ranges and correspondingly longer times available for atmospheric chemistry to take place.

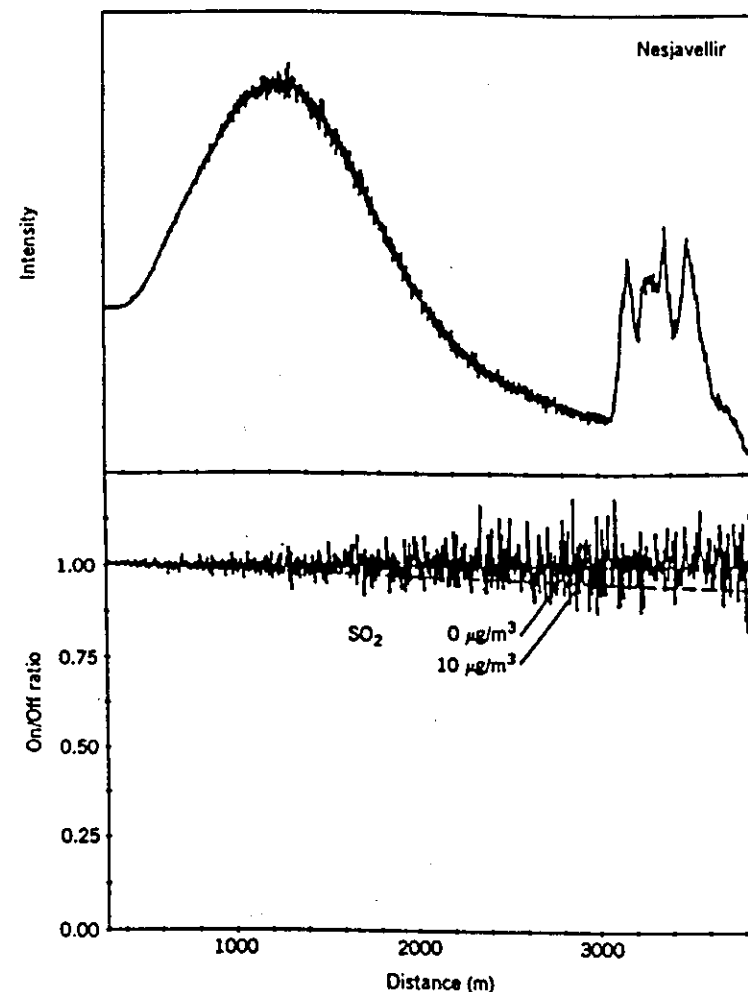Various aspects of practical SO₂ monitoring have been discussed by Egebäck et al. (1984).

Figure 3.31. Long-range SO₂ lidar recordings (at Nesjavellir, Iceland) for on- and off-resonance wavelengths and corresponding divided (DIAL) curve. From Edner et al. (1991c).

3.6.2 O₃ Monitoring

Great attention is presently being focused on the ozone molecule. A steadily increasing concentration of tropospheric ozone is thought to be at least partially related to the increasing damage to forests observed throughout Europe. The stratospheric ozone layer is being depleted, most likely because of chemical reactions with fluorinated hydrocarbons (Freons). Measurements of stratospheric ozone have been performed by many groups (Werner et al., 1983; Uchino et al., 1983; Megie et al., 1985; Browell et al., 1990; Stefanutti et al., 1992a). In order to reach stratospheric heights, lidar systems with high pulse energies ($\simeq$ 1 J), large telescope diameters ($\simeq$ 1 m), and photon-counting detection electronics are needed. For stratospheric measurements it is necessary to use wavelengths that are only weakly absorbed by ozone (long wavelengths) in order to avoid excessive absorption already at lower heights. As discussed in Section 3.2.1 a special problem with O₃ monitoring is the need for a wide wavelength separation, necessitating a correction to be applied for different Mie scattering at the different wavelengths (Browell, 1985). This correction is particularly critical when particle layers are being passed, e.g., at the tropopause. DIAL data for tropospheric ozone are shown in Fig. 3.32 (Edner et al., 1992b). Here the new Swedish mobile DIAL system was used at high elevation angles. The range- and angle-resolved data can be converted into a vertical profile as shown in the figure.

3.6.3. NO₂ Monitoring

Nitrogen oxide (NO) is formed in all high-temperature combustion and is an important pollutant from industrial activities and, in particular, from automotive traffic. Shortly after the emission of NO into the atmosphere this molecule is oxidized into NO₂ and further on to HNO₃, which contributes to water and soil acidification. NO₂ absorbs in blue spectral region and was the first pollutant to be measured by the DIAL technique (Rothe et al., 1974a, b; Grant et al., 1974). Recordings for NO₂ have already been shown in Fig. 3.17.

Practical NO₂ monitoring by DIAL techniques has been discussed by Fredriksson and Hertz (1984).

3.6.4. NO Monitoring

The NO molecule has a strong absorption band, the γ-band at short UV wavelengths, as shown in Fig. 3.33. First atmospheric UV lidar measurements were reported by Aldén et al. (1982b), who used stimulated Raman scattering to produce the required radiation. For DIAL plume mapping of NO frequency mixing was employed, first generating 575 nm by dye radiation frequency
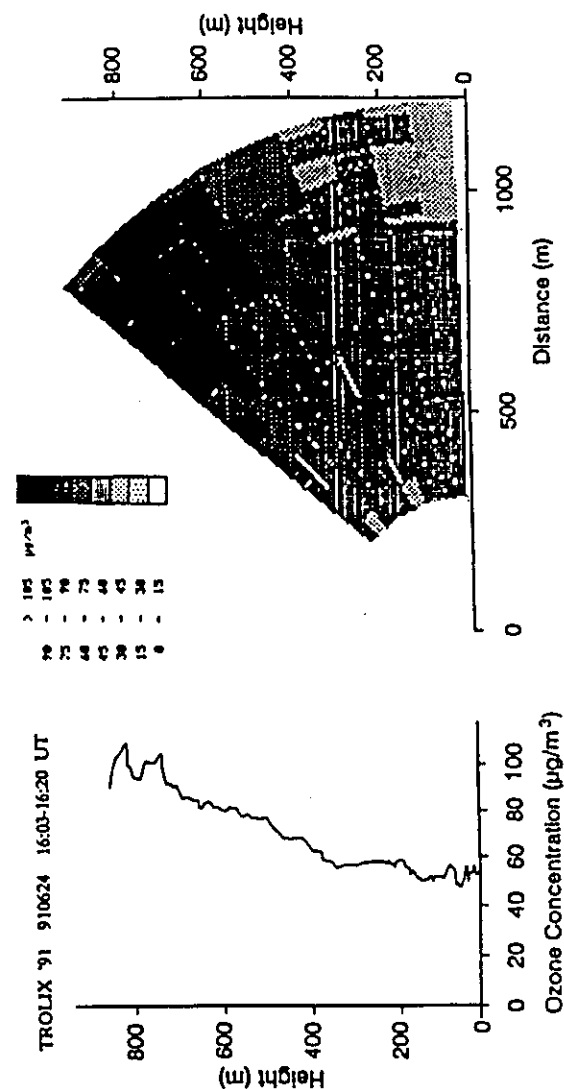
Figure 3.32 Vertical ozone sounding with a mobile dye-laser-based DIAL system. From the vertical lidar sweep a vertical ozone profile has been evaluated. From Edner et al. (1992b)
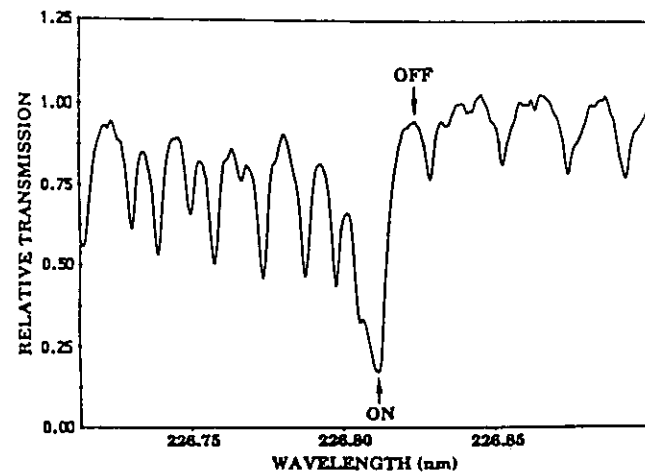
Figure 3.33. NO absorption spectrum with DIAL wavelengths indicated. From Edner et al. (1988).
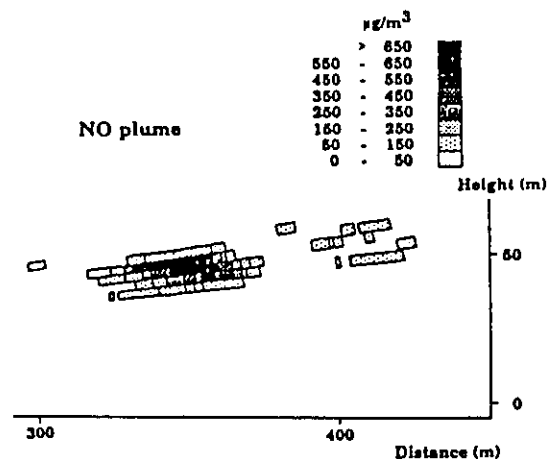

Figure 3.34. Vertical NO scan through the plume from a small heating plant. From Edner et al. (1988).

doubling and then mixing with residual fundamental Nd:YAG radiation in a second KDP crystal to reach 226 nm (Edner et al., 1988; Jolliffe et al., 1987). The result from a vertical scan downwind from a smokestack is seen in Fig. 3.34.

Since NO absorbs at approximately half the wavelength on NO_2, it is possible to measure the two gases simultaneously using the same frequency-doubled laser (Nickolov and Svanberg, 1986). The low conversion efficiency of the KPB (potassium pentaborate) frequency-doubling crystal was initially a drawback but with the occurrence of the new nonlinear material BBO (β-barium borate) double species monitoring became very realistic. Such measurements have been reported by Kölsch et al. (1989).

3.6.5. Monitoring of Other Gases

DIAL monitoring of a number of other pollutant gases has also been demonstrated, although the techniques may be less operational than for SO_2, O_3, NO_2, NO, and Hg. DIAL monitoring of toluene and benzene at 267 and 253 nm, respectively, has recently been reported (Milton et al., 1992). Molecular chlorine (Cl_2) exhibits a broad absorption spectrum in the UV region. Like for ozone it is necessary to have a sufficiently large wavelength separation in the DIAL measurements. A demonstration of DIAL measurements on an artificial chlorine cloud has been made by Edner et al. (1987a). HCl emitted from incineration ships has been monitored by Weitkamp (1981) using a DF laser transmitter at 3.6 μm. By using frequency mixing techniques, wavelengths around 5 μm could be produced by CO_2 lasers, allowing DIAL monitoring of CO (Killinger et al., 1980), NO (Menyuk et al., 1980), and hydrazine and other fuels (Menyuk et al., 1982). Hydrocarbons can be measured at the CH-stretch wavelength 3.4 μm, and practical DIAL measurements have been performed by Milton et al. (1988). Special, simplified systems have also been constructed for CH_4 detection, i.e., from leaking natural gas pipelines. In one system the gas correlation lidar technique (discussed in Section 3.5.3) was employed for methane leak detection (Galetti, 1987). Several demonstrations of direct and heterodyne DIAL monitoring at CO_2 laser wavelengths ($\approx$ 10 μm) have been made covering species such as Freon-12, ethylene, ozone, ammonia, and sulfur hexafluoride (see, e.g., Grant, 1989).

3.6.6. Sensitivity and Detection Limits of DIAL

Preferred wavelength regions, differential absorption cross sections, and detection limits in ppb for a 100-m measuring path are given in Table 3.1 for pollutants for which realistic DIAL measurements can be performed. The detection limits correspond to a 1% change in the DIAL curve over the range

Table 3.1. Important DIAL Detected Pollutants with Detection Limits for a 100-m Measurement Interval (200-m Absorption Path)[a]

Gas	Wavelength	Differential Cross (atm^{-1}·cm^{-1})	Detection Limit (ppb)
NO	226 nm	100	5
Benzene	253 nm	61	8
Hg	254 nm	670,000	0.001
Toluene	267 nm	30	17
O_3	280 nm	30	9
SO_2	299 nm	25	20
NO_2	450 nm	10	50
HCl	3.6 μm	6	90
C_2H_4	10 μm	31	16

[a] Only rough values are given. Differential cross-sections' depend on details in wavelength-pair, choice, laser line width, etc.

interval chosen. Many other gases can be studied, but the experience with such measurements might be less extensive. The table is given to provide the reader with a realistic assessment of the practical applicability of the DIAL technique.

3.7. SPECIAL CASE STUDY: ATOMIC MERCURY MONITORING

Mercury is a troublesome pollutant that is unique in the atmosphere, as it is mainly present in atomic form (Jepsen, 1973). All other pollutants are molecules, for which each electronic transition is accompanied by thousands of vibrational–rotational transitions, giving rise to a distributed band spectrum. For an atom the electronic transition probability (oscillator strength) is instead concentrated in a single line, or at least in a low number of isotopic and hyperfine-structure lines, which because of Doppler and collisional broadening appear as a single line. Because of this the DIAL detection limit for Hg is about 3 orders of magnitude lower than for other pollutants such as SO_2 or NO_2. When these latter pollutants can be detected on the ppb level, mercury can be detected at ppt concentrations. That is exactly what is needed, since atomic mercury has an Atlantic background concentration of about 0.25 ppt or 2 ng/m^3 (Slemr et al., 1981).

Locally increased amounts of mercury in the air can be caused by industrial activities such as chlorine-alkali plants, where liquid mercury electrodes are used. Mercury is also emitted from coal-fired power plants as well as from incineration plants. Recently attention has been given to strong mercury emissions from crematoria, which in some countries give rise to more mercury pollution than normal incineration plants. As a toxic heavy metal, mercury and its cycle in the environment have been much studied (see, e.g., Ngriau, 1979; Mitra, 1986; Lindqvist, 1991).

Apart from being a pollutant caused by human activities, mercury is a very interesting geophysical tracer gas associated with ore deposits (Bristow and Jonasson, 1972; McCarthy, 1972), geothermal energy (Robertson et al., 1977; Varekamp and Buseck, 1983), and seismic and volcanic phenomena (Varekamp and Buseck, 1981). These latter aspects are illustrated in Fig. 3.35 (Svanberg, 1991).

The mercury resonance line ($6s^1S_0-6p^3P_1$) occurs at 253.65 nm. Its width and shape at ambient atmospheric conditions are shown in the cell absorption spectrum in Fig. 3.36. There also the isotopic contributions to the Hg line shape are indicated and neighboring "forbidden" absorption lines of molecular oxygen are shown (see also Fig. 3.18). First attempts to remotely monitor mercury were made using anti-Stokes Raman shifting of frequency-doubled dye laser radiation (Aldén et al., 1982a). On- and off-resonance curves and a
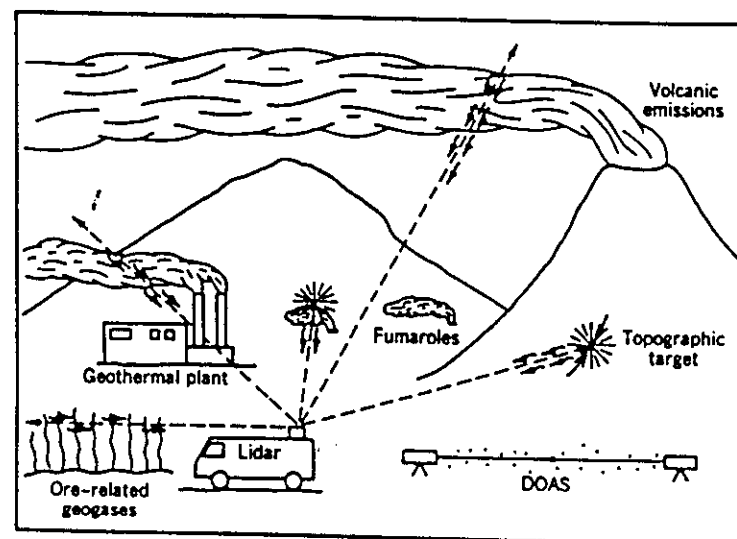

Figure 3.35. Measurement scenarios for atomic mercury of geophysical origin. From Svanberg (1991).
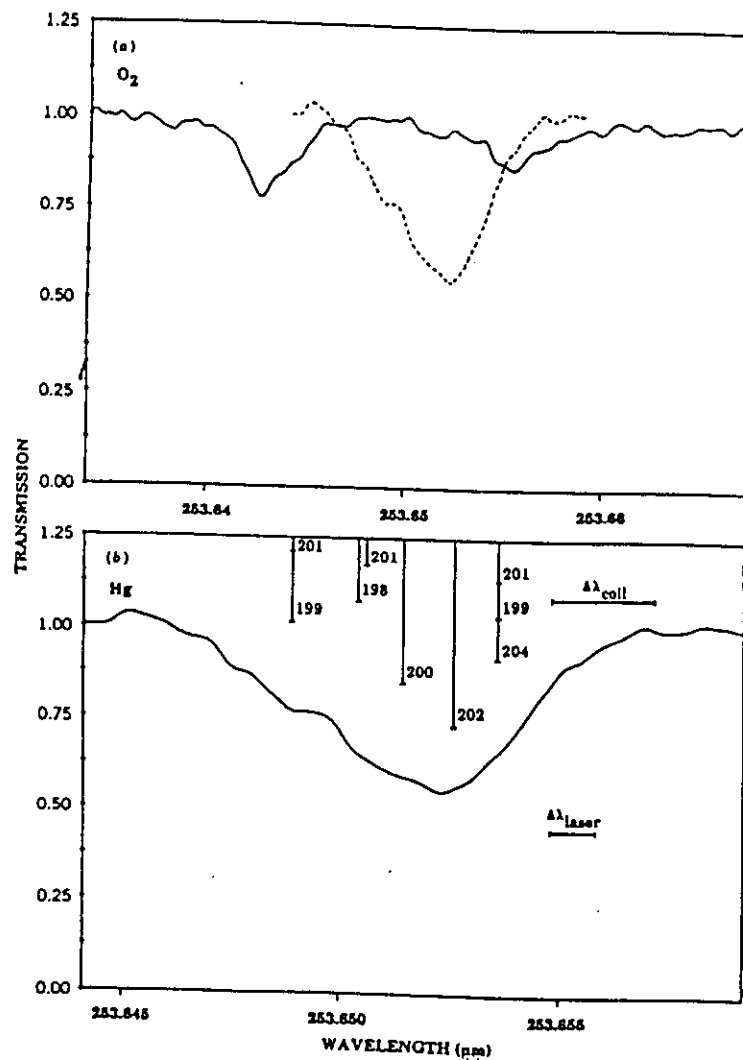
Figure 3.36. Laboratory recording of the atomic mercury absorption line: in (a) oxygen "forbidden" lines are also shown: in (b) the isotopic contributions to the line shape are shown. From Edner et al. (1989).
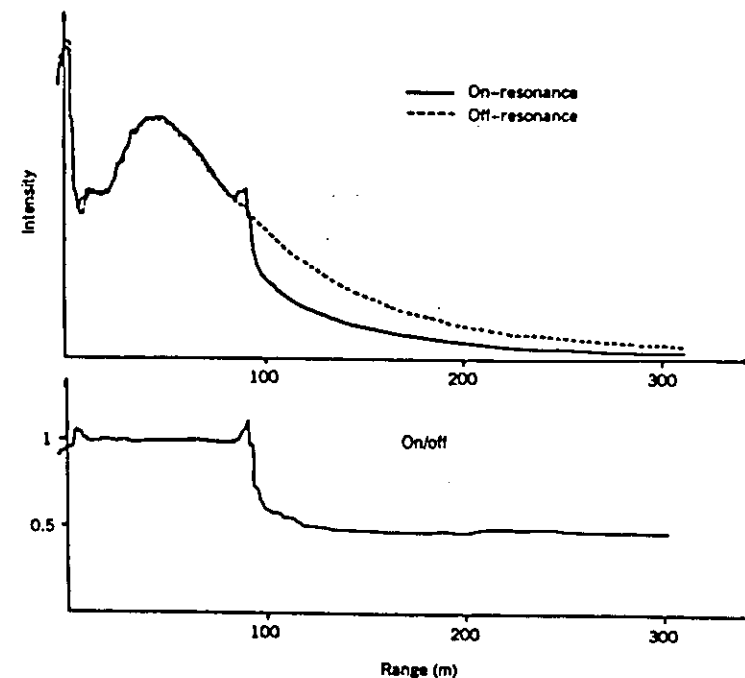

Figure 3.37. On- and off-resonance Hg lidar curves for an artifical mercury cloud at about 100-m distance. Note the fluorescence emission peak in the on-resonance curve. In the lower part of the figure the divided (DIAL) curve is shown From Aldén et al. (1982a).

resulting DIAL curve from an artificial mercury cloud at a distance of about 100 m are shown in Fig. 3.37. However, the laser power and line width did not allow practical monitoring. In the on-resonance curve it is possible to see a fluorescence signal associated with the dense mercury cloud. It occurs weakly even at atmospheric pressure because the 254 nm line is the only radiative decay channel available. The occurrence of fluorescence does not induce any problems in the evaluation of mercury concentrations, as demonstrated by Edner et al. (1989). Real measurements of industrial mercury pollution became possible when narrow-band coumarin dye laser emission at 508 nm could be efficiently directly doubled using the new nonlinear crystal BBO. Figure 3.38 shows the result of a horizontal scan around the cell house of a Swedish chlorine-alkali plant (Edner et al., 1989), performed with the new Swedish
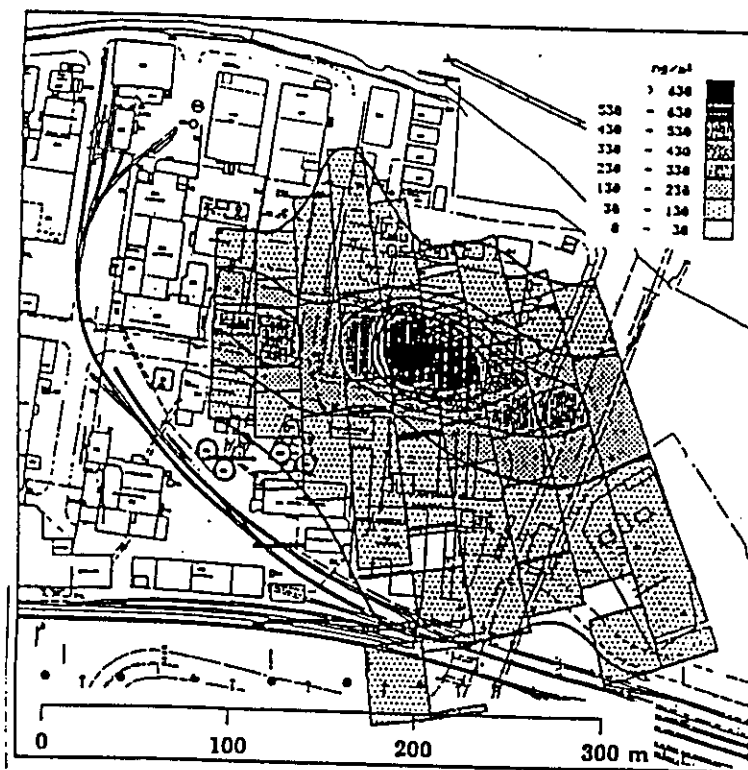
Figure 3.38. Horizontal lidar scan at a Swedish chlorine-alkali plant showing the horizontal distribution of atomic mercury. From Edner et al. (1989).

DIAL system. From data in vertical scans downwind from the cell house and available wind data, an emission of 30 g/h is obtained. Measurements at a similar Italian plant yielded similar emission values and an estimated yearly mercury emission of 500 kg (Ferrara et al., 1992). A vertical scan featuring a strong plume and a weaker one is shown in Fig. 3.39. The mercury emission from the stack of a crematorium is shown in Fig. 3.40 during the cremation process (Edner et al., 1991b). In order to alleviate environmental problems in this connection, techniques like selenium addition at the cremation or gas filtering are being tested.

Lidar measurements of mercury have been performed in Icelandic and Italian geothermal fields by the Swedish lidar group. Although no enhanced
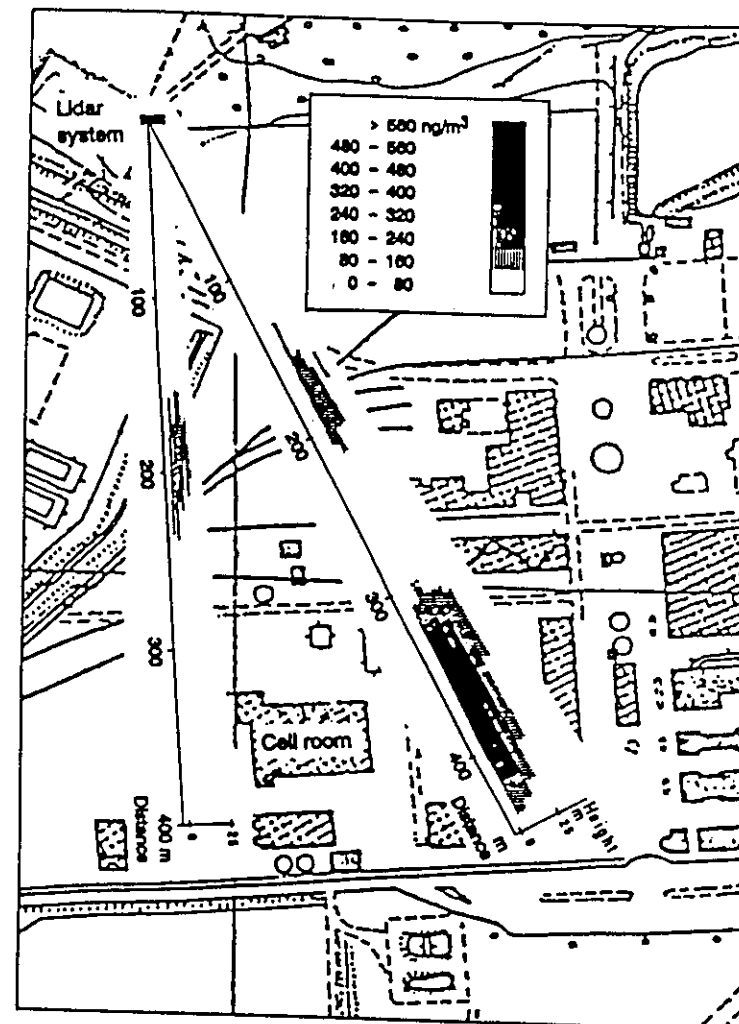

Figure 3.39. Vertical lidar scans, upwind and downwind from the cell house at the chlorine-alkali plant at Rosignano Solvay, Italy. The vertical Hg concentration plots are shown in diagrams placed along the lines of measurement. The weak plume is related to a mercury waste deposit. From Ferrara et al. (1992).
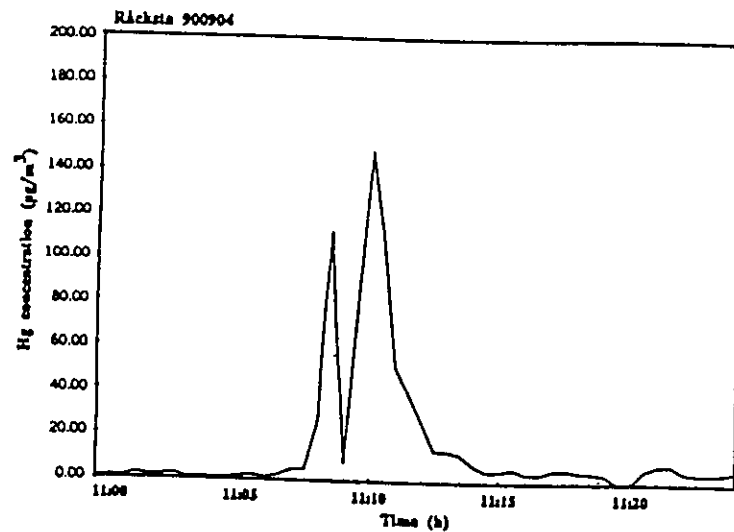
Figure 3.40. The concentration of atomic mercury in the stack effluents of a Swedish crematorium during a single cremation. The recording was taken with the Swedish mobile DIAL system, placed 200 m from the crematorium. From Edner et al. (1991b).

Figure 3.41. Photograph of the Swedish mobile DIAL system during atomic mercury measurements at the geothermal plant at Castelnuovo di Val di Cecina, Italy. From Edner et al. (1992c).

atomic mercury emissions could be detected in three Icelandic geothermal fields (Edner et al., 1991c), strongly elevated values were found in Italy (Edner et al., 1992c). A photograph of the new Swedish mobile DIAL system during measurement at a geothermal power station in Tuscany, Italy, is shown in Fig. 3.41. As can be seen in Fig. 3.42, substantial emissions are recorded. The

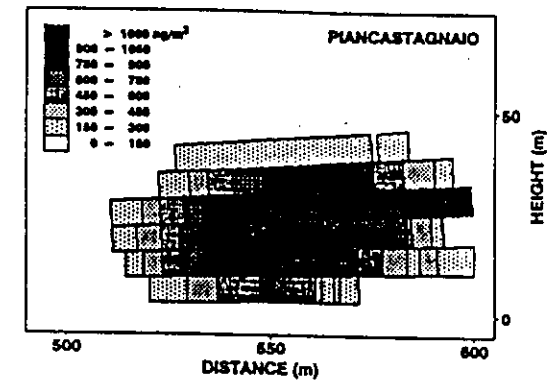Figure 3.42. Vertical mercury lidar scan through the plume from the geothermal power plant at Piancastagnaio, Italy (20 MW). From Edner et al., 1992c).
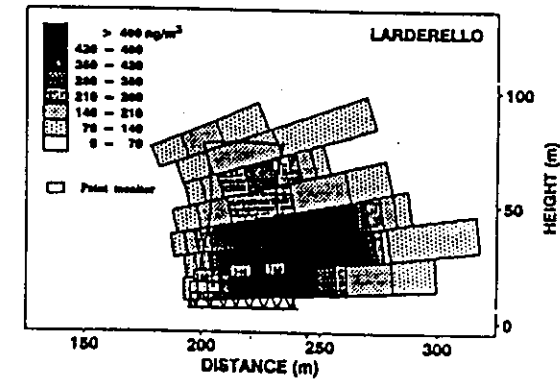

Figure 3.43. Vertical lidar scan at the geothermal power plant at Larderello, Italy. The DIAL data for atomic mercury concentration are compared with the data from three point monitors placed close to the cooling tower. From Edner et al. (1992c).

yearly total flux of mercury from the plant is estimated to be about 200 kg, combining DIAL scans with wind velocity data. Data from a vertical scan close to the cooling towers at the largest geothermal power station in Europe are shown in Fig. 3.43. In the figure data obtained using point monitors based on mercury amalgamation in gold and subsequent atomic absorption monitoring are inserted. As can be seen there is a good agreement between the two measurement techniques.

The aforementioned absence of elevated concentrations of atomic mercury in the air over geothermal fields in Iceland presents a puzzle. There can be no
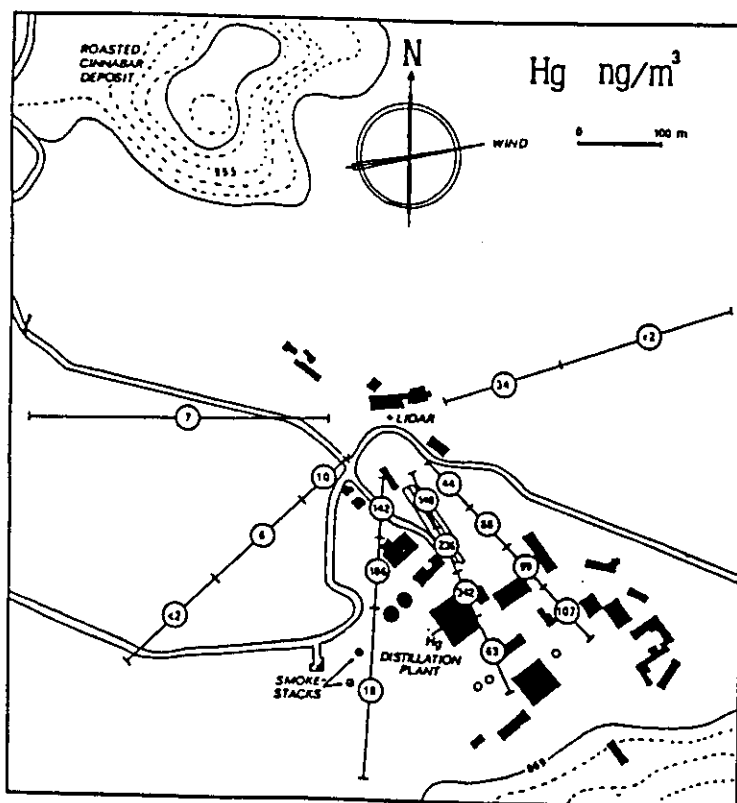

Figure 3.44. Mercury concentration data from a horizontal lidar scan at the abandoned mercury mine at Abbadia S. Salvatore, Italy. From Edner et al. (1993a).

doubt about the presence of significant amounts of mercury in well fluids in these areas. The lidar technique is sensitive only to atomic mercury. Mercury in a form other than elemental vapor would therefor: not have been revealed in our search. The occurrence of the mercury in some form other than elemental vapor seems to be the most probable explanation for the failure of the lidar search to detect significant concentrations. Mercury in Californian geothermal fields is known to be present mainly in elemental form (Robertson et al., 1977), as is the case in Italy.

In connection with mercury mining there is a substantial emission of mercury to the atmosphere. We have performed DIAL monitoring of the air over the now abandoned mercury mine at Abbadia S. Salvatore in Tuscany, Italy (Edner et al., 1993a). A horizontal map over the mining area is shown in Fig. 3.44, with mean concentrations given in circles for selected path lengths. As can be seen strongly elevated concentrations are found, particularly in connection with a distillation plant. On the other hand, the concentration quickly reaches the background value (2 ng/m³) outside the central area.

In connection with the mine there are large deposits of roasted cinnabar ore still containing about 0.2% of mercury. There is a substantial outgassing from these cinnabar banks. The DIAL technique can be used to measure the atomic mercury gradient due to the outgassing, which is particularly strong at elevated temperature. Comparisons with point monitoring distributed along a
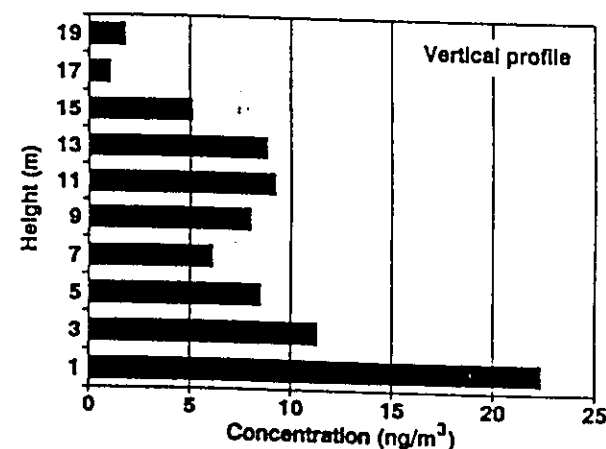

Figure 3.45. Vertical atomic mercury gradient over roasted cinnabar ore deposits at Abbadia S. Salvatore, Italy, measured with a mercury DIAL system. From Edner et al. (1993a).

vertical wire suspended from a crane showed good agreement (Ferrara et al., 1991). Data are shown in Fig. 3.45. Attempts have also been made to measure the very low mercury gradient above lake surfaces by comparing data obtained in long paths chosen at low heights above the surface (Edner and Svanberg, 1991). It has been postulated that this may account for missing mercury in the full environmental cycle of this element. In these measurements the lidar beam was directed onto large first surface mirrors mounted to provide measurement paths across a lake at 0.5 and 2.0 m above the surface. In initial measurements the concentration gradient over the lake surface was not high enough to be detected.

We conclude this section on atmospheric mercury monitoring by showing an example of a background mercury concentration measurement illustrating the sensitivity of the technique. The DIAL curve in Fig. 3.46 allows a determination of the ambient air atomic mercury concentration over the city of Lund, Sweden, which was found to be 1.5 ± 1.0 ng/m^3 Hg over a 1-km path.

As shown by the foregoing examples, DIAL monitoring of atomic mercury is a very powerful technique that can be employed not only for traditional pollution monitoring but also for studying geophysical processes.
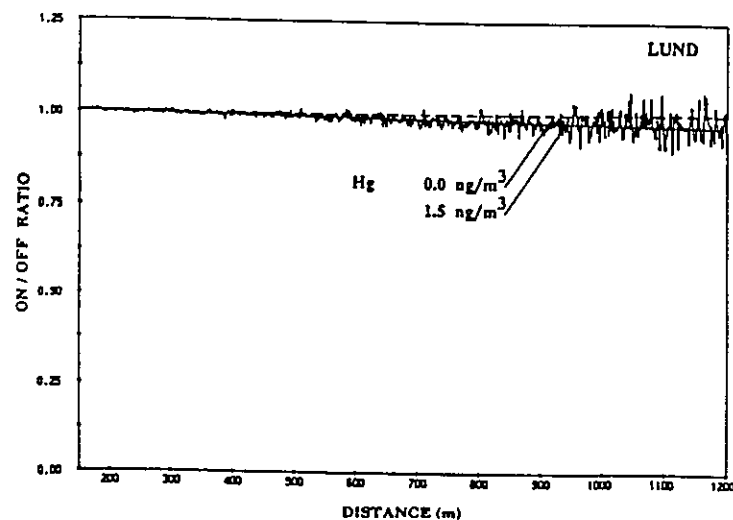

Figure 3.46. DIAL curve from a background atomic mercury concentration measurement in the city of Lund, Sweden. From Edner and Svanberg (1991).

3.8. OUTLOOK

The DIAL technique for monitoring of atmospheric pollutants is reaching a substantial level of general applicability and maturity. It provides unique possibilities for three-dimensional mapping of the atmosphere and for measuring total fluxes from industrial and urban areas. The technique is starting to be applied for routine monitoring. The largest obstacles to the widespread application of the powerful DIAL technique is system complexity. This is particularly true for the laser part. A very interesting development is the emergence of diode-pumped Nd:YAG lasers that can be used for pumping of titanium–sapphire lasers. Moderate-cost systems using this all-solid-state technology would mean a breakthrough for DIAL technology: high reliability and ease of operation could be anticipated. Very powerful and low-cost computers are already available for near-real-time data processing into understandable graphs. The increased compactness possible with the new technology will allow installation in small vehicles that can easily be moved from one measuring site to another without tedious setup procedures. The same technology will also enable construction of realistic DIAL airborne systems.

The ultimate application of the DIAL technique is global monitoring of meteorological parameters and atmospheric pollution from space. Increasing system performance, compactness, and reliability in conjunction with the planned availability of serviceable space platforms should make execution of such a scenario possible. Both NASA and ESA (the European Space Agency) are planning space lidar systems providing global wind, temperature, and pollution monitoring (see, e.g., Couch et al., 1991).

ACKNOWLEDGMENTS

REFERENCES

Aldén, M., Edner, H., and Svanberg, S. (1982a). Remote measurements of atmospheric mercury using differential absorption lidar. Opt. Lett. 7, 221–223.

Aldén, M., Edner, H., and Svanberg, S. (1982b). Laser monitoring of atmospheric NO using ultraviolet differential-absorption techniques. *Opt. Lett* 7, 543–545.

American National Standards Institute (ANSI), (1986). "American National Standards for the Safe Use of Lasers,"ANSI-Rep. Z136.1. ANSI, Washington, DC.

Ansmann, A., Riebesell, M., Wandinger, U., Weitkamp, C., Voss, E., Lahmann, W., and Michaelis, W. (1992). Combined Raman elastic-backscatter LIDAR for vertical profiling of moisture, aerosol extinction, backscatter, and LIDAR ratio. *Appl. Phys.* B55, 18–28.

Axelsson, H., Edner, H., Galle, B., Ragnarson, P., and Rudin, M. (1990). Differential absorption spectroscopy (DOAS) measurements of ozone in the 280–290 nm wavelength region. *Appl. Spectrosc.* 44, 1654–1658.

Bach, W., Pankrath, J., and Kellogg, W., Eds. (1979). *Man's Impact on Climate* Elsevier, Amsterdam.

Barbini, R., Colao, F., Palucci, A., Ribezzo, S., Hermsen, T., and Orlando, S. (1991). "Ozone Measurements from the ENEA Lidar/DIAL system," EUROTRAC Annual Report 1990, Part 7, pp. 46–51. EUROTRAC, Garmisch-Partenkirchen, Germany.

Bowman, M. R., Gibson, A. J., and Sandford, M. C. W. (1969). Atmospheric sodium measured by a tuned laser radar. *Nature (London)* 221, 456–457.

Breschi, B., Cecchi, G., Pantani, L., Raimondi, V., Tirelli, D., Valmori, G., Mazzinghi, P., and Zoppi, M. (1992). Measurement of water column temperature by Raman scattering. EARSeL (Eur. Assoc. Remote Sens. Lab.) *Adv. Remote Sens.* 1, 131–134.

Bristow, Q., and Jonasson, I. R. (1972). Vapour sensing for mineral exploration. *Can. Min. J.* 93, 39–47.

Browell, E. V. (1985). Ultraviolet DIAL measurements of O_3 Profiles in regions of spatially inhomogeneous aerosols. *Appl. Opt.* 24, 2827–2836.

Browell, E. V. (1991). Differential absorption lidar detection of ozone in the troposphere and lower stratosphere. In *Optoelectronics for Environmental Science* (S. Martellucci and A. N. Chester, Eds.), pp. 77–89. Plenum, New York.

Browell, E. V., Wilkerson, T. D., and McIlrath, T. J. (1978). Water vapor differential-absorption lidar development and evaluation. *Appl. Opt.* 18, 3474–3483.

Browell, E. V., Carter, A. F., and Wilkerson, T. D. (1981). Airborne differential absorption lidar system for water vapor investigation. *Opt. Eng.* 20, 84.

Browell, E. V., Carter, A. F., Jr., Shipley, S. T., Allen, R. J., Butler, C. F., Mayo, M. N., Siviter, J. H., and Hall, W. M. (1983). Airborne LIDAR system and measurements of ozone and aerosol profile. *Appl. Opt.* 22, 522–532.

Browell, E. V., Butler, C. F., Ismail, S., Fenn, M. A., Kooi, S. A., Carter, A. F., Tuck, A. F., Toon, O. B., Proffitt, M. H., Loewenstein, M., Schoeberl, M. R., Isaksen, I., and Braathen, G. (1990). Airborne lidar observations in the wintertime arctic stratosphere: Ozone. *Geophys. Res. Lett.* 17, 325–328.

Capelle, G. A., Franks, L. A., and Jessup, D. A. (1983). Aerial testing of a KrF laser-based fluorosensor. *Appl. Opt.* 22, 3382–3387.

Carswell, A. I. (1983). Lidar measurement of the atmosphere. *Can. J. Phys.* 61, 378–395.

Carswell, A. I., Chairman (1986). *Thirteenth International Laser Radar Conference*, NASA Conf. Publ. 2431. NASA, Toronto.

Cecchi, G., and Pantani, L. (1991). Vegetation monitoring by means of spectral resolved fluorescence lidar. *Eur. Space Agency [Spec. Publ.]* ESA SP-319, p. 687.

Celander, L., Fredriksson, K., Galle, B., and Svanberg, S. (1978). "Investigation of laser-induced fluorescence with applications to remote sensing of environmental parameters," Rep. GIPR-149. Göteborg Institute of Physics, CTH, Göteborg, Sweden.

Chanin, M. L. (1983). Rayleigh and resonance sounding of the stratosphere and mesosphere. *Springer Ser. Opt. Sci.* 39.

Chappelle, E. W., Wood, F. M., Newcomb, W. W., and McMurtrey, J. E., III (1985). Laser-induced fluorescence of green plants. 3. LIF spectral studies of five major plant types. *Appl. Opt.* 24, 74–80.

Chen, H. S. (1985). *Space Remote Sensing Systems.* Academic Press, Orlando, FL.

Collins, G. P. (1992). Making stars to see stars: DOD adaptive optics work is declassified. *Phys. Today* 45, (2), 17–21.

Collins, R. L., Bowman, K. P., and Gardner, C. S. (1992). Lidar observations of polar stratospheric clouds and stratospheric temperatures at the South Pole. *NASA Conf. Publ.* 3158, 293–295.

Couch, R. H., Rowland, C. W., Ellis, K. S., Blythe, M. P., Regan, C. R., Koch, M. R., Antill, C. W., Cox, J. W., DeLorme, J. F., Crockett, S. K., Remus, R. W., Casas, J. C., and Hunt, W. H. (1991). Lidar-in-space technology experiment: NASA's first in-space lidar system for atmospheric research. *Opt. Eng.* 30, 88–95.

Edner, H., and Svanberg, S. (1991). Differential lidar measurements of atmospheric mercury. *Water, Air, Soil Pollut.* 56 131–139.

Edner, H., Svanberg, S., Unéus, L., and Wendt, W. (1984). Gas correlation lidar. *Opt. Lett.* 9, 493–495.

Edner, H., Fredriksson, K., Sunesson, A., and Wendt, W. (1987a). Monitoring Cl_2 using a differential absorption lidar system. *Appl. Opt.* 26, 3183.

Edner, H., Fredriksson, K., Sunesson, A., Svanberg, S., Unéus, L., and Wendt, W. (1987b). Mobile remote sensing system for atmospheric monitoring. *Appl. Opt.* 26, 4330–4338.

Edner, H., Sunesson, A., and Svanberg, S. (1988). NO plume mapping using laser radar techniques. *Opt. Lett.* 12, 704–706.

Edner, H., Faris, G. W., Sunesson, A., and Svanberg, S. (1989). Atmospheric atomic mercury monitoring using differential absorption lidar techniques. *Appl. Opt.* 28, 921–930.

Edner, H., Ragnarson, P., Svanberg, S., and Wallinder, E. (1991a). "Vertical Lidar Probing of Ozone and Related Trace Species," EUROTRAC Annual Report 1990, Part 7, pp. 37–40. EUROTRAC Secretariat, Garmisch-Partenkirchen, Germany.

Edner, H., Olsson, P., and Wallinder, E. (1991b). "Measurements of Mercury with Optical Techniques at the Räcksta crematorium," Lund Rep. At. Phys. LRAP-118. Lund Institute of Technology, Lund, Sweden.

Edner, H., Faris, G. W., Sunesson, A., Svanberg, S., Bjarnason, J.Ö., Kristmansdóttir, H., and Sigurdsson, K.H. (1991c). Lidar search for atomic mercury in Icelandic geothermal fields. *J. Geophys. Res.* 94D, 2977–2985.

Edner, H., Ragnarson, P., Spännare, S., and Svanberg, S. (1992a). "A differential absorption spectroscopy (DOAS) system for urban atmospheric pollution monitoring." Lund Rep. At. Phys. LRAP-133. Lund University, Lund, Sweden, and *Appl. Opt.*, in press. 1993.

Edner, H., Svanberg S., and Wallinder, E. (1992b). Photo-oxidants: precursors and products. Evaluation of DIAL systems for tropospheric ozone. In *EUROTRAC Symposium '92*. (P. M. Borrell, P. Borrell, T. Civitas, and W. Seiler, eds.) SPB Acad. Publishing. The Hague, Netherlands.

Edner, H., Ragnarson, P., Svanberg, S., Wallinder, E., De Liso, A., Ferrara, R., and Maserti, B.E. (1992c). Differential absorption lidar mapping of atmospheric atomic mercury in Italian geothermal fields. *J. Geophys. Res.* 97D, 3779–3786.

Edner, H., Johansson, J., Svanberg, S., Wallinder, E., Bazzani, M., Breschi, B., Cecchi, G., Pantani, L., Radicati, B., Raimondi, V., Tirelli, D., and Valmori, G. (1992d). Laser-induced fluorescence monitoring of vegetation in Tuscany. EARSeL (Eur. Assoc. Remote Sens. Lab.). *Adv. Remote Sens.* 1, 119–130.

Edner, H., Johansson, J., Svanberg, S., Wallinder E., Cecchi, G., and Pantani, L. (1992e). Fluorescence lidar monitoring of the Arno River. EARSeL (Eur. Assoc. Remote Sens. Lab.). *Adv. Remote Sens.* 1, 42–45.

Edner, H., Ragnarson, P., Svanberg, S., Wallinder, E., Bargagli, R., Ferrara, R., and Maserti, B.E. (1993a). Atmospheric mercury mapping in a Cinnabar mining area. *Sci. Total Environ.* 133, 1–15.

Edner, H., Ragnarson, P., Spännare, S., and Svanberg, S. (1993b). *Appl. Opt.* 32, 327–333.

Egebäck, A.L., Fredriksson, K., and Hertz, H. M. (1984). DIAL techniques for the control of sulfur dioxide emission. *Appl. Opt.* 23, 722–729.

Englisch, W., Wieseman, W., Boscher, J., and Rother, M. (1983). Laser remote sensing measurements of atmospheric species and natural target reflectivities. *Springer Ser. Opt. Sci.* 39, 38.

Farman, J. C., Gardiner, B. G., and Shanklin, J. D. (1985). Large losses of total ozone in Antarctica reveal seasonal ClO$_x$/NO$_x$ interaction. *Nature (London)* 315, 207.

Ferrara, R., Maserti, B. E., Morelli, M., Edner, H., Ragnarson, P., Svanberg, S., and Wallinder, E. (1991). Vertical distribution of atmospheric mercury concentration over a Cinnabar deposit. In *Heavy Metals in the Environment*, (J.G. Farmer, ed.), C.E.P. Consultants, Edinburgh. pp. 247–250.

Ferrara, R., Maserti, B. E., Edner, H., Ragnarson, P., Svanberg, S., and Wallinder, E. (1992). Mercury emissions to the atmosphere from a chloralkali complex measured by the lidar technique. *Atmos. Environ.* 26A, 1253–1258.

Fioccio, G., and Smullin, L. D. (1963). Detection of scattering layers in the upper atmosphere (60–140 km) by optical radars. *Nature (London)* 199, 1275–1276.

Fredriksson, K. (1988). Differential absorption lidar for pollution mapping. In *Laser Remote Chemical Analysis* (R. M. Measures, ed.), pp. 273–331. Wiley (Interscience), New York.

Fredriksson, K., and Hertz, H. M. (1984). Evaluation of the DIAL technique for studies on NO$_2$ using a mobile lidar system. *Appl. Opt.* 23, 1403–1411.

Fredriksson, K., Lindgren, I., Svanberg, S., and Weibull, G. (1976). "Measurements of the emission from industrial smoke-stacks using laser radar techniques," Rep. GIPR-121. Göteborg Institute of Physics, CTH, Göteborg, Sweden.

Fredriksson, K., Galle, B., Linder, A., Nyström, K., and Svanberg, S. (1977). "Laser radar measurements of air pollutants at an oil-burning power station, Rep. GIPR-150. Göteborg Institute of Physics, CTH, Göteborg, Sweden.

Fredriksson, K., Galle, B., Nyström K., and Svanberg, S. (1979). Lidar system applied in atmospheric pollution monitoring. *Appl. Opt.* 18, 2998–3003.

Fredriksson, K., Galle, B., Nyström, K., and Svanberg, S. (1981). Mobile lidar system for environmental probing. *Appl. Opt.* 20, 4181–4189.

Fricke, K. H., and von Zahn, U. (1985). Mesopause temperatures derived from probing the hyperfine structure of the D$_2$ resonance line of sodium by lidar. *J. Atmos. Terr. Phys.* 47, 499–512.

Galetti, E. (1987). Detection of methane leaks with a correlation lidar. *Opt. Soc. Am., Tech. Dig. Ser.* 18.

Garnier, A., and Chanin, M.L. (1992). Description of a Doppler Rayleigh LIDAR for measuring winds in the middle atmosphere. *Appl. Phys.* B55, 35–40.

Grant, W. B. (1982). Effect of differential special reflectance of DIAL measurement using topographic targets. *Appl. Opt.* 21, 2390–2394.

Grant, W. B. (1987). Laser remote sensing techniques. In *Laser Spectroscopy and Its Applications* (L. J. Radziemski, R.W. Solarz, and J.A. Paisner, Eds.), pp. 565–621. Dekker, New York.

Grant, W. B. (1989). The mobile atmospheric pollutant mapping (MAPM) system: A coherent CO$_2$ DIAL system Proc. SPIE—*Int. Soc. Opt. Eng.* 1062, 172.

Grant, W. B., and Menzies, R. T. (1983). A survey of laser and selected optical systems for remote measurement of pollutant gas concentration. *APCA J.* 33, 187–194.

Grant, W. B., Hake, R. D., Jr., Liston, E. M., Robbins, R. C., and Proctor, E.K., Jr. (1974). Calibrated remote measurement of NO$_2$ using differential absorption backscattering technique. *Appl. Phys. Lett.* 24, 550–552.

Hansen, G., and von Zahn, U. (1990). Sudden sodium layers in polar lattitudes. *J. Atmos. Terr. Phys.* 52, 585–608.

Harms, J. (1979). Lidar return signals for coaxial and noncoaxial systems with central obstruction. *Appl. Opt.* 18, 1559–1566.

Harms, J., Lahmann, W., and Weitkamp, C. (1978). Geometrical compression of lidar return signals. *Appl. Opt.* 17, 1131–1135.

Hauchecorne, A., Chanin, M. L., Keckhut, P., and Nedeljkovic, D. (1992). LIDAR monitoring of the temperature in the middle and lower atmosphere. *Appl. Phys.* B55, 29–34.

Hawley, J. G., Fletcher, D., and Wallace, G. F. (1983). Grou ..-based ultraviolet differential absorption lidar (DIAL) system and measurements. In *Optical and Laser Remote Sensing* (D. K. Killinger and A. Mooradian, Ed.), pp. 128–137. Springer-Verlag, Heidelberg.

Hercules, D. H., Ed. (1966). *Fluorescence and Phosphorescence Analysis.* Wiley (Interscience), New York.

Hinkley, E. D. Ed. (1976). *Laser Monitoring of the Atmosphere,* Top. Appl. Phys. Vol. 14 Springer-Verlag, Heidelberg.

Hirschfeld, T., Schildkraut, E. R., Tannenbaum, H., and Tannenbaum, D. (1973). Remote spectroscopic analysis of ppm-level air pollutants by Raman spectroscopy. *Appl. Phys. Lett.* 22, 38.

Hoge, F. E. (1988). Ocean and terrestrial lidar measurements. In *Laser Remote Chemical Analysis* (R. M. Measures, Ed.), pp. 409–503. Wiley (Interscience), New York.

Hoge, F. E., Swift, R. N., and Frederick, E. B. (1980). Water depth measurement using an airbone pulsed neon laser system. *Appl. Opt.* 19, 871–883.

Hoge, F. E., Swift, R. N., and Yungel, J. K. (1983). Feasibility of airborne detection of laser-induced fluorescence of green terrestrial plants. *Appl. Opt.* 22, 2991–3000.

Hoge, F. E., Swift, R. N., and Yungel, J. K. (1986). Active-passive airborne ocean color measurement. 2: Applications. *Appl. Opt.* 25, 48–57.

Huffaker, R. M., Lawrence, T. R., Post, M. J., Priestley, J. T., Hall, F. F., Jr., Richter, R. A., and Keeler, R. J. (1984). Feasibility studies for a global wind measuring satellite system. (Windsat): Analysis of simulated performance. *Appl. Opt.* 23, 2523–2536.

Jepsen, A. F. (1973). Measurements of mercury vapor in the atmosphere. *Adv. Chem. Ser.* 123, 80–94.

Jeys, T. H., Brailove, A. A., and Mooradian, A. (1989). Sum frequency generation of sodium resonance radiation. *Appl. Opt.* 28, 2588–2591.

Jolliffe, B. W., Michelson, E., Swann, N. R. W., and Woods, P. T. (1987). A differential absorption Lidar system for measurements of tropospheric NO, NO$_2$, SO$_2$, and O$_3$. *Opt. Soc. Am., Tech. Dig. Ser.* 180.

Kane, T. J., Mui, P., and Gardner, C. S. (1992). Evidence for substantial seasonal variations in the structure of the mesospheric iron layer. *Geophys. Res. Lett.* 19, 405–408.

Kerker, M. (1969). *The Scattering of Light,* Academic Press, New York.

Killinger, D. A. (1992). USF HITRAN-PC. University of South Florida, Tampa.

Killinger, D. A., and Menyuk, N. (1981). Effects of turbulence-induced correlation on laser remote sensing errors. *Appl. Phys. Lett.* 38, 968–970.

Killinger, D. A., and Mooradian, A., Eds. (1983). *Optical and Laser Remote Sensing,* Springer Ser. Opt. Sci. Vol. 39. Springer-Verlag, Heidelberg.

Killinger, D. A., Menyuk, N., and DeFoe, W. E. (1980). Remote sensing of CO$_2$ using frequency-doubled CO$_2$ laser radiation. *Appl. Phys. Lett.* 36, 402–405.

Kim, H. H. (1977). Airborne bathymetric charting using pulsed blue-green lasers. *Appl. Opt.* 16, 46–56.

Klett, J. D. (1981). Stable analytical inversion for processing lidar returns. *Appl. Opt.* 20, 211–220.

Klett, J. D. (1986). Extinction boundary value algorithms for lidar inversion. *Appl. Opt.* 25, 2462–2464.

Kobayashi, T. (1987). Techniques for laser remote sensing of the environment. *Remote Sens. Rev.* 3, 1–56.

Kölsch, H. J., Rairoux, P., Wolf, J. P., and Wöste, L. (1989). Simultaneous NO and NO$_3$ DIAL measurements using BBO crystal. *Appl. Opt.* 28, 2052–2056.

Korb, C. L. and Weng, C. Y. (1983). Differential absorption Lidar technique for measurement of the atmospheric pressure profile. *Appl. Opt.* 22, 3759–3770.

Korb, C. L., Gentry, B. M., and Weng, C. Y. (1992). The edge technique: Theory and application to the lidar measurement of atmospheric winds. *Appl. Opt.* 31, 4202–4213.

Lakowicz, J. R. (1983). *Principles of Fluorescence Spectroscopy,* Plenum, New York.

Lee, H. S., and Zwick, H. H. (1985). Gas filter correlation instrument for the remote sensing of gas leaks. *Rev. Sci. Instrum.* 56, 1812.

Leonard, D. A. (1967). Observation of Raman scattering from the atmosphere using a pulsed nitrogen ultraviolet laser. *Nature (London)* 216, 142.

Leonard, D. A., Caputo, B., and Hoge, F. E. (1979). Remote sensing of subsurface water temperature by Raman scattering. *Appl. Opt.* 18, 1732–1745.

Lichtenthaler, H. K., and Rinderle, U. (1988). The role of chlorophyll fluorescence in the detection of stress conditions is plants. *CRC Crit. Rev. Anal. Chem.* 19, Suppl. 1, S29–S88.

Lindqvist, O., Ed. (1991). *Mercury as on Environmental Pollutant, Water, Air, Soil Pollut.,* Vol. 56, Reidel, Dordrecht, The Netherlands.

Mason, B. J. (1989). The greenhouse effect. *Contemp. Phys.* 30, 417–432.

McCarthy, J. H., Jr. (1972). Mercury vapor and other volatile components in the air as guides to ore deposits. *J. Geochem. Explor.* 1, 143–162.

McCormick, M. P., Chairman (1982a). *Eleventh International Laser Radar Conference,* NASA Conf. Publ. 2228, Ast. Pap. University of Wisconsin–Madison.

McCormick, M. P. (1982b). Lidar measurements of Mt. St. Helens effluents. *Opt. Eng.* 21, 340–342.

McCormick, M. P., Ed. (1992). *Sixteenth International Laser Radar Conference,* NADA Conf. Publ. 3158. Massachusetts Institute of Technology, Cambridge.

McCormick, M. P., Swisser, T. J., Fuller, W. H., Hunt, W. H., and Osborn, M. T. (1984). Airborne and groundbased lidar measurements of the El Chichon stratospheric aerosol from 90°N to 56°S. *Geofis. Int.* 23–2, 187.

Measures, R. M. (1984). *Laser Remote Sensing: Fundamentals and Applications,* Wiley, New York.

Measures, R. M., Ed. (1988). *Laser Remote Chemical Analysis*. Wiley (Interscience), New York.

Megie, G., Ed. (1984). *Twelfth International Laser Radar Conference*, Abst. Pap. Service d' Aern., Aix-en-Provence, France.

Megie, G., Ancellet, G., and Pelon, J. (1985). Lidar measurements of ozone vertical profiles. *Appl. Opt.* 24, 3454–3463.

Menyuk, N., Killinger, D. K., and DeFeo, W. E. (1980). Remote sensing of NO using a differential absorption lidar. *Appl. Opt.* 19, 3282–3286.

Menyuk, N., Killinger, D. K., and DeFeo, W. E. (1982). Laser remote sensing of hydrazine, MMH, and UDMH using a differential-absorption CO_2 lidar. *Appl. Opt.* 21, 2275–2286.

Menzies, R. T. (1976). Laser heterodyne detection techniques. In *Laser Monitoring of the Atmosphere*. (R. T. Hinkely, Ed.), pp. 297–353. Springer-Verlag, Heidelberg.

Menzies, R. T. (1991). Laser atmospheric wind Velocity measurement. In *Optoelectronics for Environmental Science* (S. Martellucci and A. N. Chester, Eds.), pp. 103–116. Plenum, New York.

Menzies R. T., and Seals, R. K., Jr. (1977). Ozone monitoring with an infrared heterodyne radiometer. *Science* 197, 1275–1277.

Milton, M. J. T., Bradsell, R. H., Jolliffe, B. W. Swann, N. R. W. and Woods, P.T. (1988). The design and development of a near-infrared DIAL system for the detection of hydrocarbons. *Int. Laser Radar Conf., 14th*, pp. 370–373.

Milton, M. J. T., Woods, P. T., Jolliffe, B. W., Swann, N. R. W., and McIlveen, T. J. (1992). Measurements of toluene and other aromatic hydrocarbons by differential-absorption LIDAR in the near-ultraviolet. *Appl. Phys.* B55, 41–45.

Mitra, S. (1986). *Mercury in the Ecosystem*, Technomic, Basel.

Molina, L. T., and Molina, M. J. (1986). Absolute absorption cross sections of ozone in the 185- to 350-nm region. *J. Geophys. Res.* 91D, 14501–14508.

Ngriau, J. O., Ed. (1979). *The Biogeochemistry of Mercury in the Environment.* Elsevier/North-Holland, Amsterdam.

Nickolov, Zh., and Svanberg, S. (1986)."On the Possibilities of NO/NO_2 Simultaneous Detection by DIAL," Lund Rep. At. Phys. LRAP-71, LTH, Lund Institute of Technology, Lund, Sweden.

O'Neill, R. A., Buja-Bijunas, L., and Rayner, D. M. (1980). Field performance of a laser fluorosensor for the detection of oil spills. *Appl. Opt.* 19, 863–870.

Osborn, M. T., Winker, D. M., Woods, D. C., and DeCoursey, R. J. (1992). Lidar observations of the Pinatubo volcanic cloud over Hampton, Virgina. *Nasa Conf. Publ.* 3158, 91–94.

Reuter, R. (1991). Hydrographic applications of airborne laser spectroscopy. In *Optoelectronics for Environmental Science* (S. Martellucci and A.N. Chester, Eds.), pp. 149–160. Plenum, New York.

Revelle, R. (1982). Carbon dioxide and world climate. *Sci. Am.* 247, 33–41.

Robertson, D. E., Crecelius, E. A., Fruchter, J. S., and Ludwick, J. D. (1977). Mercury emissions from geothermal power plants. *Science* 196, 1094–1097.

Rothe, K. W., Brinkmann, U., and Walther, H. (1974a). Applications of tunable dye lasers to air pollution detection: Measurements of atmospheric NO_2 concentrations by differential absorption. *Appl. Phys.* 3, 115.

Rothe, K. W., Brinkmann, U., and Walther, H. (1974b). Remote sensing of NO_2 emission from a chemical factory by the differential absorption technique. *Appl. Phys.* 4, 181–184.

Rothman, L. S., Garmache, R. R., Goldman, A., Brown, L. R., Toth, R. A., Pickett, H. M., Poynter, R. L., Flaud, J. M., Camy-Peyret, C., Barbe, A., Husson, N., Rinsland, C. P., and Smith, M. A. H. (1987). The HITRAN Database: 1986 edition. *Appl. Opt.* 26, 4058–4097.

Scinfeld, J. H. (1986). *Atmospheric Chemistry and Physics of Air Pollution,* Wiley, New York.

Shimizu, H., Sasano, Y., Nakane, H., Sugimoto, N., Matsui, I., and Takeuchi, N. (1985). Large scale laser radar for measuring aerosol distribution over a wide aera. *Appl. Opt.* 24, 617–626.

Shotland, R. M. (1966). Some observations of the vertical profile of water vapour by a laser optical radar. *Proc. Symp. Remote Sens. Environ., 4th,* University of Michigan, Ann Arbor, *1966,* pp. 273–283.

Shumate, M. S., Lundqvist, S., Persson, U., and Eng, S. T. (1982). Differential reflectance of natural and man-made materials at CO_2 laser wavelengths *Appl. Opt.* 21, 2386–2389.

Siegman, A. E. (1986). *Lasers.* University Science Books, Mill Valley, CA.

Slemr, F., Seiler, W., and Schuster, G. (1981). Latitudinal distribution of mercury over the Atlantic Ocean, *J. Geophys. Res.* 86D, 1159–1166.

Sliney, D., and Wolbarsht, M. (1980). *Safety with Lasers and Other Optical Sources: A Comprehensive Handbook.* Plenum, New York.

Staer, W., Lahmann, W., Weitkamp, C., and Michaelis, W. (1984). Differential absorption lidar system for NO_2 and SO_2 monitoring. *Int. Laser Radar Conf., 12th,* pp. 281–284.

Stefanutti, L., Chairman (1988). *Fourteenth International Laser Radar Conference* Conf. Abstr. CNR-IROE/ILRC-CA, Innichen–San Candido, Italy.

Stefanutti, L., Castagnoli, F., Del Guasta, M., Morandi, M., Sacco, V. M., Zuccagnoli, L., Godin, S., Megie, G., and Porteneuve, J. (1992a). The Antarctic Ozone LIDAR system. *Appl. Phys.* B55, 3–12.

Stefanutti, L., Castagnoli, F., Del Guasta, M., Morandi, M., Sacco, V. M., Zuccagnoli., L., Kolenda, J., Kneipp, H., Rairoux, P., Stein, B., Weidauer, D., and Wolf, J. P. (1992b). A four-wavelength depolarization backscattering LIDAR for polar stratospheric cloud monitoring. *Appl. Phys.* B55, 13–17.

Stolarski, R. S. (1988). The Antarctic ozone hole. *Sci. Am.* 258 (1), 20–26

Svanberg, S. (1978). Fundamentals of atmospheric spectroscopy. In *Surveillance of Environmental Pollution and Resources by Electromagnetic Waves* (T. Lund, Ed.), pp. 37–66. Reidel, Dordrecht, The Netherlands.

Svanberg, S. (1980). Lasers as probes for air and sea. *Contemp. Phys.* 21, 541–576.

Svanberg, S. (1985). Laser technology in atmospheric pollution monitoring. In *Applied Physics: Laser and Plasma Technology* (B. C. Tan, Ed.), pp. 528–548. World Science, Singapore.

Svanberg, S. (1990). Laser fluorescence spectroscopy in environmental monitoring. In *Optoelectronics for Environmental Science* (S. Martellucci and A.N. Chester, Eds.), pp. 15–27. Plenum, New York.

Svanberg, S. (1991). Environmental monitoring using optical techniques. In *Applied Laser Spectroscopy* (W. Demtröder and M. Inguscio, Eds.), pp. 417–434. Plenum, New York.

Svanberg, S. (1992). *Atomic and Molecular Spectroscopy: Basic Concepts and Practical Applications*, 2nd ed., Springer Ser. At. Plasmas, Vol. 6. Springer-Verlag, Heidelberg.

Svelto, O. (1989). *Principles of Lasers*, 3rd ed. Plenum, New York.

Thompson, B. A., Harteck, P., and Reeves, R. R. (1963). *J. Geophys. Res.* 68D, 6431.

Thompson, L. A., and Gardner, C. S. (1987). Laser guidestar experiment at Maona Kea Observatory for adaptive imaging in astronomy. *Nature (London)* 328, 229–231.

Trush, B. A. (1988). The chemistry of the stratosphere. *Rep. Prog. Phys.* 51, 1341–1371.

Uchino, O., Maeda, M., Yamamura, H., and Hirono, M. (1983). Observation of stratospheric vertical ozone distribution by a XeCl lidar. *Opt. Lett.* 8, 347–351.

Udenfriend, S. (1962) *Fluorescence Assay in Biology and Medicine*, Vol. 1. Academic Press, New York.

Udenfriend, S. (1969). *Fluorescence Assay in Biology and Medicine*. Vol. 2. Acadamic Press, New York.

van de Hulst, H. C. (1957). *Light Scattering by Small Particles*. Wiley, New York.

Varekamp, J. C., and Buseck, P. R. (1981). Mercury emissions from Mount St Helens during September 1980. *Nature (London)* 293, 555–556.

Varekamp, J. C. and Buseck, P. R. (1983). Hg anomalies in soils: A geochemical exploration method for geothermal areas. *Geothermics* 12, 29–47.

Ward, T. V., and Zwick, H. H. (1975). Gas cell correlation spectrometer: GASPEC. *Appl. Opt.* 14, 2896–2904.

Wayne, R. P. (1985). *Chemistry of Atmospheres*. Oxford Univ. Press (Clarendon), Oxford.

Wehry, E. L., Ed. (1976). *Modern Fluorescence Spectroscopy*, Vols. 1 and 2. Plenum, New York.

Weitkamp, C. (1981). The distribution of hydrogen chloride in the plume of incineration ships: Development of new measurement systems. In *Wastes in the Ocean*, Vol. 3. Wiley, New York.

Werner, J., Rothe, K. W., and Walther, H. (1983). Monitoring of the stratospheric ozone layer by laser radar. *Appl. Phys.* B32, 113–118.

Wolf, J. P., Kölsch, H. J., Rairoux, P. and Wöste, L. (1990). Remote detection of atmospheric pollutants using differential absorption Lidar techniques. In *Applied*

Laser Spectroscopy (W. Demtröder and M. Inguscio, Eds.), pp. 435–467. Plenum, New York.

Zanzottera, E. (1990). Differential absorption Lidar techniques in the determination of trace pollutants and physical parameters of the atmosphere. *CRC Crit. Rev. Anal. Chem.* 21, 279–319.

Zuev, V. E., Chairman (1990). *Fifteenth International Laser Radar Conference*, Abstr. Pap., Parts I and II. Institute of Atmospheric Optics Publication, Tomsk, Russia.

Fluorescence Lidar Monitoring of Vegetation Status *

S. Svanberg

Department of Physics, Lund Institute of Technology, P.O. Box 118, S-221 00 Lund, Sweden

Abstract

Remote laser-induced fluorescence monitoring can complement passive reflectance measurements on vegetation. Vegetation classification and status assessment is normally performed by air- or spaceborne multi-spectral scanners. An increased research activity in the field of vegetation monitoring is motivated by the abundant stressed forests of Europe. We have used a mobile lidar system for remote studies of laser-induced fluorescence in vegetation. Point monitoring of fluorescence spectra is performed, but also multi-spectral imaging using a newly designed measurement system. Swedish experience in several field tests being part of the European LASFLEUR project is reported. Collaboration with expertise in plant physiology is stressed.

1. Introduction

There is an increasing need for powerful monitoring techniques to assess the status of the environment, regarding the atmosphere, the hydrosphere as well as the ground and its vegetation. Air- and spaceborne optical sensors are frequently used for global monitoring of the environment (see, e.g. [1]). Laser remote-sensing techniques, in particular differential-absorption and fluorescence lidars, provide means for monitoring the atmosphere and the status of vegetation. Mobile and fixed lidar systems are being used for local and regional mapping of atmospheric pollutants. A recent review of this field can be found in [2].

Fluorescence lidar studies of the hydrosphere and of terrestrial vegetation is another aspect of active remote sensing. This field has been covered by extensive reviews [3–5]. The purpose of the present paper is to provide an overview of research performed at the Lund Institute of Technology in the field on vegetation laser-induced fluorescence, updating an earlier review [6] on our work, that was initiated in 1978 [7]. Remote fluorescence point monitoring and multi-colour imaging are described providing information on green plants and trees. Several field tests with the fluorescence lidar technique have been made within the framework of the European LASFLEUR project. The goal of this project is to provide a new and hopefully more specific tool for assessing vegetation damage and forest decline, thus forming a complement to satellite vegetation monitoring [8]. By studying fluorescence the functioning of the photosynthetic apparatus can be much more directly assessed than in absorption characteristics. Fluorescence signals from vegetation originate from chlorophyll (marked peaks at 690 nm and 735 nm) as well as from other leaf constituents, giving rise to signals in the blue-green spectral region. By performing fluorescence diagnostics work together with plant physiol-

ogists a deeper understanding of the manifestations of environmental stress in plants is sought.

The relation between fluorescence signatures and plant status has been discussed, e.g. in [9, 10]. Fluorescence techniques are also useful for water pollution monitoring and recent results from our group in collaboration with Italian researchers are presented in [11, 12]. It should also be noted that experimental techniques and evaluation methods in the field of vegetation and hydrospheric fluorescence monitoring have very much in common with the methodology used in medical fluorescence diagnostics of diseased tissue [13].

An artist's conception on the study of vegetation fluorescence is shown in Fig. 1 [14]. Different experimental arrangements for studying laser-induced fluorescence in the laboratory and remotely are described in the next sections. Thus, in Section 2 a convenient point monitoring arrangement is shown and measurement examples are given. In particular, the choice of excitation wavelength is discussed. Then, remote point monitoring of fluorescence is described in Section 3 with examples from field work. The extension from point monitoring to multi-spectral imaging is taken in Section 4. A final discussion also covers a proposed European airborne system for vegetation monitoring.

2. Laboratory and field point monitoring

2.1. Point-monitoring set-up

Laboratory or field measurements on controlled plants are very important for understanding the relation between the observed signals and the plant physiological status. A fibre-optic fluorosensor, originally developed for medical tissue diagnostics, was found to be a very useful instrument for this type of work. The system can be used in the laboratory but can also be brought out into the field on board a van, with electric power supply from a small motor generator and with a 10 m long optical fibre to be brought in contact
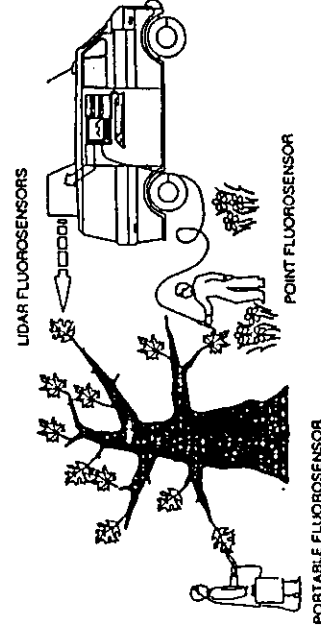

Fig. 1. Artist's conception of point and remote laser-induced fluorescence measurements on vegetation (from [14]).

Fig. 2. Fibre-based fluorosensor for point monitoring of vegetation fluorescence (from [15]).

with the leaf or needle to be studied. A lay out of the system is shown in Fig. 2 [15]. As an excitation source a pulsed nitrogen laser ($\lambda = 337$ nm) is used, either directly or after frequency conversion in a dye laser unit, pumped by a nitrogen laser. The radiation is focused into a 600 μm fibre, the tip of which is put in contact with the object to be studied. Laser-induced fluorescence is collected by the same fibre and is brought back to the entrance slit of a spectrometer after passing a dichroic mirror, reflecting the laser light by transmitting the red-shifted fluorescence light. The spectrometer is equipped with a CCD detector, proceeded by an image intensifier. The intensifier can be gated electronically only to accept light during a time window, normally set to 100 ns. In this way background light can be efficiently eliminated. Following each laser shot a full spectrum covering 300–800 nm is captured, displayed and stored. Averaging of multiple shots can be performed.

2.2. Examples of spectra

As a first example, spectra from *Picea Abies*, growing at the Italian CNR test site Camporgiano are shown in Fig. 3 [14]. Three excitation wavelengths were used: 337, 405 and 470 nm. Strong chlorophyll fluorescence with peaks at 690 and 735 nm can be seen for the longer excitation wavelengths, whereas such fluorescence is absent for 337 nm excitation. For UV excitation the match to the chlorophyll absorption band is poor while pigments emitting in the blue-green region are optimally excited. Actually, the penetration into the needle is poor and most of the excitation light is absorbed in the surface wax layer. This fibre-based fluorosensor was used in a controlled Swedish study of the influence of ozone exposure on fluorescence properties of spruce and pine [16].

A further example is shown in Fig. 4, exhibiting fluorescence spectra for maize [17]. Here, a separate excitation source yielding frequency-tripled Nd:YAG radiation at 355 nm and Raman-shifted components at 320, 397, and 450 nm was employed. (Raman medium: deuterium gas). It can be seen that chlorophyll is efficiently excited for the two longer wavelengths and that is appears very weakly for the shorter wavelength. 397 nm is a particularly useful excita-

tion wavelength, since it allows eyesafe outdoor laser operation. The eye exposure limit becomes 10000 times less stringent for wavelengths below 400 nm; an important observation for airborne fluorosensor operation.

3. Remote monitoring of fluorescence spectra

3.1. *Mobile fluorescence lidar system*

We are employing a mobile lidar system for remote monitoring of laser-induced fluorescence. An atmosphere lidar system, described in [18], is modified for fluorescence work. A scenario for field measurements of vegetation fluorescence is shown in Fig. 5 [19]. A schematic diagram of the fluorosensor equipment is shown in Fig. 6 [19, 20]. A pulsed

Fig. 3. Point monitoring of fluorescence spectra of *Picea Abies*, excited at different laser wavelengths (from [14]).

FLUORESCENCE INT.

PICEA ABIES

470 nm exc.

WAVELENGTH (nm)

FLUORESCENCE INT.

405 nm exc.

WAVELENGTH (nm)

FLUORESCENCE INT.

337 nm exc.

WAVELENGTH (nm)

Fig. 6. Set-up for remote recordings of fluorescence spectra and multi-colour fluorescence images (from [19, 20]).
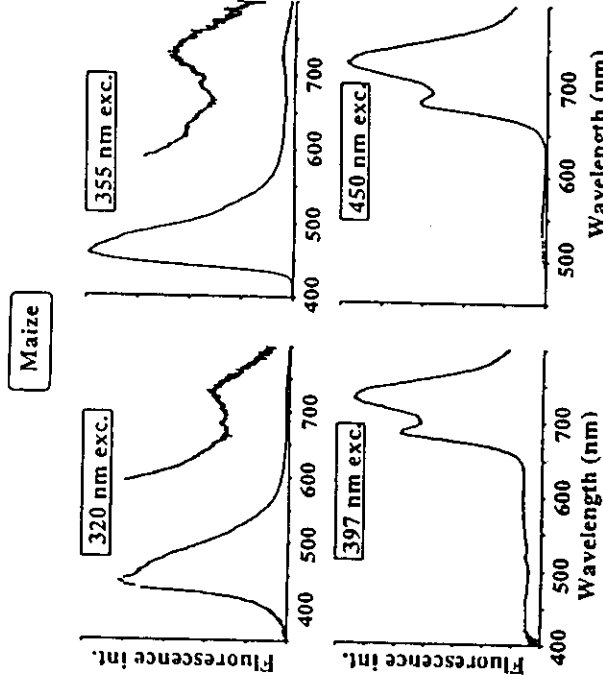

Fig. 4. Point monitoring of fluorescence spectra of maize for four different excitation wavelengths (from [17]).

Nd : YAG laser is used as the transmitter of the system. The fundamental output is frequency tripled to 355 nm and is subsequently Raman shifted in high-pressure deuterium gas to achieve 397 nm as the first Stokes component. About 30 mJ of pulse energy at 20 Hz was obtained. The outgoing beam is directed coaxially with a vertically mounted 40 cm diameter telescope and is transmitted towards the target via a $40 \times 70\,\text{cm}^2$ large flat mirror, which is under computer control. The mirror is mounted in a retractable transmission/receiving dome, with a large quartz window for weather protection. Laser-induced fluorescence in the selected target is received by the telescope and is for spectral recordings focussed into a fibre for guidance to the entrance slit of an optical multi-channel system (lower part of the figure) of a construction similar as that described in Section 2.1. In our latest version seven fibres in a circular arrangement are used. At their lateral ends they are placed in a line to match the entrance slit of the spectrometer. The gate of the image intensifier was normally set between 20 and 100 ns for gating out background light. General considerations concerning the construction of day-light fluoresensors are presented in [21]. It is now possible to capture the fluorescence spectrum remotely for a target point to which the laser beam is steered. A photograph of the system during a field campaign is shown in Fig. 7 [17].

3.2. *Examples of remotely recorded fluorescence spectra*

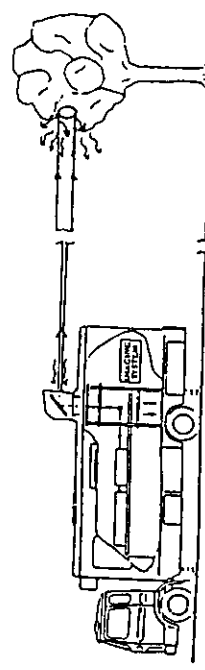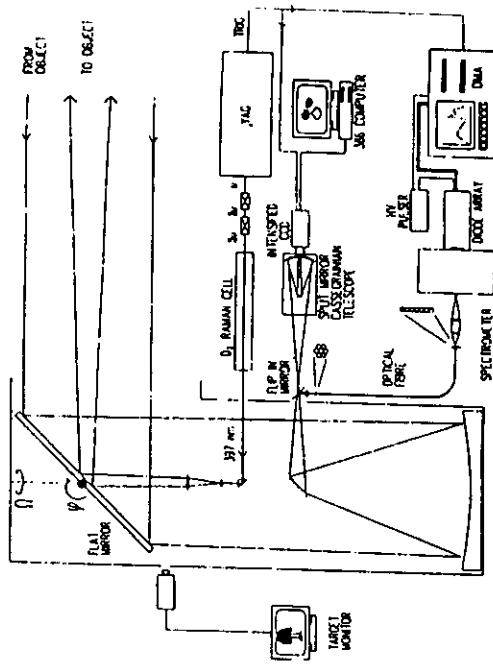As first examples we show in Fig. 8 remotely recorded spectra [17] for three different species as recorded using

397 nm excitation during a field-test at DLR, Oberpfaffenhofen as illustrated in Fig. 7. The system to target distance was 30 meters and the laser spot diameter at the target was 15 cm. As can be seen, the blue-green fluorescence is relatively more prominent for spruce in comparison with maize and maple. Also the ratio between the two red peak intensities differs between spruce and the two other species.

The daily cycle of a spruce tree is shown in Fig. 9 [17], where the red/red and the red/blue ratios are plotted as a function of time. The intensity of the light, useful for photosynthesis (PAR), is also given during the same time period.

Remote spectra of beech (*Fagus Sylvatica*), excited at 355 nm, are shown in Fig. 10 [14]. The spectra were recorded at Pian di Novello, Italy. The system/target distance was 60 m and 500 laser shots were averaged. The intensity ratio $I\,(735\,\text{nm})/I\,(690\,\text{nm})$ for a green leaf is found to be substantially higher than for a yellow leaf. The reason is that the contents of chlorophyll is higher in the green leaf, and self-absorption of the radiation at the 690 nm peak makes the above mentioned ratio become higher for green leaves [9]. The blue-green fluorescence shows some structure. This fluorescence, observed already in 1978 [7], has been subject to much interest recently, e.g. in terms of identification of the chromophores responsible for the emission observed [22].
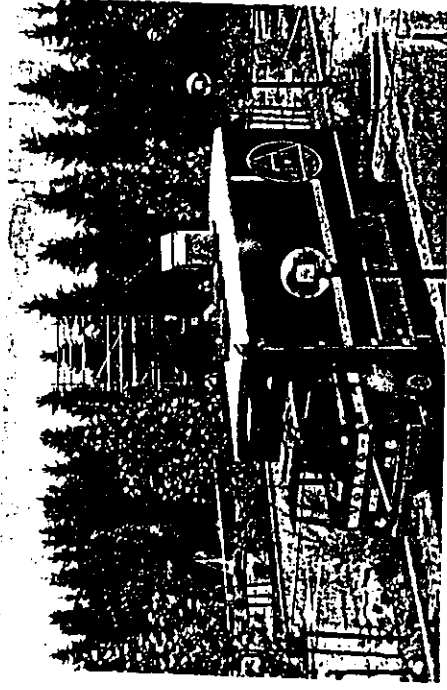

Fig. 7. Photograph of the Swedish mobile fluorescence lidar system during a field campaign at DLR, Oberpfaffenhofen (from [17]).

Fig. 5. Remote fluorescence monitoring of vegetation (from [19]).
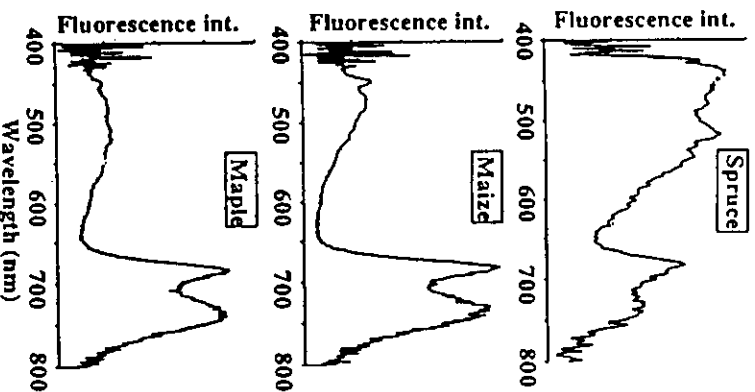
Fig. 8. Remote laser-induced fluorescence spectra of spruce, maize and maple obtained at 30 m distance using 397 nm excitation (from [17]).

The performance of the system is further illustrated by the spectra shown in Fig. 11, recorded during a field campaign at INRA, Avignon, France [20]. In these recordings the optimized seven-fibre pack was used for transferring the radiation to the spectrometer. Spectra averaged for 100 shots are shown for poplar, cypress and plane-tree at 64 m, 125 m and 210 m distance, respectively. A single-shot record-
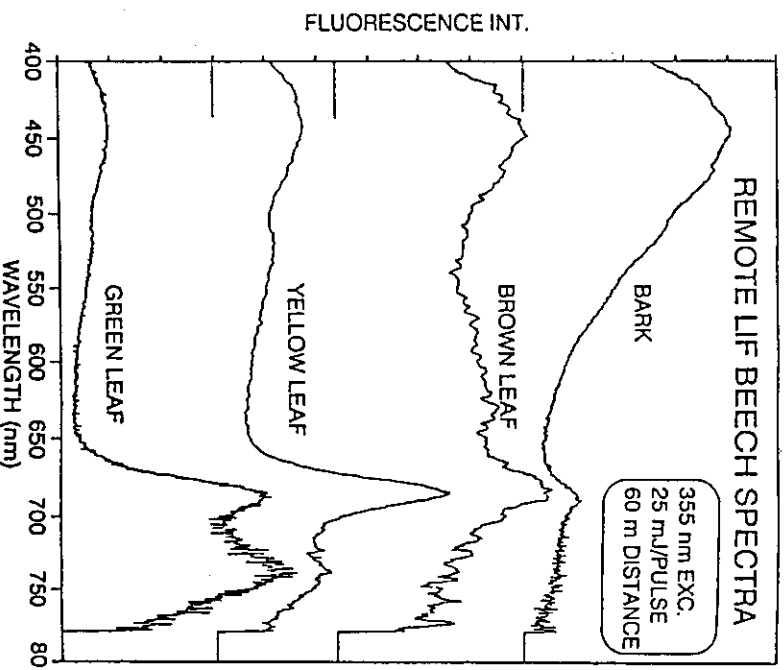
Fig. 10. Remote fluorescence spectra of beech (*Fagus Sylvatica*) at Pian di Novello (from [14]).

ing at 125 m distance is also included. Single-shot measurement capability is important especially for an airborne system moving at high speed, when averaging over several shots may not be possible.

Daily cycle recordings for maize are shown in Fig. 12 for a measuring distance of 40 m [20]. Single-shot monitoring is shown to yield basically the same results as averaged data. This demonstrates that our system is approaching the performance required for effective airborne operation.

4. Remote multi-colour fluorescence imaging

4.1. Multi-colour imaging set-up

So far we have only discussed the acquisition of fluorescence spectra from the target, which is illuminated by a laser beam
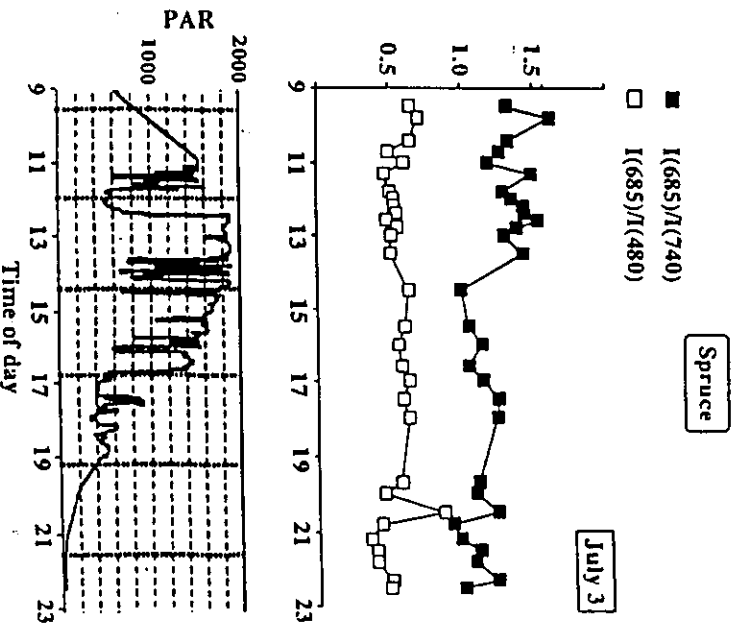

REMOTE LIF BEECH SPECTRA

355 nm EXC.
25 mJ/PULSE
60 m DISTANCE

GREEN LEAF
YELLOW LEAF
BROWN LEAF
BARK

FLUORESCENCE INT.

WAVELENGTH (nm)

Fig. 9. Daily cycle variations of the fluorescence ratio *I* (685 nm)/*I* (735 nm) and *I* (685 nm)/*I* (480 nm) for a spruce tree. PAR (illumination) values are also shown for comparison (from [17]).
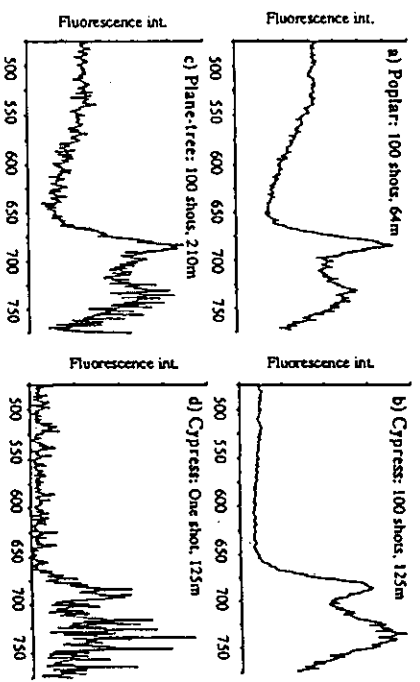
Fig. 11. Remote fluorescence spectra for poplar, cypress and plane-tree. 100 shots are averaged in (a)-(c), for distances 64 m, 125 m, and 210 m, respectively. A single-shot recording at 125 m distance is shown in (d) (from [20]).
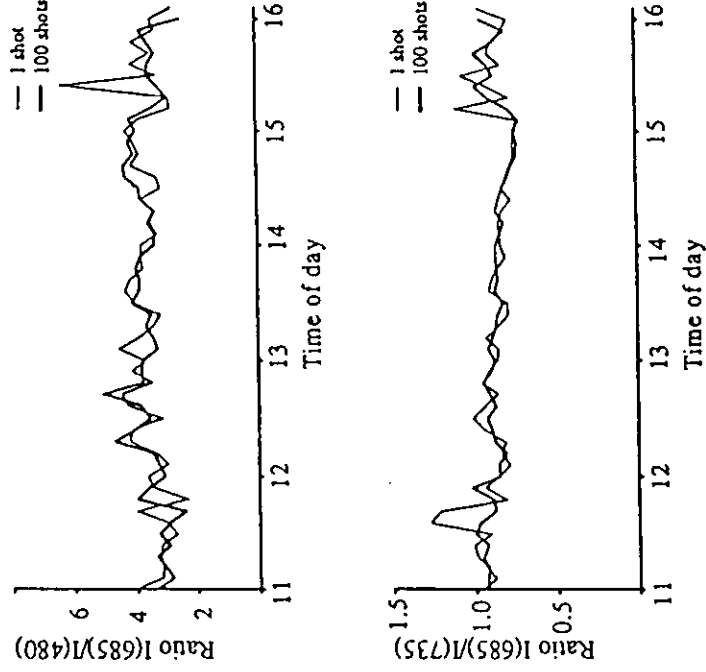
a) Poplar: 100 shots, 64m
b) Cypress: 100 shots, 125m
c) Plane-tree: 100 shots, 210m
d) Cypress: One shot, 125m

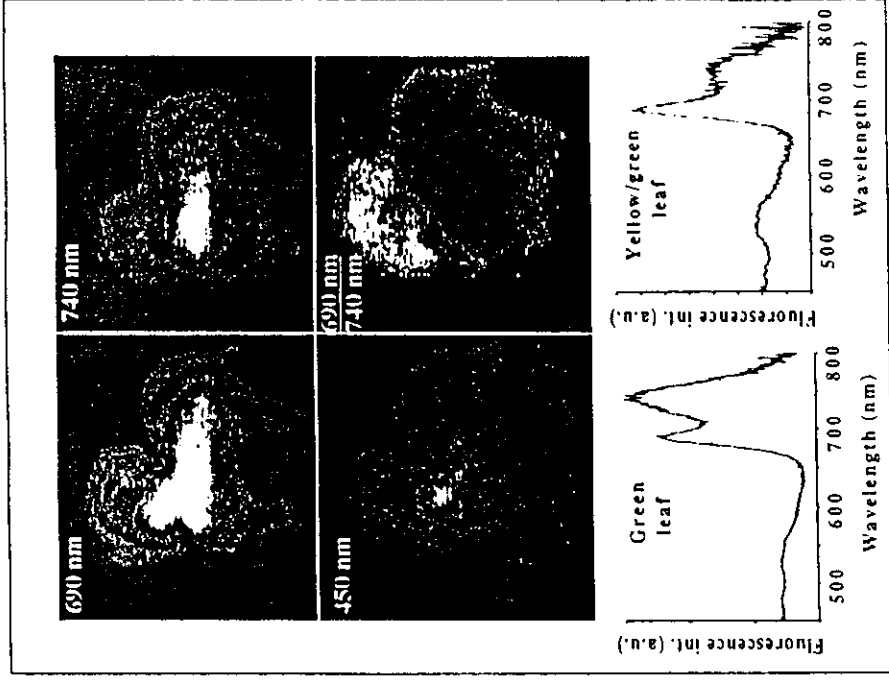Fig. 12. Remote daily-cycle fluorescence data for maize (from [20]).

Fig. 13. Multi-colour imaging and spectral recordings for two maple leaves. A ratio image, obtained by dividing the two chlorophyll peak intensities by each other for all pixels is also included (from [19, 10]).

of a given cross section. If the beam covers many leaves an average spectrum is obtained. Clearly, it would be of considerable interest to obtain spectra for many different points in a scene at the same time. However, a multi-spectral image is hard to record and to display. By using a filter, a fluorescence image of an extended illuminated target can be recorded in a particular band. Since vegetation spectra show rather little structure, fluorescence images in a limited number of bands would fully characterise the target. We have been using a multi-spectral imaging camera, that we have employed extensively for medical fluorescence imaging [23]. Special optics divides up the fluorescence light into four images that are filtered individually. The spectral images are placed in the four quadrants of an imaging matrix detector, that is preceded by a common image intensifier tube, which is gateable. Mathematical processing can then be performed on the individual, simultaneously recorded images to calculate a new image, enhancing certain aspects of the information. This multi-spectral imaging device can be seen included in Fig. 6, adapted to the lidar receiving telescope. A detailed description of this imaging set-up and several imaging examples can be found in [19].

4.2. Examples of remote multi-spectral imaging of vegetation

As a first example of remote multi-colour imaging we show in Fig. 13 a recording of two maple leaves, out of which one was fully green and the other one slightly yellowish [19, 10]. The distance to the target was 50 m and the excitation wavelength was 397 nm. Three images, recorded at 690 nm, 740 nm and 450 are shown together with a processed image, where the ratio I (690 nm)/I (740 nm) has been formed pixel by pixel. The image has been colour coded and the different status of the two leaves can be clearly seen. Using the spectral mode of our measurement system, fluorescence spectra from the two leaves are shown, exhibiting the origin of the leaf demarcation in the ratio image.

As a further example we show, in Fig. 14, imaging of two leaves of *Brasica campestris*. One leaf (to the left) had been subject to enhanced UV radiation (ozone hole simulation), while the other leaf came from a plant grown under normal light conditions. The difference in fluorescence spectra can clearly be seen in the wavelength dispersed monitoring mode. A ratio between an image recorded in the blue spectral region (BG 38 coloured-glass filtering) and a red image clearly displays the spectral differences between the two leaves.

The influence of a herbicide is shown for the case of maize recorded at 40 m distance in Fig. 15 [20]. Images, where chlorophyll fluorescence has been divided by the blue fluorescence, are shown for untreated leaves and half an hour of the expected increase in chlorophyll fluorescence can clearly be seen as a stronger intensity in the ratio image after the application of the herbicide. Further examples of multi-spectral imaging of different species of plants were obtained during a field-test in the Bothanical Garden of the University of Karlsruhe [24].

The examples show that multi-spectral imaging of a full two-dimensional target scene is possible. For an airborne imaging system it might be more effective to shape the laser excitation beam into a line using cylinder optics and sequentially capture the multi-spectral information on an intensified array detector. Further sequential image lines are obtained when the flying platform is moving forward. By combining the processed image lines, a full two-dimensional
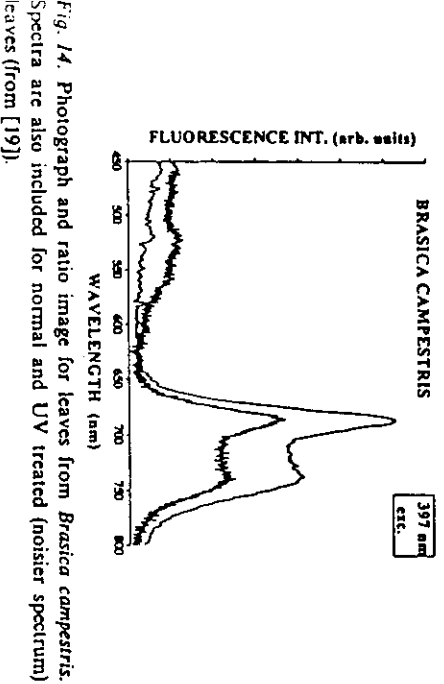
Fig. 14. Photograph and ratio image for leaves from *Brasica campestris*. Spectra are also included for normal and UV treated (noisier spectrum) leaves (from [19]).

FLUORESCENCE INT. (arb. units)

BRASICA CAMPESTRIS

WAVELENGTH (nm)

Fig. 15. Individual spectral images and ratio images for maize before and after preparation with the herbicide DCMU (from [20]).

blue 470nm

685nm blue

685nm 740nm

without DCMU

with DCMU

image may be synthesised. Ground-based text experiments of this kind are now in progress.

5. Discussion and a proposal of a European airborne system

European research activities in the field of remote vegetation fluorescence monitoring performed by German, Italian, French an Swedish groups during the last few years show that it is possible to construct a fluorescence lidar system capable to make single-shot recordings at considerable distance. Collaborative work together with plant physiologists has also shown that fluorescence signals can reflect the concentration of chlorophyll in the leaves and also give some indications of stress of various kind. The temporal domain can also yield valuable information on vegetation status.
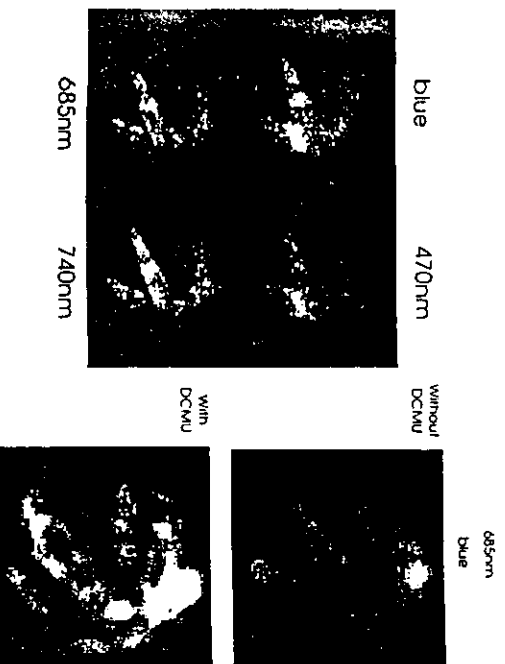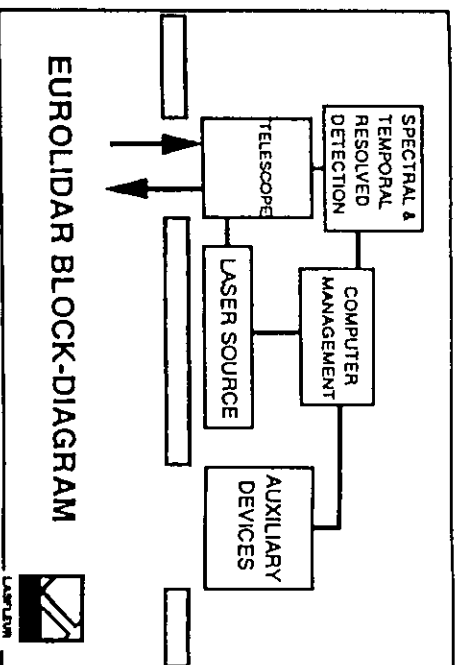

Fig. 16. Schematic diagram of a proposed European modular lidar system for vegetation monitoring (from [26]).

EUROLIDAR BLOCK-DIAGRAM

TELESCOPE

SPECTRAL & TEMPORAL RESOLVED DETECTION

COMPUTER MANAGEMENT

LASER SOURCE

AUXILIARY DEVICES

Here the decay characteristics of the fluorescence in different spectral bands is utilised [25]. However, much further work on the full interpretation of the fluorescence signatures needs to be done to fully exploit the complementarity of fluorescence and reflectance spectral characteristics. In view of the possibility for the success of a more refined monitoring system, the LASFLEUR collaboration has proposed the development of a European airborne system [26]. The system, which is modular, is schematically shown in Fig. 16. A frequency-doubled titanium-doped sapphire laser system operating at 397 nm is proposed as the transmitter. Detection modules include a high-resolution CCD array, a multiple filter/photomultiplier-tube system and a time-resolved system. If realised, such a system could provide a valuable test facility for developing a future fully operational system.

Acknowledgements

References

1. Chen, H. S., "Space Remote Sensing Systems" (Academic, Orlando 1985).
2. Svanberg, S., in: "Air Monitoring by Spectroscopic Techniques" (Edited by M. Sigrist) (Wiley, New York 1994), Chapter 3.
3. Measures, R., "Laser Remote Sensing: Fundamentals and Applications" (Wiley, New York 1984).
4. Hoge, E., in: "Laser Remote Chemical Analysis" (Edited by R. M. Measures) (Wiley-Interscience, New York 1988).
5. Pantani, L. and Reuter, R. (Editors) "Lidar Remote Sensing of Land and Sea" (EARSeL Advances in Remote Sensing, Vol. 1) 1992.
6. Svanberg, S., in: "Optoelectronics for Environmental Science" (Edited by S. Martellucci and A. N. Chester) (Plenum, New York 1990), p. 15.
7. Celander, L., Fredriksson, K., Galle, B. and Svanberg, S., "Investigation of Laser-induced Fluorescence with Applications to Remote Sensing of Environmental Parameters", Göteborg Institute of Physics Reports GIPR-149 (Göteborg, 1978).
8. Rock, B. N., Vogelmann, J. E., Williams, D. L., Vogelmann, A. F. and Hoshizaki, T., BioScience 36, 439 (1986).
9. Lichtenthaler, H. K. and Rinderle, U., CRC Crit. Rev. Anal. Chem. 19, S29 (1988).

10. Johansson, J., "Fluorescence Spectroscopy for Medical and Environmental Diagnostics", PhD Dissertation, Lund Reports on Atomic Physics LRAP-148 (Lund Institute of Technology, Lund 1993).

11. Edner, H. *et al.*, EARSeL Adv. Rem. Sensing 1, 42 (1992).

12. Alberotanza, L. *et al.*, EARSeL Adv. Rem. Sensing (in press).

13. Svanberg, S., in: "Lasers in Medicine" (Edited by G. Pettit and R. W. Waynant) (Plenum, New York 1995).

14. Edner, H. *et al.*, EARSeL Adv. Rem. Sensing 1, 119 (1992).

15. Andersson-Engels, S. *et al.*, Lasers Med. Sci. 6, 415 (1991).

16. Andersson-Engels, S., Callander, K. and Galle, B., "Investigation of the Possibilities to use Laser-induced Fluorescence to Map Conifer Forest Damage Caused by Ozone", IVL Report L88/146 (IVL, Göteborg 1988).

17. Edner, H., Johansson, J., Ragnarson, P., Svanberg, S. and Wallinder, E, EARSeL Adv. Rem. Sensing (in press).

18. Edner, H. *et al.*, Appl. Opt. 26, 4330 (1987).

19. Edner, H., Johansson, J., Svanberg, S. and Wallinder, E, Appl. Opt. 33, 2471 (1994).

20. Andersson, M. *et al.*, in: "Proceedings ISPRS Symposium, January 1994, Val d'Isère 'Physical Measurements and Signatures in Remote Sensing'", p. 835.

21. Andersson, P. S., Montán, S. and Svanberg, S., Appl. Phys. B44, 19 (1987).

22. Lang, M., Stober, F. and Lichtenthaler, H. K., Radiat. Environ. Biophysics 30, 333 (1991).

23. Andersson, P. S., Montán, S. and Svanberg, S., IEEE J. Quant. Electr. QE-23, 1798 (1987).

24. Edner, H. *et al.*, EARSeL Adv. Rem. Sensing (in press).

25. Goulas, Y., Moya, I. and Schmuck, G., Photosynth. Res. 25, 299 (1990).

26. Cecchi, G., Günther, K., Moya, I. and Svanberg, S., Proposal for a EUROLIDAR (unpublished).